

UNIVERSITY OF NAPLES “FEDERICO II”



SCUOLA POLITECNICA E DELLE SCIENZE DI BASE

PhD program in

INDUSTRIAL PRODUCT AND PROCESS ENGINEERING

DEPARTMENT OF CHEMICAL, MATERIALS AND PRODUCTION
ENGINEERING

**Engineering novel scaffolds with *in silico* designed
microarchitectures and potentially suitable for spatio-temporal
drugs release**

SUPERVISOR

Prof. Paolo Antonio Netti, PhD

CO-SUPERVISOR

Eng. Aurelio Salerno, PhD

CANDIDATE

Giuseppe Cesarelli

ACADEMIC YEARS 2016-2019

Index

List of the abbreviations	4
Abstract	6
Chapter 1: introduction to tissue engineering and multifunctional scaffolds.....	7
1.1 Scaffolds properties.....	8
1.1.1 Morphology and pore structure features.....	11
1.1.2 Drug loading and controlled release	14
Chapter 2: Scaffolds fabrication techniques	18
2.1 Traditional processes.....	18
2.2 Advanced bottom-up fabrication	20
2.2.1 Continuous processes: Additive Manufacturing	21
2.3 Discontinuous processes: lithography	28
2.4 Aims of the work	36
Chapter 3: composite scaffolds <i>in silico</i> design, fabrication and characterization	39
3.1 Bottom-up approach scheme.....	39
3.2 Design stage	40
3.2.1 Layers	40
3.2.2 3D scaffolds building.....	41
3.2.3 Drug delivery systems.....	42
3.3 Layers fabrication by magnetic embossing.....	44
3.3.1 Molds fabrication by micromilling and soft lithography	44
3.3.2 Molds characterization	48
3.3.3 Magnetic embossing.....	50
3.3.4 Layer characterization methods	54
3.4 Layers characterization	55
3.4.1 Morphology	55
3.4.2. Pore structure	58
3.4.3 Surface chemistry characterization	59

3.4.4. Surface topography	61
3.5 Scaffold building by PCL layers assembly	63
3.5.1 Assembly parts design and fabrication.....	63
3.5.2. Layers assembly	64
3.5.3 Layer characterization methods.....	65
3.6. 3D PCL scaffolds characterization	67
3.6.1 Morphology	67
3.6.2. Pore structure	67
3.6.3. Porosity	70
3.6.4 Mechanical properties.....	70
3.6.5. Biocompatibility (<i>in vitro</i> tests)	72
3.7 Drug delivery systems	74
3.7.1 Vascular endothelial growth factor – loaded poly(lactic-co-glycolic acid) microparticles by double emulsion.....	74
3.7.2. Microparticles characterization.....	75
3.7.3. Drug delivery systems external shells fabrication.....	77
3.7.4. External shells characterization.....	79
3.7.5. Drug delivery systems: microparticles packing and sintering	80
3.7.6. Microparticles packing and sintering characterization	81
3.7.7. Drug delivery systems: sealing	83
3.7.8. Drug delivery systems: characterization	83
3.7.9 Gelatin films swelling experiments.....	85
3.7.10 Fabrication of composite multifunctional scaffolds.....	86
3.7.11 Characterization of composite multifunctional scaffolds	86
Chapter 4: conclusions and future perspectives	89
References.....	91

List of the abbreviations

40,6-diamidino-2-phenylindole	DAPI
Additive manufacturing	AM
Attenuated total reflection Fourier transform infrared spectroscopy	ATR-FTIR
Basic fibroblast growth factor	bFGF
Bone morphogenetic proteins	BMPs
Bovine serum albumin	BSA
Carbon dioxide	CO ₂
Computer aided design	CAD
Computer aided manufacturing	CAM
Drug delivery systems	DDSs
Extracellular matrix	ECM
Food and drugs administration	FDA
Fused deposition modelling	FDM
Gelatin–vinyl acetate	GEVAC
Green fluorescent protein	GFP
Human bone marrow stem cells	hBMSCs
Human mesenchymal stromal/stem cells	hMSCs
Human umbilical cord-derived mesenchymal stem cells	hUC-MSCs
Human umbilical vein endothelial cells	HUVECs
Inferior turbinate human stem cells	ITSCs
Integrated tissue–organ printer	ITOP
Material testing stage	MTS
Melt electrospinning writing	MEW
Melting temperature	T _m
Mesenchymal stem cells	MSCs
Micro-computed tomography	μ-CT
Micromilling	μ-milling
Microparticles	μPs
Microscaffolds	μ – scaffolds
Microscale continuous projection printing	μCPP
Nanoparticles	nPs
Neural progenitor cells	NPCs
Nitrogen	N ₂
Number of replicates	n

Phase Separation Micromolding	PS μ M
Phosphate buffered saline	PBS
Platelet-derived growth factor-BB	PDGF-BB
Poly (ethylene glycol)	PEG
Poly (ethylene glycol) dimethyl ether	PEGDM
Poly (octamethylene maleate (anhydride) citrate)	POMaC
Poly(dimethylsiloxane)	PDMS
Poly(glycerol sebacate)	PGS
Poly(lactic acid)	PLA
Poly(lactic-co-glycolic acid)	PLGA
Polycaprolactone	PCL
Polytetrafluoroethylene	PTFE
Replica molding	REM
Significance level	α
Smooth muscle cells	SMCs
Sodium chloride	NaCl
Soft lithography	SL
Starch-polycaprolactone	SPCL
Tissue engineering	TE
Ultraviolet	UV
Vascular endothelial growth factor	VEGF

Abstract

Porous bioactive scaffolds are key components in several tissue engineering strategies. For their effective implementation, it is necessary bioactive scaffolds are capable to accurately deliver potent biological signals to control and guide the morphogenic and tissueogenic processes.

This thesis describes the development of a novel bottom-up approach to design, engineer and fabricate modular scaffolds with a precise morphological structure and potentially capable of a controlled presentation over time and space of biological factors.

Initially, an *in silico* study supported by the scientific literature was done to design modules (structural layers and drug delivery systems) features. Simultaneously, the same study focused on the selection of the better suited materials and manufacturing techniques to use during the fabrication stage.

Secondly, layers with a 0°/45°/90° filaments orientation and different thickness and/or features (related to the function to fulfil) were fabricated using a magnetic embossing process; contextually, truncated round-shaped drug delivery systems were manufactured using a combination of soft lithography and drug loaded microparticles sintering methods.

Finally, modules integration was described and scaffold assembled using a solution-based assembly process.

The results show that modules architecture strongly resembles the designed virtual models and present a superficial topography in the submicron-scale. Drug loaded microparticles could be successfully sintered and sealed inside microfabricated shells as shown by microscopy observations.

Scaffolds tomographic models present a satisfactory correspondence with virtual models. Compression tests show elastic moduli values of ≈ 30 MPa and an effective bonding between layers which could ensure scaffolds integrity for *in vitro* and *in vivo* tests. *In silico* and real porosities values are equal to $\approx 57\%$. *In vitro* biocompatibility tests on scaffolds demonstrate good endothelial cells adhesion ($\approx 58\%$ at 6h) and proliferation up to 7 days. Confocal microscopy shows cells successfully adhered and stretched on scaffold layers surfaces.

Finally, a tomographic model has proved the effective integration of structural layers and drug delivery systems demonstrating the fabrication of a predesigned scaffold with vascular endothelial growth factor loaded drug delivery systems integrated in the scaffold centre.

In conclusion, this thesis demonstrates the feasibility to fabricate modular scaffolds which could potentially demonstrate enhanced control strategies to support the presentation of biomacromolecular factors at the right time, with the right dose, and for the right time frame.

Chapter 1: introduction to tissue engineering and multifunctional scaffolds

The human body is a multicellular organism whose cells and extracellular matrix organize to build complex tissues and organs. However, several unplanned events, such as e.g. traumas and dysfunction, or diseases (for instance caused by congenital defects) can compromise the correct functioning of the human body; albeit tissue and organs can self-repair small defects, in several worst-case scenarios chronic defects are hardly self-regenerated and require external interventions.

The main strategies adopted in the past years to restore tissues and/or organ functions were tissue grafting and organ transplantation procedures. Although major technical limitations have been overcome during time and several organ transplants are nowadays routine procedures, shortage of organs¹ and possible post-surgery complications² have suggested scientists and experts to investigate alternative strategies.

Tissue engineering (TE) among the others, has gained a greater consideration over years because it has effectively improved patients' quality of life, even though TE methodologies have been implemented and diffused only since the early 90's^{3,4}. TE was defined in 1993 by its inventors as "an interdisciplinary field that applies the principles of engineering and life sciences toward the development of biological substitutes that restore, maintain, or improve tissue function or a whole organ"⁵.

Since its start, TE has relied on three key factors, namely cells, bioactive molecules and scaffolds, which work together to fulfil TE goals. Hereinafter it will be introduced the main properties of such pivotal factors.

The principal function of cells is to synthesize matrices of new tissue for replacing damaged ones; autologous (patient's own) cells would be the best ones for TE experiments, but they are always not enough for clinical treatment, especially when a patient is aged or has severely been diseased. For this reason, there have been experimented new solutions as, for instance, stem cells-based therapies⁶.

Bioactive molecules, such as growth factors, are molecular cues which direct a variety of cellular processes important for tissues regeneration⁷; as an example, bone morphogenetic proteins (BMPs) and basic fibroblast growth factor (bFGF) alone can induce bone and vascular tissue regeneration, respectively, ideally without the assistance of scaffolds or seeded cells⁶.

Unluckily, in a typical scenario isolated cells are hardly capable of organizing spontaneously to form complex large-sized tissues and organs in the absence of three-dimensional supporting structures (the scaffolds) which must mimic the

extracellular matrix (ECM) functions. These must help cells to recreate the natural complex structures of a specific tissue promoting cells adhesion, growth (under appropriate culture condition) and differentiation.^{6,8}

Typical strategies in TE are *in vitro*, *in vivo*, or *in situ* ones.

In particular^{9,10}, as also schematically illustrated in figure 1.1:

- *In vitro* TE: specific cell types are isolated and expanded to be later seeded in a bio-instructive scaffold and cultured in a static (incubator) or dynamic (bioreactor) environment to obtain an engineered tissue. Finally, this is transplanted into the patient;
- *In vivo* TE: scaffolds are implanted usually with cells and an animal is used as an incubator to grow the tissue or the organ before being re-implanted in the same or another patient;
- *In situ* TE⁹⁻¹¹: scaffolds are implanted or injected with or without cells into the patient's (or animal's) body. The tissue is expected to self-repair due to cell migration and cells growing directly in the body's environment, which acts a bioreactor.

Accordingly, scaffolds are crucial in all the presented strategies. The next paragraphs will focus on their key properties for TE applications.

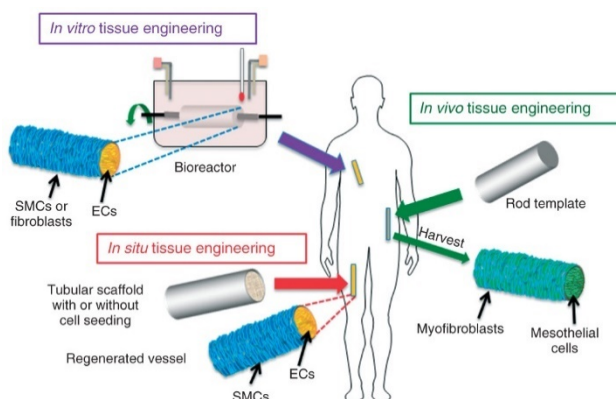


Figure 1.1: Schematic illustration of *in vitro*, *in vivo*, and *in situ* tissue engineering. Reused with permission from John Wiley & Sons¹¹.

1.1 Scaffolds properties

As briefly introduced, scaffolds should meet several requirements to fulfil the diverse functions it has to perform. Among these requirements, it is possible to provide a general overview of the multiple different ones to consider even before the scaffold design phase starts.

- Morphology and pore structure requirements: features such as controlled open pore structure (e.g. dimension and geometry), pore interconnection, surface area to volume ratio must be matched to design a structure which could mimic as closely as possible the native ECM and its functions^{12,13}.

Morphology and pore structure are of great importance for instance for tasks such as the efficient nutrient and metabolite transport, vascularization and new tissue formation and remodelling, as the next paragraph will discuss in greater detail;

- Mechanical requirements: like morphology and pore structures, mechanical properties must be tuned to mimic the natural ECM. These must guarantee^{14,15}:
 - a. the spaces required for cell ingrowth and matrix production in *in vitro* conditions (cells should 'feel' the right mechanical stimuli as in the native environment to produce the right type of ECM);
 - b. resistance during implant;
 - c. resistance to typical applied loads *in vivo*: mechanical properties should closely emulate those of living tissue such that, during the regeneration process, the sum of the contributions of the (degrading) scaffold and (growing) new tissue are adequate to withstand the imposed loads.
- Biological requirements:
 - a. Biocompatibility, or rather the material capacity to trigger favourable reactions of a living organism in specific TE applications. A biocompatible scaffold must not be toxic, trigger inflammatory reactions or reject while interacting with the host immune system and moreover should promote wound healing, reconstruction and tissue integration¹⁶;
 - b. Compatibility with biological environment: this property considers the interaction of a scaffold with the surrounding environment; we could briefly extend the concept defining a:
 - i. Morphological compatibility: scaffolds must be designed to respect organism interfacial dimensions, shape and mass¹⁷; tissues complexity does not always facilitate the design and fabrication of simple scaffold structures. Indeed, Zhu and co-workers showed for instance the design and fabrication of complex ECM-like scaffolds to be implanted in anisotropic structures for vascular and nerve regeneration purposes¹⁸;
 - ii. Functional compatibility, or rather the evaluation of scaffold actual functions compared the expected ones. Several studies to date have demonstrated a mismatch in the effective scaffolds properties compared to the ideal ones; therefore new approaches for scaffolds functional compatibility evaluation are growing up. Ghouse and co-workers, for instance, have studied the medial femoral condyle mechanical properties in ovines with the aim of designing a scaffold whose properties should effectively strictly match those of the bone to be replaced¹⁹;

- iii. **Biological compatibility:** this property considers all the biological and chemical aspects which can be detrimental for tissues and the scaffold itself; the work of Cortese and Elwany discuss the behaviour of bioresorbable vascular scaffolds for cardiac TE after implantation in human patients²⁰. It was observed that, although these scaffolds are biocompatible devices which have also partially replaced conventional metallic stent in the clinical practice, there is still a non-negligible risk of failure (e.g. scaffolds thrombosis) for longer implantation times which highlight the need of extended studies of scaffolds effective biological compatibility for *in vivo* applications²¹;
- c. **Biodegradability:** scaffold degradation time must be strictly coordinated with that of the new tissue growth. Several are the parameter which are considered to evaluate scaffolds degradation kinetics, such as material composition (and the presence of cross-linkers), the interaction of the scaffold with environment (e.g. pH variations), scaffold structure properties, superficial properties, external factors (ultrasound, heat, and other environmental stresses) and also scaffolds physical loading conditions. Despite today the control of scaffold degradation is only indirectly evaluated (before and/or during implantation), active methods for controlling scaffold degradation rate are emerging to reach the desired degradation goal²²;
- **Bioactivation properties:** scaffolds should be designed to actively interact with the cellular components of the engineered tissues to facilitate and regulate their activities. Scaffold bioactivation strategies may encompass the use of biological cues such as cell-adhesive ligands to enhance cell attachment or physical cues such as topography to influence cell morphology and alignment. The scaffold may also serve as a delivery vehicle or reservoir for exogenous growth-stimulating signals such as growth factors to speed up regeneration¹². A deeper analysis of scaffold bioactivation properties will be presented in paragraph 3;
- **Processability:** scaffold materials should be easily processed implementing a reproducible process to achieve the desired morphological and dimensional features. These are of great importance when the final shape of the regenerated tissue has a critical influence on its activity^{23,24};
- **Sterilizability:** scaffold materials must not degrade as consequence of sterilization processes to be performed for clinical applications^{13,24}.

Therefore, this paragraph has shown how a plethora of properties must be considered for the effective design and fabrication of a scaffold. Although all of

the properties would deserve a deeper consideration, the following sections will concentrate on morphological and bioactivation properties of scaffolds, because these will be the core of the *in silico* study presented in chapter 3.

1.1.1 Morphology and pore structure features

As already introduced, scaffolds must emulate the physiological function of the original extracellular matrix (ECM) to preserve cells capability to reproduce their original differentiated phenotypes. The first step toward this direction is to design a scaffold whose morphological and structural features could resemble as closely as possible that of the tissue to replace.

The first parameter to consider for scaffold architectural design is pore size; indeed, this feature in *in vitro* application is related to diameter of cells in suspension and their later morphogenesis proliferation and differentiation, while in *in vivo* applications pore dimension influences and cell migration and surrounding tissue infiltration²⁵. A typical pore dimension classification in scaffolds generally considers nanopores (< 300 nm), micropores (0.3 – 100 µm in size) and macropores (> 100 µm in size). These different pore size surfaces are able to direct cell behaviour: a typical, but not exhaustive, classification reports²⁶:

- Nanopores: promote cellular attachment by inducing cells to develop focal adhesions;
- Micropores: improve the scaffolds permeability and facilitate cell migration;
- Macropores: provide space for vascularization, nutrients supply, waste removal, and gas diffusion.

Several publications have appeared in recent years documenting nanopores in several tissue components and their importance in directing cell behaviour. For instance, as reported by Kaltschmidt and co-workers, collagen Type I fibers spatial arrangement in bone presents 30 nm pores; they demonstrated these structures can induce naturally osteogenic differentiation of inferior turbinate human stem cells (ITSCs). Moreover, the results thus obtained are compatible with a osteogenic differentiation in a biomimetic system, as was demonstrated seeding the same cells on ceramic silicon dioxide scaffolds with similar features (34 nm pores)²⁷.

However, other studies, such as that of Brennan and co-workers, have concluded that also microstructured fibrous ECM-like scaffolds could induce stem cells osteogenesis. Specifically, different polymeric scaffolds with a 50 µm apparent pore size were fabricated and human bone marrow stem cells were cultured up to 21 days. Enhanced collagen and calcium deposition (both normalised to DNA content) for the 100 µm fibre spacing scaffolds demonstrate an enhanced osteogenic capacity of these fibrous structures which represent an

excellent *in vitro* model for the study of human bone marrow stem cells behaviour²⁸.

Further study of the issue, such as a recent paper by Wang and co-workers, seems in contrast with the presented findings. Herein there was indeed reported the fabrication and characterization of four different metallic scaffolds configurations with pore sizes higher than 400 μm . Although after 4 weeks two of the four scaffolds types showed a better bone tissue ingrowth *in vivo*, osteogenic differentiation evaluation after 21 days proved there was no significant difference in the alkaline phosphatase (ALP) activity among the four porous groups which could be considered all potentially suitable for bone regeneration²⁹.

Table 1.1 summarizes several examples of scaffolds with nano-/micro-/macroporous structures which have demonstrated suitable (or potentially suitable) for several TE applications (for instance bone TE, as yet described, cardiac^{30,31} or liver^{32,33}).

Application	Cell type	Scaffold materials	Pore size (μm)	Porosity (%)	Notes
Bone	ITSCs ²⁷	Silicon dioxide	0.034	N/A	0.018 μm pores do not lead to cells differentiation
	hBMSCs ²⁸	PCL	50	N/A	Fibre distances tested: 100/200/300 μm
	hBMSCs ²⁹	Ti ₆ Al ₄ V	427-458	61-66	Several scaffolds differences in mechanical properties and <i>in vivo</i> behaviour
Heart	Rat H9c2 myoblasts ³⁰	Gelatin	50	76	H9c2 differentiate spontaneously on gelatin scaffolds
	Rat MSCs ³¹	Gelatin coated iron oxide	200	N/A	Gelatin does not change pore size and promote cells adhesion
Liver	hUC-MSCs ³²	GEVAC	70-100	76	Different scaffolds with 75–300 and 100–200 μm tested
	Rat MSCs ³³	C-PLGA	150-350	94	Improved cells viability and hepatocyte-specific functions compared to 2D control

Table 1.1: Pore Sizes and Porosity for different TE applications. Partially reused with permission from Elsevier B.V.²⁵ and Mary Ann Liebert, Inc³⁴.

It must be considered anyway that the presented findings have also indicated the potential use for several applications of scaffolds with multiple pore dimensions, such as the polymeric ones manufactured by Yeong and Dattola for cardiac TE applications^{35,36} and by Prasopthum for osteochondral TE³⁷.

Anyway, other parameters such as shape, surface-to-volume ratio, pore wall morphology and pore interconnectivity have been demonstrated to directly modulate cell behaviour or specific tissue functions.

Vascularization is a field where the choice of appropriate pore interconnection is crucial; for example, Choi and co-workers have indicated that to promote the development of invading vasculatures scaffolds should have 200 μm interconnected pores³⁸; these results agree with Bai and co-workers study which has fabricated scaffolds with pore sizes ranging from 300 to 700 μm demonstrating that above 400 μm there was no difference in vascularization³⁹. However, tissue ingrowth is related also to pore interconnectivity as demonstrated by Somo and co-workers⁴⁰ which have fabricated several hydrogels to be used for vascularization evaluations based on variable pores interconnectivity. Hydrogels for histological analyses were fabricated with a mean pore size of 129 μm and normalized pores connectivity values, which is an indication of the interconnectivity values on the mean pore size, of 0.24 and 0.42. The results show that hydrogels with larger interconnectivity allowed for extensive vascularization and formation of blood vessel networks within the pores *in vivo* at both 3 and 6 weeks⁴⁰.

Pore shape and pore wall morphologies have proved as another pivotal factors in TE scaffolds, such as for instance in cartilage TE. Hollister and co-workers have indeed developed several researches works in the field analysing how scaffolds design could direct chondrocytes and/or stem cells behaviour. The results show that for both cell types the use of spherical shaped pores (compared to cubical pores) promote a more robust ECM production by cells; these findings were attributed to events such as increased local cell densities (chondrocytes) or induction of cellular condensations (stems cells)^{41,42}. Anyway, the same authors demonstrate chondrocytes or stem cells need different environments for an optimal ECM production; indeed, chondrocytes proved to better produce a stable cartilaginous matrix in lower permeable environments, such as spherical shaped scaffolds with pores of small interconnection sizes (220 μm), while bone marrow stromal cells demonstrated an increase in cellular differentiation and chondrogenic markers in scaffolds with pores of bigger interconnection sizes (380 μm)⁴². Finally, in a further study, chondrocytes seeded scaffolds were analysed also in terms of degradation and mechanical properties: two scaffolds with the same pore sizes and surface area, but different porosity values, were fabricated and mechanically compressed

demonstrating a huge variation in the non-linear elastic properties in a range between 1.5 to 4 times. Moreover, these scaffolds demonstrated also a better chondrogenic integration with the new growing tissue cartilage after for weeks *in vitro* degradation tests. These results were suggested by a successful correspondence between the tangent moduli of the degraded scaffold and native tissue and by chondrogenic markers evaluations⁴³.

The complexity in tuning scaffolds whose features resemble as closely as possible the natural ECM have demonstrated to be challenging in several scenarios. Therefore, new solutions/technologies are strongly desired to support the design and prediction of scaffolds architecture properties and mechanical behaviour, respectively. As an example, topology optimization paradigms⁴⁴ has demonstrated a great potential in defining porosity, pore size, mechanical properties, geometrical constraints and even their mutual relationships^{45,46}.

1.1.2 Drug loading and controlled release

The control of scaffolds architectural, structural and degradation properties has proved successful to date for regenerating several critical tissue defects. Anyway, the improved control over scaffolds microstructural features has not always been followed by positive *in vitro* and *in vivo* tissue regeneration results. Indeed, tissue growth within the highly interconnected porous network of scaffolds resulted far from being optimal and often proved dysfunctional. Scientific community found as a common explanation that cells in a pore within a 3D matrix would not receive all the microenvironmental cues essential to direct and guide the tissueogenesis process. Therefore, scaffolds which have showed a passive role in tissue regeneration, or rather a poor interaction with the surrounding environment, have been replaced by new multifunctional bioactivated scaffolds. These presents biomolecular cues which support scaffolds control of the cellular microenvironment inducing both cell–cell and cell-material interactions, which are crucial to promote an advantageous biological response of the environment^{47,48}.

A possible strategy to bioactivate scaffolds is represented by loading drugs for a specific purpose; anti-inflammatories (fenbufen, ibuprofen and naproxen sodium), antibacterials and antimicrobials (gentamicin and tetracycline hydrochloride), antibiotics (ciprofloxacin)⁴⁹ and other small molecules have been loaded in scaffolds which have been tested demonstrating as valid platforms in TE. Nonetheless, several of such findings proved so promising to motivate scaffolds validation in preclinical studies⁵⁰.

Albeit the loading of such drugs in scaffolds, it should be pointed out other molecules, specifically growth factors (GFs), have extensively studied because

these are a component of the ECM. This is the natural network in which cells proliferate, differentiate and migrate; these synthesize, assemble and degrade ECM components responding to specific signals while ECM controls and guides specific cell functions. These are mainly governed by GFs, signalling molecules specific for intercellular and cell-ECM signalling involved in ECM dynamic properties (e.g. remodelling) through specific surface receptors. GFs activate specific pathways controlling cell migration, differentiation and proliferation. The presence of soluble GFs guides cellular behaviours and consequently governs neo-tissue formation and organization^{51,52}.

Thus, bioactivated scaffolds with integrated mechanisms of matricellular cue exposition and GFs sequestration and delivery, with the aim of mimicking the natural ECM, were designed and manufactured^{7,47,51-54}.

The first one method implemented in TE was the simple interspersation of GFs into the scaffold matrix. Despite this approach has been widely used in the literature, several issues have limited its application, among which we can consider^{47,51}:

- Enzymatic degradation due to a fast *in vivo* exposition;
- Poor spatial and/or temporal control (tissue structures require the adjustment of the local concentration of signalling molecules and eventually its changing over time);
- Side-effects caused by GF over expression in time and space.

Consequently, it has immediately appeared clear the need for alternative strategies with the aim to create scaffolds also with advanced delivery features. There have been investigated opportunities such as adsorption or layer-by-layer assembly of GFs on scaffolds surface, GFs covalent immobilization on scaffolds (carbodiimide or natural mussel inspired bioconjunctions for instance) and also ECM-inspired binding approaches^{52,54,55}. However, these require an *ab initio* design of bioactivated constructs which consider both scaffold and delivery requirements. Specifically, properties such as drug loading efficiency, appropriate release kinetics and physical, chemical, and biological activity must be achieved and tailored in symbiosis with structural and architectural scaffold properties^{54,56}. Unluckily, an optimal symbiosis between scaffold and delivery requirements is very difficult to attain.

Thus, drug delivery systems (DDSs) were designed to provide GFs preservation from *in vivo* degradation and inactivation, to prolong the duration of scaffold bioactivation and to design and modulate GFs release at preprogrammed rates by regulating platform composition, shape and architecture^{52,54}.

Several GFs loaded DDSs have been investigated to date; among them, micro – (μ Ps) and nanoparticles (nPs) are the one that have been extensively studied^{51,52,54,55}. The importance of these DDSs in the controlled drug delivery field is motivated in the possibility to engineer structures with different physico-chemical characteristics (e.g. chemical nature, composition, molecular weight, hydrophilicity, degradability) and the possibility to use biodegradable polymers which, differently from non-degradable systems, do not require further manipulation after introduction within the body^{51,52,54}. Several biodegradable natural and synthetic polymers have been studied to fabricate GFs – loaded particles; among these, polyester copolymers have been demonstrated the most versatile ones, because their properties can be easily tailored by varying composition, molecular weight and chemical structure (i.e. capped and uncapped end-groups). Poly(lactide-co-glycolide) (PLGA) is one of the most suited polymers for these applications thanks to tunable *in vivo* lifetimes (from 3 weeks a year) and its well-known security for human use^{51,52,54}.

Scaffolds with interspersed DDSs have represented an interesting strategy of bioactivation that is still investigated in TE and have demonstrated interesting findings. For example, Richardson and co-workers have designed and fabricated and composite scaffold PLGA scaffold bioactivated by vascular endothelial growth factor (VEGF) and platelet-derived growth factor-BB (PDGF-BB). VEGF was directly interspersed into the scaffold while PDGF-BB were firstly loaded inside μ Ps which were subsequently interspersed. VEGF was positioned predominantly adjacent to scaffold pores and was released rapidly (40–60% in 5 days) while PDGF-BB (loaded in μ Ps) demonstrated a slower release (40-60% in 20 – 25 days). Consequently, this example demonstrated the possibility to design and fabricate scaffolds capable of dual GF delivery which could be used in applications like vascularization in bone TE where the temporal control of VEGF and PDGF-BB can direct the formation of a more mature vasculature as compared to the delivery of VEGF or PDGF alone⁵⁷.

Similar μ Ps were used by Akar and co-workers for designing a composite gradient scaffold. Specifically, a porous hydrogel was fabricated and subsequently bioactivated depositing on a unique surface a composite polymeric layer with interspersed PDGF-BB loaded μ Ps. The aim was to confer to this scaffold spatial gradient properties, by varying the degradation rate of gradient layer components or dose of PDGF-BB delivered, and to investigate the influence of PDGF-BB gradients on vascularized tissue formation within the scaffold. The data obtained indicated that a PDGF-BB gradient was effectively created and persisted *in vivo* for over 3 weeks; the best results were obtained with a dose of 200 ng of loaded PDGF-BB. Moreover, the gradient scaffold allowed a better tissue invasion depth compared to scaffolds where PDGF-BB

loaded μ Ps or free PDGF-BB were respectively homogeneously interspersed⁵⁸. Therefore, a well-tailored spatial presentation of GFs has a significant potential for applications in TE where highly vascularized scaffolds capable of persistent GFs gradients are requested.

Despite the significant advancements in tissue guidance and regeneration showed by several bioactivated scaffolds, preclinical and clinical studies indicate that further research is still required. Indeed, such scaffolds have been designed to deliver potent biological signals to control and guide the morphogenic and tissueogenic processes. Anyway, to induce the desired cell response, a given signal must be presented at the right time, with the right dose, and for the right time frame; currently, these systems only sometimes demonstrate optimal control strategies in signal presentation^{47,52,54}. In conclusion, novel programmable materials with encoded strategies to control the space and time presentation of bioactive cues and to control and guide specific events at the cellular scale are needed to better mimic the natural ECM dynamic behaviour and overcome the actual tissue regeneration limitations.

Chapter 2: Scaffolds fabrication techniques

The possibility to design tailored scaffolds for a specific TE application is also related to the choice of suitable manufacturing processes.

Scaffolds fabrication technologies are mainly expected to provide the maximum control over macro- and microstructural features without negatively affecting the other properties (for instance, bioactivation requirements). Moreover, fabrication methods must guarantee as much as possible scaffolds structures to be accurate and reproducible when processing parameters are fixed.

An additional criterion strictly related to manufacturing methods is materials choice: indeed, scaffolds properties are dependent on the natural or synthetic material chosen and its intrinsic properties. Anyway, each material or combination of materials has a different degree of processability and processing requirements which in turn influence final scaffolds features²³.

Thus, the appropriate manufacturing process choice is not trivial and it must be carefully pondered to achieve scaffolds whose properties could closely resemble the designed ones.

In the first part of this chapter the most used scaffold fabrication techniques, ranging from the oldest to the novel ones, will be introduced. Finally, in the second part the reasons which have guided the choice for specific fabrication technologies for this *in silico* work will be explained.

2.1 Traditional processes

Traditional methods are the established and oldest ones in TE. The most used to date have been porogen and thermodynamic based processes⁵⁹.

Porogen based methods involves the preparation of solutions containing appropriate porogen materials which are later dissolved after consolidation of the final scaffold structure. Sodium chloride⁶⁰ has been the most used granular porogen thanks to its high stability during fabrication, a high solubility in water and a good granulometric control; despite these advantages, such salts do not allow an accurate control of pores geometry. Thus, it has been diffused manufacturing techniques which are based on spherical porogens, such as paraffin or gelatin⁶¹ (biocompatible) microparticles (μ Ps), which have allowed to overcome the previous problem and at the same time improve pore interconnection.

Continuous porogens have been productive alternative solutions. A typical example involves the fabrication of immiscible co-continuous blends^{62,63} scaffolds whose pores are generated using an appropriate solvent dissolving the material used as porogen. Another possible solution is fiber templating^{64,65}; typically, aligned fibers are fabricated and subsequently embedded in a

structure whose pores are generated dissolving the embedded fibers using a non-solvent for the final scaffold structure. The use of continuous porogens showed as a valid methodology for manufacturing more biomimetic scaffolds⁶³⁻⁶⁵ (i.e. aligned structures that better match the architecture of several anisotropic tissues) and with improved mechanical properties in comparison to granulated porogens based scaffolds^{25,66}.

Gas foaming and phase separation, instead, promote pores generation through thermodynamic instabilities. The former involves the high pressure solubilization of a non-toxic blowing agent (typically carbon dioxide, nitrogen or their mixtures) within a biomaterial solution. The porous structure is generated by firstly nucleation and growth of gas bubbles (through a temperature increment or pressure reduction) and the subsequent setting of the biomaterial structure decreasing system temperature^{25,66}. Gas foaming allows to fabricate more biomimetic and bioactive scaffolds compared to porogen - based techniques⁶⁷, anyway with the important drawback of the generation of a not negligible amount of closed pores, which are undesired in TE scaffolds⁶⁶.

Phase separation architectures, instead, are fabricated from homogeneous solutions preparation using low freezing point solvents. Thermodynamic instabilities (typically exposure to non-solvents or temperature decreasing) are induced to create heterogeneous morphologies characterized by polymer rich and polymer-lean phases. Solvent removal from polymer lean phases allows to create the interconnected porous scaffold^{25,66}. Phase separation allows an improved control on porosity distribution, geometry and interconnection, although its widespread use has been limited by the presence of retained toxic chemicals, an inaccurate porosity control and limited materials choice^{68,69}.

Albeit the interesting findings in TE using the discussed methods, these have been partially overlooked by the success gained by bottom-up fabrication technologies⁷⁰. These are based on the implementation of prefabricated structures (i.e. fiber templates) which are mainly assembled in a layer-by-layer fashion, such as scaffold fabricated by sintered μ Ps layers. The motivation of bottom-up approaches implementation is related to the possibility of manufacture scaffolds with crescent architectural complexity and with better ECM-like properties compared to the yet introduced "top-down" methods.

Fiber bonding process involves a prefabricated fiber template, which is casted in specific polymeric solutions with subsequently solvent extraction⁷¹; although the fabricated scaffolds have been demonstrated valid in regenerating tissues which request structures with an high pore interconnection and a high surface to volume ratio, there are no fine porosity control and adequate mechanical properties for *in vivo* implantation⁶⁶.

μ Ps sintering, instead, is a technology based on the sintering of packed μ Ps. Sintering is promoted by mass transfer processes induced for instance by temperature or appropriate solvents/solvent vapours. The high diffusion of these scaffolds has been motivated by the easiness of established emulsion fabrication processes⁷² (nowadays in addition with novel microfluidics, lithography and micromolding ones also) for μ Ps preparation and final scaffolds properties such as high-resolution control over spatial organization and the possibility to bioactivate scaffolds encapsulating biological factors (for instance growth factors)⁷³. Although microscaffolds (μ – scaffolds) - scaffolds fabricated by μ Ps sintering processes - have proved as valid systems in several TE applications^{73,74}, some key issues have limited their successful clinical translation. Firstly, μ – scaffolds require multiple steps of fabrication, from uPs' preparation up to assembly and sintering. For sure, the possibility to reduce scaffolds' manufacturing time by automated processes will be a great enhancement towards clinical implementation. Anyway, the main limitation is related to structural considerations; in fact, biological tissues are characterized by hierarchical-ordered architectures at both nano- and micrometric size scales, that can be replicated only in part by uPs' random and ordered assembly⁷⁵.

Finally, electrospinning has been a widely used manufacturing technique in TE because it was one of the few available for nanostructured scaffolds fabrication. Electrospinning is based on the deposition (guided by an electrostatic force) of nanometric polymer fibers from a syringe nozzle (spinneret) on a collector; such scaffolds are of great interest in the field because nanometric electrospun structures mimic collagen nanofibers present in the ECM⁷⁶. Several complex electrospun scaffolds have been fabricated for different TE fields (bone and vascular for instance) but, although the great success, few are the papers in literature that show electrospun scaffolds as *in vivo* models of tissue damage⁷⁷. The main reason is the poor infiltration of cells into these constructs due to too small intra-fiber pore sizes; in this scenario, cells behaviour is like that observed in a 2D environment⁷⁸. As seen in the last chapter, cells need instead to infiltrate and proliferate in a tailor-made 3D structure, which conventional electrospinning techniques are hardly ever capable to emulate.

2.2 Advanced bottom-up fabrication

The main conclusions which arise from the analysis of traditional scaffolds manufacturing techniques are the intrinsic limitations in fabricating specimens whose overall properties can be designed and implemented through user control. Specifically, features such as pore size, pore geometry and spatial pores

distribution can be hardly controlled in these conventional processes, especially “top-down” ones, with high precision⁷⁹.

As already introduced, bottom-up TE paradigm has emerged at the beginning of the 21st century as a possible solution. Anyway, several disadvantages of scaffolds bottom-up approaches have directed researchers’ attention to engineer and assembly micro- and nanostructured biologic modules using scaffoldless approaches (cells and cell-produced materials)^{70,80} to create complex tissues. This strategy has even raised doubts about the importance and necessity of a scaffold⁷⁰ in modern TE applications. Despite this worthy question, researchers are investing resources on both strategies, as for example clearly highlighted for bone TE by Kesireddy and Kasper⁷⁴. The continuous developing of such interest seems justified on the one hand by scaffolds importance in many TE scenarios while, on the other hand, by the current limitations of several scaffoldless approaches in achieving the hierarchy necessary for recapitulating tissue structure and function⁸¹.

In this dissertation the focus will be only on scaffold-based bottom-up techniques, whose modules are patterned continuous layers. These modular methods are usually split in continuous processes and discontinuous processes.

2.2.1 Continuous processes: Additive Manufacturing

The increasing power of electronic computation and the fast technical progress are the pivotal factors which have supported the TE scientific community to design and fabricate biological substitutes whose morphological and structural properties could be highly user – controlled. The most famous bottom – up technologies which allow to fabricate such scaffolds are generally based on the combination of computer aided design (CAD) and computer aided manufacturing (CAM) paradigms; thus, the 3D model of the desired scaffold is designed using a suited CAD software (or, in case of personalized medicine, virtually reconstructed from patients through reverse engineering methods and eventually optimized using CAD software) and fabricated adopting technologies such as those based on automatic layer-by-layer materials (or rather, biomaterials and/or biological matter) deposition or consolidation (namely “additive manufacturing”, better known as “3D printing”).

Several are the improvements these technologies have introduced: considering biomaterials only, additive manufacturing (AM) methods, respect to traditional techniques, allows e.g. scaffolds fabrication with different porosity configurations (from the simplest square to non-uniform ones) and eventually with pores of different dimensions according to scaffold topography (e.g. geometry of internal pores differs from lateral ones)⁸²; nevertheless, the possibility to consider multiple orientation patterns (for instance, non-

conventional ones such as hexagonal and zigzag) for all the layers allows a high control for pore interconnection which directly influences scaffolds mechanical and biological properties⁸².

The presented advantages can be effectively deduced analysing the promising results achieved (for various TE fields) fabricating several synthetic scaffolds using AM; for instance, Van Bael and co-workers have assessed how pores shape variations (specifically, aligned layers presenting triangular versus rhomboidal pores) induce a better differentiation of human periosteum-derived cells towards osteoblasts; among the analysed scaffolds, those presenting 500 μm triangular shaped pores have shown the best cellular differentiation results⁸³. Similar effects were later demonstrated by Di Luca and co-workers that observed an important increase in osteogenic markers (mainly the alkaline phosphatase activity) after culturing osteogenic stem cells for 28 days in a 1:1 ratio chondrogenic and osteogenic medium. The tested scaffolds presented layers designed with rhomboidal pores of more acute angles (0-15° and 0-30°) respect to the classical crisscrossed configuration with square pores⁸⁴. Analogous results were previously shown also by Yilgor and co-workers which studied stem cells differentiation on scaffolds presenting triangular shaped pores (0°/45° filaments deposition)⁸⁵.

Ahn and co-workers have recently fabricated a scaffold with a similar pore structure aimed to study cartilage regeneration *in vitro*. The designed scaffold was characterized by internal pore structures having alternating lattices (isosceles triangles pores) and columns (300 μm height) to allow human chondrocytes to penetrate the scaffold once seeded and to maximize their retention. Such scaffolds effectively demonstrated, after bioactivation with RGD peptides - using a covalent bonding methodology - to promote adhesion and proliferation up to 168 h of human chondrocytes⁸⁶.

Finally, scaffolds presenting a lateral porosity were also presented by Holmes and co-workers for analysing a potential *in vitro* bone tissue regrowth and simultaneous vascularization. Specifically, several layers (375 μm height) with hexagonal pores patterns were deposited and interrupted alternatively by other layers with a simpler pattern of aligned filaments (1 or 0.5 mm diameter). The basic idea of this design was to generate a more biomimetic network for blood vessels development in a typical bone-like scaffold fabricated by AM; a hexagonal porosity was designed moreover to ideally enhance a fast and efficient perfusion of arterial blood, thanks also to the presence of interconnected horizontal and vertical channels which could help capillaries formation. Hydrodynamic preliminary measurements demonstrated such designed structures may provide efficient and adequate blood and fluid transport in and out of the scaffold, similarly to bone native vascular systems.

Mechanical compression tests on both scaffolds configurations return a Young modulus between 30 and 50 MPa which is in range of recorded failure regimes of bone under impact loading. Furthermore, *in vitro* hMSCs studies showed a better osteogenic differentiation in scaffolds with 0.5 mm diameter channels while HUVECs showed a better growth in 1 mm diameter scaffolds⁸⁷.

The AM TE literature reports processable materials range from the classic metals up to composites (the most studied⁸⁸), which include also e.g. polymer-based scaffolds integrated with nanomaterials fillers^{88,89}. As yet discussed, scaffolds features depend on the class of material and the manufacturing technique chosen; consequently, several authors have been devised to evaluate processing results of two different materials using the same AM technique^{90,91} or two different AM technologies using the same material⁹². These works have as final goal a better understanding of the capabilities of these processes and the quality of specimens which could be manufactured.

Nevertheless, albeit synthetic scaffolds have been the most manufactured so far, recently new hybrid approaches, based on scaffold AM techniques integrated with bioprinting methods, are interesting the TE community. A successful application in this regard was shown by Kang and co-workers. They have described the capabilities of a novel AM system named “integrated tissue-organ printer” (ITOP), as illustrated in figure 2.1(a). This complex platform allows the simultaneous fabrication and accurate positioning, for example, of synthetic polymeric filaments (PCL loaded with tricalcium phosphate nanoparticles) and stem cells-loaded hydrogels, respectively, for a bone TE application. The manufactured scaffold was then implanted in a defective calvarial site demonstrating to properly promote new bone formation and vascularization even in the central defect zone, as can be seen from figure 2.1(b) and (c). The same technology has proved effective in the regeneration of ear cartilage and skeletal muscle defects⁹³.

Integrated AM techniques have showed their power also in complex shaped regions regeneration, such as osteochondral ones. Mekhileri and co-workers have developed a custom-made AM technology; this is combination of a commercial AM machine (BioScaffolder) with a custom-made device capable of handling pre-loaded tissues, as shown in Figure 2.1 (d). These, in the form of spheroids (1 mm diameter), have been successfully positioned into pores generated by voids left by polycaprolactone (PCL) filaments, as can be seen from figure 2.1 (g), previously extruded through Bioscaffolder. The result is a large hybrid construct that could mimic a natural osteochondral tissue, such as the authors demonstrate positioning two different natural hydrogels’ microspheres (bone and cartilage portions) as a proof of concept⁹⁴, as shown in Figure 2.1 (e)

and (f). Finally, *in vitro* culture tests in chondrogenic differentiation media have demonstrated tissues spheroids fusion at 35 days, as illustrated in figure 2.1 (h).

Novel AM applications in TE could be based also on the implementation of new synthetic polymers formulations; for instance, Yang and co-workers has developed a composite poly(glycerol sebacate) (PGS)/PCL blend into which sodium chloride (NaCl) particles are dispersed. This blend, respect to the single polymers, showed mechanical properties closer to the natural heart tissue and, after NaCl leaching, scaffold features resulted improved in terms of neovascularization, thanks to the presence of an additional interconnected microporosity.

The designed cardiac scaffold had a regular crisscrossed structure and was fabricated using a fused deposition modeling (FDM) technology, as illustrated in Figure 2.1 (i). Those precise architectural properties, despite the easiness and low resolution (hundreds of microns) of the technique, demonstrated well-tailored to help a correct cardiac remodelling after myocardial infarction in rodents, with respect to scaffold-free and PCL or PGS only scaffolds, as showed in figure 2.1 (j). Moreover, annular shaped PGS/PCL scaffolds demonstrated to be potentially suitable in applications concerning ventricular dilation preservation, as illustrated in Figure 2.1 (k)⁹⁵.

AM technologies have brought improvements also in the neural TE field, for example in the spinal cord injury regeneration. Koffler and co-workers have implemented a “microscale continuous projection printing method” (μ CPP), as shown in figure 2.1 (l), to fabricate a 2 mm-thick biomimetic scaffold, composed of a mixtures of poly (ethylene glycol) and gelatin methacrylate, in less than 2 seconds. These materials demonstrated to well mimic the spinal cord structure, as illustrated in Figure 2.1 (m) and (n); indeed, the scaffold not only kept its structure over four weeks *in vivo*, even showing a good inflammatory response, but moreover regenerated and improved the pre-existent tissue functions. Specifically, the scaffold was seeded (before implantation) with neural progenitor cells (NPCs) which after 6 weeks *in vivo* greatly contributed in regenerating the host axons, as can be seen from figure 2.1 (o). These were furthermore helped to promote their extension outside the scaffold by the same NPCs⁹⁶.

However, although it was here reported how AM technologies have been demonstrated their power in fabricating scaffolds with precise control over spatial architecture, several issues have limited their widespread translation from the bench to the bedside. For example, as for conventional techniques, several AM technologies process materials in combination with undesirable organic solvents which could be retained inside the scaffold structure⁹⁷; moreover, other limitations are the possibility to process (for some AM

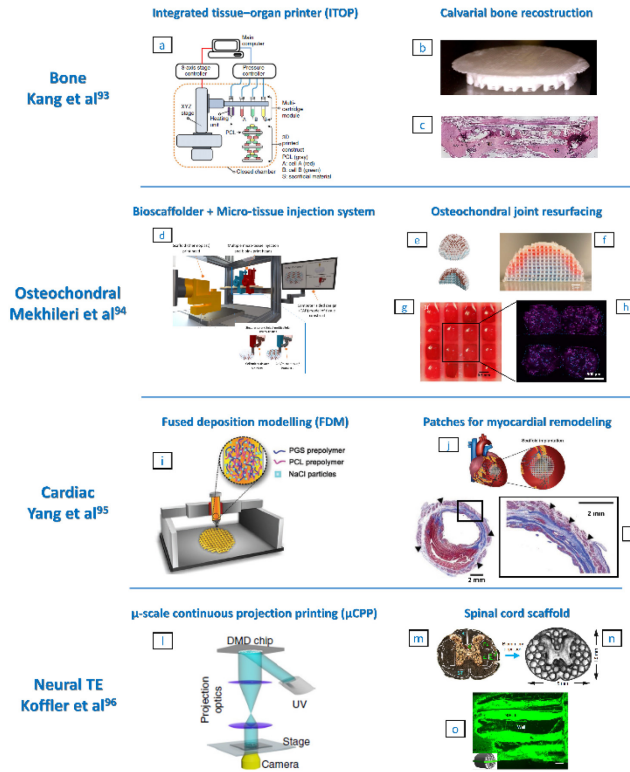


Figure 2.1 (a) ITOP system components and materials. (b) Photograph of the manufactured calvarial bone construct. (c) Histological image of the fabricated calvarial construct after *in vivo* implantation. (d) Image of the bioscaffolder + micro-tissue injection system (inset: working concept overview of the micro-tissue injection system) developed for manufacturing the osteochondral joint resurfacing device. (e) CAD images and (f) optical image of an assembled hemispherical construct. (g) Image of spheroid microtissues positioned into the hemispherical construct and (h) resulting DAPI (blue) and Aggrecan (purple) antibodies staining of the construct showing cells distribution and microtissues fusion at 35 days of *in vitro* chondrogenic culture. (i) FDM machine overview and materials for the elastic cardiac patch fabrication. (j) Illustration of the scaffold implantation site after induced myocardial infarction in rats. (k) Representative Masson's trichrome stained heart section four weeks after implantation. Black box highlights the higher magnification area of the left panel. Black arrows indicate the annular-shaped PGS-PCL scaffolds. Scale bars: 2.0 mm. (l) μ CPP system used to fabricate poly (ethylene glycol)-gelatin methacrylate scaffolds loaded with NPCs for nerve regeneration. (m) Spinal cord structure highlighting fascicles regions (motor systems are shown in green and sensory systems are shown in blue) and (n) the corresponding scaffold. (o) Image of the NPCs-loaded scaffold after four weeks *in vivo* showing channels filled with GFP-expressing NPCs. Figure adapted from MDP¹⁰⁰.

technologies) only specific materials classes, the necessity of developing post – process optimizations and, sometimes, the limited overall scaffolds sizes^{98,99}.

Nowadays, one of the principle limitations of AM processes is the lower resolution (accuracy); indeed, possible resolutions are usually limited to hundreds of microns or maximum tenth of microns for techniques used to

fabricate scaffolds of limited sizes^{98,99}. As described before, several scaffolds furthermore require a controlled architecture in the micron and sub-micron range which several AM technologies do not still guarantee¹⁰¹⁻¹⁰³.

In this context, researchers have evaluated different possible solutions. Initially, there was investigated the creation of bimodal or multimodal scaffolds combining traditional solution or melt electrospinning methods with AM technologies; as an example, Kim and co-workers have developed a combined technology based on a direct polymer melt deposition (which can be considered practically equal to FDM) supported by solution electrospinning. The designed scaffolds were based on a framework of a four-layer PCL woodpile structure with 3 different configurations, as illustrated in figure 2.2 (a): the first one was free of electrospun fiber layers, the second one presented an electrospun fiber layer between the second and the third PCL layer, while the third configuration presented electrospun fiber layers between all PCL layers, as illustrated in figure 2.2 (b) and (c). Cell culture results have demonstrated that both the second and the third configuration have better promoted cells adhesion and proliferation compared to the free electrospun fiber layers scaffolds, with the third one that showed increased cell numbers that were 1.5 times higher (compared to the second scaffold configuration) after 10 days of *in vitro* culture¹⁰⁴. The authors state this effect could be effectively ascribed to the electrospun fibers which recreate the cells typical ECM environment.

The evolution of bimodal scaffolds could be considered the design of multiphasic scaffolds, or rather scaffolds with different regions of pore size and porosity to elicit successful regeneration of tissue interfaces, for instance. An important example could be considered that of Vaquette and co-workers which have designed and fabricated a multiphasic scaffold through a hybrid FDM and solution electrospinning method for periodontal regeneration purposes. The electrospun fibers zone acted as support for the adhesion of a periodontal ligament fibroblast cell sheet, while the FDM zone enabled space maintenance for bone regeneration to occur and biomechanical stability¹⁰⁵.

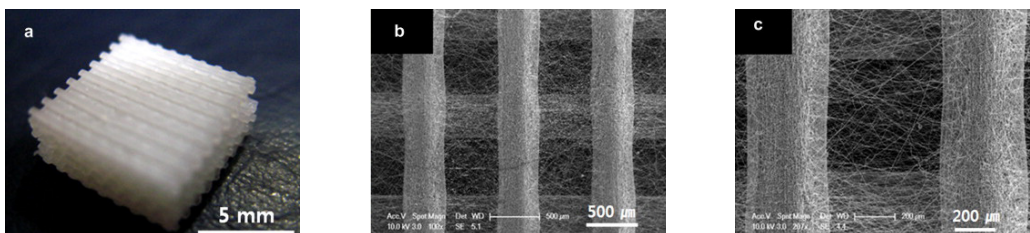


Figure 2.2: (a) PCL composite structure fabricated through AM + solution electrospinning; (b) SEM picture of an electrospun layer deposited on an FDM layer; (c) magnification of an area of figure (b). Reused with permission from Elsevier¹⁰⁴.

Although combining different manufacturing processes has proved an effective approach to create scaffolds with high architectural complexity that more closely fulfil the requirements for several TE applications, new AM methods have allowed scaffolds fabrication with lower filament resolution.

Melt electrospinning writing (MEW) is one of these methods; it was introduced in the early 2010s and helped to fabricate scaffolds with filaments resolution of over an order of magnitude smaller than FDM^{101,106}. MEW is similar to FDM with some distinctions. In MEW a melt polymeric filament is ejected by a spinneret (usually of bigger diameter than an FDM nozzle) using low pressure values compared to FDM. The electrified jet passes through the air, reduces its diameter (as consequence of electrostatic surface charges and the selected process parameters) and it is finally deposited to a collector. The presence of a large air gap, moreover, removes the need for a z movable stage. This technique is gaining an increasing consideration and to date has showed interesting findings mainly considering *in vitro* TE applications. Blum and co-workers have indeed demonstrated the manufacturing of PCL scaffolds with 4 µm filaments and pore diameters of 200 µm using MEW. These were later differently bioactivated to evaluate the better method for the differentiation of hBMSCs using a fixed scaffold architecture and a short-term differentiation protocol. It was found that PCL scaffolds bioactivated with decellularized adipose tissue better promoted hBMSCs differentiation respect to others bioactivation strategies, PCL alone and 2D controls, as supported by greater adipogenic marker expression and protein levels. Such scaffold seems attractive for applications in soft tissue regeneration in reconstructive surgery and as a proadipogenic 3D cell culture platform¹⁰⁷.

hBMSCs behaviour on similar fabricated scaffolds were also studied by Xie and co-workers. PCL scaffolds with a heterogeneous rectangular structure with different fiber spacing and fiber diameters (from 4 to 23 µm) were fabricated with MEW by controlling the printing path. Interaction of hBMSCs with the different structural configurations resulted in different cellular behaviour, as showed by confocal microscopy images, and consequently confirming that the structure could induce specific cell growth and alignment by merely printing different structures in different regions¹⁰⁸.

MEW is not however the unique technology which can fabricate structures with micron or sub-micron features. Integrated approaches, which combine high-resolution 2D structure manufacturing with modular assembly, has been developed and represent a valid alternative option to manufacture and assembly scaffolds using semi-automated two-step (discontinuous) processes. Evidences were yet demonstrated for both *in vivo* and *in vitro* TE and potential

solutions could be implemented also for enhancing scaffolds bioactivation features^{47,52}. The next paragraph will introduce and discuss such technologies.

2.3 Discontinuous processes: lithography

Discontinuous processes in TE have developed when the possibility of implementing microfabrication (and later nano-) technologies and their advancements in the biomedical field was fully understood.

Microfabrication, by definition, is a technology by which a structure with micrometre dimensions and resolution is manufactured; generally, an overall microfabrication process consists of several pertinent techniques (and related steps) used to fabricate the final desired structure¹⁰⁹.

A general classification for micro/nanofabrication methods is based on substrates (or molds) being fabricated and their later use; this classification split molds manufacturing processes into direct and replication methods. In the direct methods, molds patterns are fabricated and the same molds (masters) used to manufacture the desired structures. Differently, in replication methods molds (obtained usually by direct methods) are replicated several times to fabricate new molds and replicas are then used as masters to manufacture the desired materials.

In figures 2.3 and 2.4 it is showed a set of manufacturing discontinuous processes (used in TE) described in current literature. Figures clearly indicate firstly the microfabrication techniques used for biomaterials 2D layers (modules) manufacturing and later the assembly process developed for modules assembly. For each section the main features/outcomes of the fabricated materials are summarized.

2D layers			3D scaffolds		
Fabrication process		Main features	Composition	Layers assembling/bonding	Main outcomes
Consolidation from solution	Polymeric solution casting/phase separation ^{112,113}	<ul style="list-style-type: none"> Layer thickness: 20-100 µm 75% porosity, 2-10 µm rounded pores and 45 µm ridge height 	<ul style="list-style-type: none"> PLLA Cell-free 	C2C12 pre-myoblast cell seeding, manual stacking w/o rolling, external fixation without bonding ¹¹³	<ul style="list-style-type: none"> 4 layers planar or tubular scaffolds In vitro study of cell behaviour in 3D conditions
	Polymeric solution electrodeposition ¹¹⁴	<ul style="list-style-type: none"> Layer thickness: 300 µm Hepatic lobule structure with 1.5 and 2 mm outer diameter 	<ul style="list-style-type: none"> Ca-Alginate RLC-18 cell-laden 	Stacking mould without bonding	<ul style="list-style-type: none"> 600 µm scaffolds thickness (2 layers) In vitro model of liver tissue
	Pre-polymer solution casting followed by thermal curing ¹¹⁵	<ul style="list-style-type: none"> Layer thickness: 100 µm Rectangular pores (500x350 µm²) 	<ul style="list-style-type: none"> AP5 Cell-free 	Dip coating in pre-polymeric solution and manual stacking followed by curing at 165°C for 2h	<ul style="list-style-type: none"> 200 µm scaffolds thickness (2 layers) Struts offset configuration Design of vascularized myocardial grafts by modular assembly of scaffold and microfluidic base separated by a rapidly degradable interface
Thermal processing	Pre-polymer solution casting followed by UV crosslinking ¹¹⁶	<ul style="list-style-type: none"> 87/125 µm thick layers Micropores (362 x 564 µm², rectangular) 	<ul style="list-style-type: none"> PLT32o and PGS Cell-free 	Manual stacking with struts offset followed by solvent treatment and bonding	<ul style="list-style-type: none"> Up to 2 mm thick scaffolds Elastomeric mechanical properties In vitro and in vivo cardiac TE
	Micro embossing ¹¹⁸⁻¹²²	<ul style="list-style-type: none"> Layer thickness: 20 µm¹¹⁸ Layer 1: channels (20 x 30 µm, rectangular)¹²⁰ Layer 2: micropores (20 µm diameter)¹²⁰ 	<ul style="list-style-type: none"> PCGA Cell-free 	Layers plasticization by vaporised solvent followed by stacking chamber and pressing for bonding	<ul style="list-style-type: none"> Up to 60 µm scaffolds thickness In vitro model to study single cell population
		<ul style="list-style-type: none"> 500 µm thick layers Micropores (300 µm diameter)¹²¹ 	<ul style="list-style-type: none"> PCL and SPCL Cell-free 	Layer dipping into polymeric solution followed by manual staking and bonding for 20 min	<ul style="list-style-type: none"> 1.5 mm scaffolds thickness 88% porosity In vitro platform for bone TE

Figure 2.3: discontinuous processes for modular scaffolds fabrication overview scheme. Left side: two-dimensional (2D) layers' fabrication processes using rigid moulds. Right side: three-dimensional (3D) scaffolds' assembly processes and scaffolds main features and/or involved applications.

In TE applications the introduced classification between direct and replication methods is usually overlooked because another based on moulds types is generally preferred; specifically, substrates can be rigid or elastomeric¹¹⁰. Rigid ones (see Fig. 2.3) are usually used as masters in the micro/nanofabrication direct methods while the elastomeric molds (see Fig. 2.4) are usually those used in micro/nanofabrication replication methods. Moreover, another sub – classification, valid regardless of molds' nature (rigid or elastomeric), for structures replication is based on polymers processing (solution or temperature plasticization).

Rigid molds are common materials in several technological processes in polymer science (for instance, injection moulding); this class of moulds is usually fabricated by cleanroom technologies (e.g. photolithography)¹¹¹. Rigid moulds materials, such as silicon, metals or acrylic materials, show advanced stability properties which represent a plus for micro and nanofabrication approaches and have been used for these reasons to fabricate modules also for bottom – up TE purposes. For example, considering layers fabrication approaches by solution–based processes, Papenburg and co-workers¹¹² have implemented a solution casting/phase separation method, labelled Phase Separation Micromolding (PS μ M). Silicon molds were microfabricated and used to manufacture modules firstly casting a polymeric solution on moulds and finally transferring the complete system into a non-solvent bath to consolidate the structure and removing the retained solvents. PS μ M results show that modules had an 80% porosity value and a high pore interconnection (microscopy analyses) but the process generated undesired low closed isolated pores and a minor dense outer residual layer. The main drawback was represented by modules volumetric shrinking (compared to mold features) during the solvent extraction process. *In vitro* biological analyses showed layers are suitable for cell culturing and micropattern design affects the extent of cell alignment and tissue formation.

A preliminary assembly method was introduced: specifically, layers stacking was promoted by clamping modules with retained solvent residues followed by system consolidation in the non-solvent bath. This method proved a preliminary effective strategy for manufacturing cell-free scaffolds¹¹².

In a further work, the authors have developed an alternative cell – based assembly method to fabricate a cell-seeded scaffold; firstly, C2C12 pre-myoblasts cell–laden sheets were fabricated through PS μ M and then these were rolled up and bonded thanks to cell -cell interactions. The final goal was to evaluate the effect of static and dynamic culture conditions on nutrient transport and cell behaviour *in vitro*. Static culturing showed nutrient diffusion patterns while dynamic conditions promoted a better nutrient supply to the

cells improving cell proliferation on all layers, suggesting the scaffolds could be potentially used as *in vitro* platforms for multi-layer tissues fabrication¹¹³.

In another recent example, Liu et al. proposed an electrodeposition process for the preparation of rat liver cell (RLC-18)-laden alginate layers for an *in vitro* liver application¹¹⁴. The process involves the casting of the alginate cell-laden solution onto a rigid mold whose features mimic the hepatic lobule morphology. Then, the solution was electrodeposited for 15 s fabricating 300 μm thick cell-laden alginate layers, whose cells remain viable during all the microfabrication steps and proliferate over time. For sheets bonding, the authors used a pre-designed PDMS chamber for layer stacking; after sheet positioning, cell–cell interactions allowed layers assembly after 1 week. This scaffold holds great promise to be improved further as *in vitro* models of liver organs.

Bottom–up TE has been deeply proposed as a successful strategy for vascular TE purposes. As an example, Ye and co-workers have developed a strategy to build a slowly degradable poly(ester-amide),1:2 poly (1,3-diamino-2-hydroxypropane-co -polyol sebacate) (APS) bilayer scaffold, connected to a microfluidic base through a rapidly degradable porous PGS module, fabricated replicating features of an acrylic mould. These four-layer scaffolds increased the 3D permeability to oxygen and nutrients *in vitro* and degraded *in vivo* with a rate suitable to enhance scaffold vascularization¹¹⁵.

The same group developed an alternative approach with the aim to provide a scaffold with long *in vivo* half-life for cardiac TE. The photo-cross-linkable poly (limonene thioether) (PLT32o) prepolymer was synthesized, characterized and later micromolded to replicate features imprinted into poly(methyl methacrylate) (PMMA) and polycarbonate molds. Layers with rectangular micropores (362 x 564 μm^2) were obtained and subsequently assembled to manufacture 3D scaffolds which demonstrated an elastomeric mechanical behaviour and were able to retain their structural integrity until one month *in vivo*¹¹⁶.

Albeit the discussed papers have presented promising findings both for *in vitro* and *in vivo* studies, highlighted technological drawbacks such as mismatches between designed and real features, presence of undesired closed pores and long procedures for organic solvents removal, whose retention can address cells towards unnatural behaviours¹¹⁷, has suggest to investigate green solvent based or even solvent-free techniques. It is not by chance that polymers thermal processing is generally the main alternative to solution–based layers fabrication processes.

The articles by Ryu and co-workers presents a possible solvent-free method illustrating the development of a micro–embossing technique to fabricate patterned layers with interconnecting structures; the selected materials were

thermoplastic ones, such as poly(lactic-co-glycolic acid) (PLGA), poly (p-dioxanone), and Monocryl®. The authors analysed in depth all the principal technological points, for instance microstructures demolding process and modulation of polymers bulk properties. Morphological analyses demonstrated the possibility of embossing structures of different aspect ratios with such polymers¹¹⁸. The authors developed later a novel custom-made solvent vapor-mediated assembly process to fabricate thermoplastic porous scaffolds. Briefly, two layers were placed in an assembly chamber at a pre-defined temperature followed by a solvent vapor injection. Layers bonding was then achieved bringing the layers in contact under pressure. The main advantage of such process is the possibility to control the amount of solvent vapour which allows to preserve layers' features and eventually incorporate bioactive molecules which are not altered by the process¹¹⁹. Finally, 60 µm thick scaffolds with rectangular pores (20 x 30 µm) were achieved and tested as a 3D platform for single-cells' culture and characterization¹²⁰.

Lima and co-workers demonstrated also the feasibility of manufacturing 500 µm thick PCL and starch-polycaprolactone (SPCL). Modules designed with 300 µm circular pores and 300 thick pillars were replicated from stainless-steel molds through a micro – embossing process and the microfabricated layers were manually stacked and bonded using a PCL solution in chloroform acting as a “glue”. The as obtained scaffolds were 1.5 mm thick with 88% porosity and were used for *in vitro* bone TE purposes¹²¹.

Despite the satisfactory results in micro- and nanoreplication of layers from rigid molds, some disadvantages have not contributed to direct replication methods broad implementation. Firstly, molds patterning (photolithography) needs expensive cleanroom facilities that are not always available and easy accessible; secondly, the rigid suitable materials for mold patterning processes are of a restricted class (such as silicon, glass, or quartz) which are not always biocompatible requiring the implementation of further operations before modules replication can start. Nonetheless, molds need to be usually treated by subsequent etching steps which thereby slow fabrication throughput.

Consequently, scientists have investigated new possible microfabrication technologies to overcome rigid mould limitations in layers fabrication.

Soft lithography (SL), developed in the late 90's by George Whitesides group, emerged as an alternative non-photolithographic set of methods. Several are the advantages that SL demonstrates compared to the standard lithography methods, among which it is possible to cite: the possibility to direct pattern a wide range of materials (from unsensitized polymers to biological macromolecules), the possibility to generate patterns on both planar and

nonplanar surfaces (2D or 3D) but mainly the possibility to implement these fabrication methods outside of cleanroom facilities¹²².

The key idea of SL is substituting rigid moulds with patterned elastomeric molds. Poly(dimethylsiloxane) (PDMS) elastomers, between the others¹²², are the most used ones because they show unique properties related to their chemical nature (presence of an inorganic siloxane backbone and organic methyl groups attached to silicon) which allow a very simple processability for users: the elastomers precursors are fluid at room temperature, thanks to their low glass transition temperature, but can be readily and easily converted into solid elastomers by ultraviolet (UV) or thermal cross-linking steps after being casted onto rigid masters. These are usually manufactured using microlithographic techniques such as photolithography, micromachining or e-beam writing¹²².

Xia and Whitesides motivate the widespread diffusion of PDMS in soft lithography applications explaining a set of advantages^{122,123}:

- Surface with a low interfacial free energy (≈ 21.6 dyn/cm) with a good chemical stability; most molecules or polymers being patterned or molded do not adhere irreversibly to, or react with, the surface of PDMS;
- Hydroscopic; PDMS in fact does not swell with humidity;
- Permeability to gases;
- Good thermal stability (up to $\approx 186^\circ\text{C}$ in air) which allows to cure thermally prepolymers being molded;
- The PDMS elastomer is optically transparent down to 300 nm; prepolymers being molded can also be cured by UV cross-linking;
- The PDMS elastomer is isotropic and homogeneous; stamps or molds can be therefore deformed mechanically to manipulate the patterns and relief structures in their surfaces;
- The elastomeric PDMS is durable when used as a stamp; we can use a PDMS stamp many (>50) times over a period of several months without noticeable degradation in performance. The obvious consequence is the possibility to set up a cost – effective process preserving the quality of rigid master molds;
- The interfacial properties of PDMS elastomer can be changed easily either by modifying the prepolymers or by treating the surface with plasma.

The process generally used to fabricate PDMS stamps for modules fabrication is replica molding (REM). A liquid prepolymer of PDMS is cast against a rigid master whose surface has been patterned using, for instance, advanced lithographic techniques. The relief features on the PDMS mold can consequently

be faithfully replicated by using PDMS itself as a mold for forming structures using a second UV-curable (or thermally curable) prepolymer. Xia and Whitesides have demonstrated replica molding against elastomeric PDMS molds with resolution <10 nm over substantial areas ($\approx 1 \text{ mm}^2$) for an extended number of replica operations (≥ 10) without observation of damage or degradation in patterns quality^{122,124}.

However, PDMS shows also several technical issues. The most important one is related to the aspect ratio of microstructures: in fact, when the aspect ratio (features height/features side) is too high or too low, the elastomeric character of PDMS will cause the microstructures in PDMS to deform or distort and generate defects in the patterns in some applications. Secondly, another technical problem concerns the PDMS elasticity/thermal expansion correlation; this makes it difficult to get high accuracy in registration across a large area and may limit the utility of SL for example in multilayer structures fabrication and/or nanofabrication^{122,123}.

Nonetheless, the advantages of PDMS and SL methods have proved superior than the already explained disadvantages¹²³ and consequently in literature, even in the modular TE field, it is possible to find layers and scaffolds assembly fabrication processes based on SL replication procedures (both solvent and thermal based), as illustrated in Figure 2.4.

Considering the first set of methods, Gallego et al provided a multilayer micromolding technique as a possible technology to fabricate and assemble PCL scaffolds. Modules were fabricated via spin-coating of a PCL solution in

2D layers			3D scaffolds		
Fabrication process		Main features	Composition	Layers assembling/bonding	Main outcomes
Consolidation from solution	Spin coating/ solvent evaporation ¹²⁵	<ul style="list-style-type: none"> ✓ Layer thickness: 10 μm ✓ Dual-scale pores: large ($45 \times 45 \mu\text{m}^2$, square); small ($81 \mu\text{m}$, round) 	<ul style="list-style-type: none"> ✓ PCL ✓ Cell-free 	Manual stacking followed by thermal bonding at 70°C for 2 min under 52 psi pressure	<ul style="list-style-type: none"> ✓ Scaffolds thickness up to 100 μm ✓ 81% porosity ✓ Scaffolds with different layers orientations ✓ Platform for studying <i>in vitro</i> cell/scaffold interactions
	Solution casting/ solvent evaporation ¹²⁷	<ul style="list-style-type: none"> ✓ Layer thickness: 25 μm ✓ Dual scale pores: large ($100 \times 500 \mu\text{m}^2$, rectangular); small ($< 100 \text{ nm}$, round) 	<ul style="list-style-type: none"> ✓ Poly(NIPAAm-co-HEMAHex)/alginate/gelatin ✓ Cell-free 	Manual stacking followed by thermal bonding at 60°C for 10 min under compression	<ul style="list-style-type: none"> ✓ Anisotropic mechanical properties and high stiffness ✓ Myoblasts elongation and orientation along scaffolds patterning
	Solution casting/ freeze drying ^{128,129}	<ul style="list-style-type: none"> ✓ Layer thickness: 2 mm ✓ Dual scale pores: large (500 μm, liver lobe-like); small (100-200 μm, round) ✓ Porosity (70-90%)¹²⁸ 	<ul style="list-style-type: none"> ✓ Silk fibroin-gelatin ✓ Cell-free 	Stacking mould with alignment wires followed by polymeric solution bonding at RT	<ul style="list-style-type: none"> ✓ Scaffolds thickness up to 1 cm ✓ Complex 3D microfluidic channels design
	Solution casting/ Gelatin ^{131,132}	<ul style="list-style-type: none"> ✓ Layer thickness: 500 μm ✓ Dual scale pores: large ($\geq 100 \mu\text{m}$, channels); small ($10\text{-}50 \mu\text{m}$, round)¹³² 	<ul style="list-style-type: none"> ✓ Chitosan-gelatin ✓ Cell-free 	HUVEC or SMC cell seeding, manual stacking, Cell/ECM mediated bonding	<ul style="list-style-type: none"> ✓ Controlled endothelialisation by interactive HUVEC/SMC layers stacking
	Solution casting/ Gelatin ^{131,132}	<ul style="list-style-type: none"> ✓ Layer thickness: 140 μm ✓ Hepatic lobe-like mesh with 300-μm-diameter central pore and smaller cylindrical pores (150 μm distanced)¹³² 	<ul style="list-style-type: none"> ✓ HepG2 or NIH3T3 cell-laden alginate 	Stacking container, Alginate solution bonding with calcium chloride for 30 s	<ul style="list-style-type: none"> ✓ 420 μm thick scaffolds ✓ 3D model for studying cells interaction in co-culture
	Pre-polymer solution casting + UV crosslinking ¹³³	<ul style="list-style-type: none"> ✓ Layer thickness: 200 μm ✓ Hexagonal pores (100-250-500 μm)¹³² ✓ Layer thickness: 150-300 μm ✓ Dual scale-pores: channels luminal section and microstructured pores (10 - 20 μm) induced by porogen leaching 	<ul style="list-style-type: none"> ✓ HUVEC/HepG2 cell-laden collagen 	Stacking container, Cell/ECM mediated bonding after 4 days culture	<ul style="list-style-type: none"> ✓ Construct thickness up to 2 mm and customized modular tissue assembly ✓ HUVEC migration and scaffold vascularization model
Thermal processing	Micro embossing ^{134,137}	<ul style="list-style-type: none"> ✓ Layer thickness: 60 μm ✓ 120 μm wide pores 	<ul style="list-style-type: none"> ✓ PLGA ✓ Cell-free 	hMSCs or mouse ES cells seeding. Manual stacking followed by layers pressing and bonding with high-pressure CO_2 ^{135,136} or N_2 ¹³⁷ at 0.69-1.73 MPa pressure, 37°C for 15 min	<ul style="list-style-type: none"> ✓ Up to 2 cm-thick scaffold ✓ 3D platforms for studying the effect of pore geometry and pore size as well as biomolecules release on tissue growth

Figure 2.4: discontinuous processes for modular scaffolds fabrication overview scheme. Left side: two-dimensional (2D) layers' fabrication processes using elastomeric (PDMS) moulds. Right side: three-dimensional (3D) scaffolds' assembly processes and scaffolds main features and/or involved applications.

tetrahydrofuran and dimethylsulfoxide (1:3:6 w/w/w ratio) at 4000 rpm for 1 min; the residual solvent was extracted overnight. The process demonstrated adequate for manufacturing 10 μm thick PCL layers with 45 x 45 μm^2 pores; the modules were later manually stacked one on top of the other using a thermal based process. Scaffolds characterized by 81% porosity and a thickness up to 100 μm were manufactured and analysed for studying the effect of pores size and architecture on cell behaviour *in vitro*¹²⁵. A similar approach was used by Sodha et al. for preparing PCL scaffolds with 200 μm circular or star-shaped pores for retinal transplantation purposes¹²⁶.

Micromolding demonstrated as an alternative solution for layers fabrication. Rosellini and co-workers in fact fabricated a biomimetic myocardial scaffold based on a simplified model of a natural ECM microarchitecture. Several 25 μm thick layers with 100 x 500 μm^2 rectangular pores were successfully manufactured and thermally assembled to promote layers' bonding and achieve a mechanically stable scaffold which was also able to promote myoblast proliferation, differentiation and alignment in the absence of external stimuli¹²⁷.

Micromolded layers could be also consolidated with other techniques, such as freeze – drying. He and co-workers, indeed, have manufactured 2 mm thick cylindrical layers pipetting a silk fibroin/gelatin solution onto a pre-frozen PDMS mold. The frozen system is then freeze-dried for at least one day to extract the residual solvent simultaneously preserving the fabricated microstructure. This manufacturing technique allowed to modulate layers porosity, in the 70–90% range, and pores size, from 125 to 225 μm , merely changing the concentration of the polymeric solution. The as obtained layers properties demonstrated also to control cell behaviour. A solution-mediated bonding was used to prepare microstructured scaffolds mimicking the liver lobule architecture for liver TE purposes¹²⁸.

A similar consolidation step for modules was used by Wang et al who manufactured porous scaffolds for vascular TE purposes. The authors developed a microfluidic molding method to manufacture 500 μm thick chitosan/gelatin layers (100 μm microstructures thickness) pipetting a 1:1 solution between a PDMS mold/glass slide system. Cooling and freeze-drying steps were used to consolidate the definitive layers structure. An interesting aspect of the method was that, before scaffolds' assembly, the layers were seeded with HUVECs or smooth muscle cells (SMCs) to promote bonding, similarly to Papenburg et al¹¹³, through cell/cell and cell/ECM interactions. Morphological and histological analyses demonstrated the possibility to create a complete branching vascular network and direct SMCs growth into fiber-like bundles inside the microstructured channels¹²⁹. A similar approach was implemented by He et al who manufactured agarose/collagen layers by solvent casting and thermal

gelation. The layers were seeded with HUVECs/collagen suspension, aligned inside an assembly mold, and bonded with the aid of a thin layer of agarose to obtain a fully perfusable 3D construct¹³⁰.

Modules fabrication approaches can be designed to promote, as yet discussed for AM, the deposition of biomaterials and biological matter. Son et al. in this regard used cell-laden solutions and a solution cross-linking assembly step to manufacture a 3D scaffold which mimics the hepatic liver lobule with sinusoids. To achieve this goal, a cell-laden alginate suspension was firstly casted on a plasma-cleaned PDMS mold; later, the system was incubated into a humidifier with a cross-linking reagent to induce gelation. The as manufactured modules well replicated molds features (8 x 8.7 mm² with a maximum thickness 200 μm). Layers were aligned into a custom-made PDMS chamber (the same used by Liu et al¹¹⁴) and bonding was promoted using a small amount of alginate solution and cross-linker at layers' edges. The results demonstrate layers retained their structure during cell proliferation and the manipulation techniques did not result in cell loss. Furthermore, cells show high viability because scaffolds' lateral and central pores were designed to ensure oxygen and nutrients' transport in the entire 3D structure. As specific example, HepG2 cell-loaded scaffolds were manufactured; these exhibited increased hepatic secretion and, when used in combination with mouse embryo fibroblast cell line (NIH3T3), allowed for studying cells interactions in 3D co-culture experiments¹³¹. This manufacturing method was also used to test different porous structures, namely hexagonal pores with size in the 100–500 range, selecting anyway collagen as manufacturing modules material. A patterned cellulose filter substrate was used for collagen layers manipulation and the scaffold was assembled by alternating cell-free and HUVECs-laden collagen sheets to study cells' migration and scaffold vascularization¹³².

Solution-based layers' fabrication was also demonstrated through pre-polymer mixtures which can be consolidated by UV radiation. Zhang and co-workers developed such a procedure for the microfabrication of the AngioChip scaffold. Specifically, modules were designed through a CAD approach and manufactured using a mixture of poly (ethylene glycol) dimethyl ether (PEGDM) and poly (octamethylene maleate (anhydride) citrate) (POMaC) that was injected in a patterned PDMS prior to UV cross-linking and solution consolidation. Finally, the as-obtained layers (5 x 3.1 mm² surface and 150–300 μm thickness) were demolded, assembled, and bonded by an additional UV treatment. The key feature of this micro-construct is the presence of a built-in endothelialized branched network, suitable to assess cardiac and hepatic tissues' responses to drugs delivered through the internal vasculature. For example, the generation of an angiogenic stimulus (thymosin β4) *in vitro*

allowed endothelial cells' migration through the scaffold micro-holes as a first step of blood vessel formation *in vitro*. AngioChip also enabled fast anastomosis *in vivo* and tissue remodeling during the first week¹³³.

The last example of SL approaches for scaffolds fabrication is based on thermal polymers processing, because another considerable disadvantage of PDMS is it can be swelled by several nonpolar organic solvents^{122,123,134}. Yang et al have presented multiple methods to fabricate PLGA/nanoclays composite layers (120 μm wide pores and 60 μm thick) by PDMS micro-embossing at a temperature far from the polymer glass transition temperature. The final porous constructs were obtained by stacking layers with the aid of an alignment mold followed by compressed carbon dioxide bonding for 1 h¹³⁵. This solvent-free approach was successfully applied to cell-seeded PLGA composite layers, demonstrating that CO₂ assembly ensured proper human mesenchymal stem cells viability and functions¹³⁶. Later, Xie and co-workers further demonstrated the possibility of bonding PLGA composite layers using nitrogen, which resulted in enhanced embryonic stem (ES) cells' viability with respect to carbon dioxide¹³⁷.

In conclusion, it has been introduced in this paragraph several discontinuous process for TE scaffolds fabrication. Both natural and synthetic (and even their blends¹²⁷) materials could be processed through solution and thermal based methods to fabricate polymeric and even composite layers¹³⁵. It was demonstrated to be feasible the fabrication of modules with a high controlled architecture using both rigid and elastomeric molds (considering the discussed technological limitations which can consequently limit features accuracy). Resolutions can go beyond the minimum achievable by classical AM techniques (e.g. FDM⁹⁵) and are comparable to newer AM ones (e.g. MEW¹⁰⁸). Cell-free and cell-laden layers could be stacked using appropriate techniques which can moreover potentially allow to manufacture bioactive scaffolds^{119,136,137}. For these reasons discontinuous processes can be considered promising methods to fabricate those new generation scaffolds which require highly controlled architectural and bioactivation properties⁴⁷.

2.4 Aims of the work

Previous paragraphs have extensively documented different available techniques for scaffolds manufacturing, highlighting their advantages and drawbacks, finally focusing in the last paragraph on discontinuous processes. Among these, in the last years SL techniques have been usually preferred rather than direct replication methods (rigid molds) because SL ones have demonstrated several vantages for modules fabrication; nonetheless, PDMS was sometimes used for manufacturing molds for layers assembly¹³¹

demonstrating, moreover, valid results considering the precision of layers alignment.

Consequently, as suggested by the discussed promising findings of discontinuous processes for scaffolds fabrication and, specifically, by the design flexibility offered by SL methods, in this thesis it has been presented the development of a new bottom-up approach for scaffolds fabrication. This will have as final goal the fabrication of a modular scaffolds whose morphological, structural and even bioactivation (spatiotemporal controlled release) properties could be accurately controlled.

The next chapter describes modules and scaffolds design and manufacturing. Firstly, layers features (for instance, filament resolutions, pore sizes and geometries, thicknesses) and scaffolds configurations are presented and *in silico* modelled using a specific CAD software.

Later, layers manufacturing steps are described. PDMS moulds were fabricated using a multistep process like that showed by Carugo and coworkers¹³⁸. Specifically, micromachining techniques - micromilling (μ -milling) - and subsequent SL techniques, such as REM¹²⁴, were used to fabricate the elastomeric PDMS masters. These have later been integrated in a composite assembly structure to fabricate the desired polymeric layers through a novel magnetic embossing process. Briefly, two different assembly components were designed using a CAD software and fabricated by μ -milling. The magnetic force exerted by neodymium magnets, integrated in precise positions of the assembly components, was used to emboss a PCL film into PDMS masters features, at a temperature higher than PCL melting temperature (T_m), to manufacture the designed layers which were later extensively morphologically characterized.

Subsequently, the technique for layers assembly is described. Among all the possible processes, an established solution based method for layers assembly in bottom-up TE¹²¹ was selected after technological considerations. To effectively perform the stacking process, μ -milling and REM processes were used to create a scaffold assembly chamber and several PDMS parts to be used as layers micromanipulation systems. Scaffolds were later manufactured assembling layers one on top of the other using a precise PCL solution as a “glue” to imbibe layers bottom surface before promoting modules physical contact. The manufactured assembly parts helped modules alignment and manipulation throughout the entire process. Two types of scaffolds configurations were fabricated and, later, the as-manufactured scaffolds were accurately characterized from a structural and morphological point of view.

Finally, the last part of the next chapter shows how the as-manufactured scaffolds could be accurately bioactivated presenting DDSs features and the developed microfabrication process for their fabrication. Specifically, PDMS

moulds were firstly fabricated similarly to the processes that will be described for layers manufacturing. Then, micromolding techniques have been used to fabricate semi-hollow structures inside which drugs carriers (drug loaded PLGA μ Ps) have been positioned and sintered, using two different sintering methods. This methodology allows to control both the loading and the release of the encapsulated drug. As an example, the process has been developed using VEGF as a model drug. The modular DDSs were finally morphologically characterized and integrated inside scaffolds to effectively validate CAD design and present an example of potentially bioactivated scaffolds for TE purposes.

Chapter 3: composite scaffolds *in silico* design, fabrication and characterization

3.1 Bottom-up approach scheme

The bottom up approach developed for modules design, fabrication, integration and assembly is summarized in Figure 3.1.

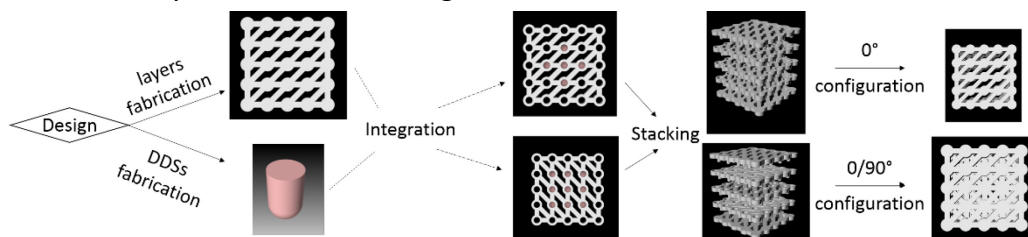


Figure 3.1: bottom-up approach workflow. Images represent renderings of the virtual effective structure of modules and scaffolds.

The first stage deals with the definitive modules and scaffolds features design and their *in silico* evaluation. As figure 3.1 illustrates, two different types of modules have been designed: structural layers and DDSs. The first ones are those which define the morphological and structural features of the final scaffold while the second ones are those which mainly characterize scaffolds bioactivation properties. Modules and scaffolds were *in silico* designed and engineered firstly to acquire preliminary modules and scaffolds data and secondly to use the design data for the fabrication stage.

The second step deals with modules fabrication processes. The structural layers were manufactured by a novel magnetic embossing procedure. DDSs, instead, were fabricated developing a multistep process: a solution micromolding method was used to fabricate external semi-hollow structures into which drug loaded PLGA μ Ps were interspersed (packed) and finally sintered implementing two different processes.

The third step deals with structural and bioactive modules integration. This could be achieved for the as-fabricated modules through the micropositioning of DDSs into the pores of a specific type of layer.

The fourth and last step deals with modules assembly to achieve two different scaffold configurations. For this purpose, a solution-based assembly method was implemented after technological considerations.

In the next paragraphs, the different stages of the introduced bottom-up approach will be analysed. Firstly, layers, scaffolds and DDSs design will be discussed; afterwards, layers manufacturing and scaffolds assembly methods will be presented, and processes results analysed and discussed. Secondly, the dissertation will describe DDSs fabrication methods and present and discuss manufacturing results; finally, the last paragraph concludes this chapter

presenting an example of a potential composite scaffold for vascular TE applications.

3.2 Design stage

3.2.1 Layers

Structural layers were *in silico* modelled in 2D (as a set of lines) and 3D (using functions to extrude solids from 2D lines) using the CAD software Rhinoceros (version 4.0 SR9, McNeel Europe, Spain). Layers renderings and the relative dimensional features are respectively shown and summarized in figure 3.2.

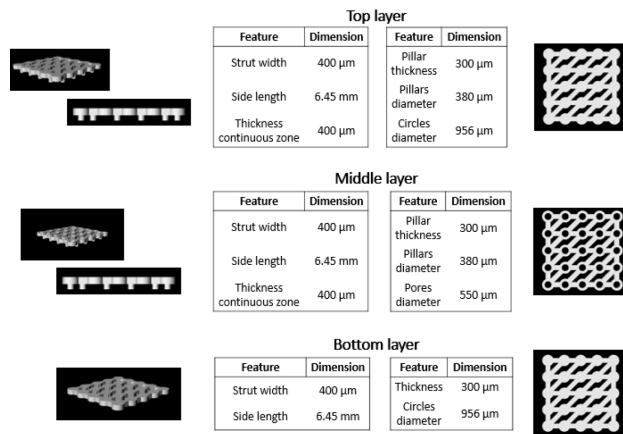


Figure 3.2: layers isometric, frontal and top views (Rhinoceros renderings). Tables summarize dimensions of the main features of layers.

Thus, as follows from the figure shown above, three different type of layers were engineered: a bottom, middle and a top layer. These have the same lateral features (sides are about 6.45 mm), but a different thickness. The middle and top layers, indeed, are 300 μm thicker than the third one layer because the bottom surface of the first two layers is linked in specific positions with 380 μm diameter pillars. These have a double function:

- provide a scaffold lateral porosity (design based consideration);
- allow a safe distance for solution bonding to avoid microfeatures modification (technological based consideration); the middle and top layers indeed will be stacked one on top of the other and this procedure requires a safe distance.

Regardless the difference in layers thickness, the continuous zone of bottom and top layers has similar features (see figure 3.2); instead, middle layers differ from the bottom and top ones in the continuous zone for 550 μm diameter pores, designed for later DDSs integration. Circular pores design allows 25 possible positions for structural layer bioactivation which could generate,

considering only a single middle layer, several possible planar configurations, such as the two depicted in figure 3.1.

The last pivotal feature of layers is filaments spatial configuration; specifically, layers present crisscrossed filaments with an orientation of $0/45^\circ$. This pattern allowed to generate 2 different porosity configurations, as will be described in the next paragraph. The choice of this type of layer structure was inspired by the works, among the others, of Yilgor⁸⁵, Di Luca⁸⁴ and Ahn⁸⁶, presented in the last chapter, which have demonstrated promising results in osteochondral and cartilage TE. Anyway, the presence of circles in bottom and top layers or circular annuli in middle layers generate anisotropic pores. Indeed, layer central areas present modified rhomboidal pores with only two opposite angles of 45° ; pore diameters are thus variable due to the modification of the classical rhomboidal shape by the circular shaped regions. The outer pores, instead, show a simile triangular shaped porosity, where one of acute angles is modified by the presence of the circular shaped regions.

Literature studies suggested the choice of PCL as candidate material for layers fabrication. PCL is of the oldest known bioresorbable polymers; it is biocompatible and could be biodegraded by the human body. Therefore, several medical devices in which PCL was used have been presented to date and moreover PCL was selected as biomaterial in a plethora of TE fields, like bone, cartilage, vascular, cardiac to name a few¹³⁹. Moreover, as described in the last chapter, several manufacturing techniques for modules fabrication has yet demonstrated capable to process PCL^{125,126}, consequently further supporting this selection. Anyway, previous research has not documented the fabrication of layers whose features (mainly thicknesses) are comparable to those already presented; these limitations were exceeded using a magnetic embossing procedure whose steps will be extensively described in the next paragraphs.

3.2.2 3D scaffolds building

Figure 3.3 presents pictures of renderings (generated using Rhinoceros) of the two designed scaffold configurations. The former - 0° or aligned - is based on the sequential assembly of three middle layers and a top layer whose features have always the same orientation; the latter - $0/90^\circ$ or alternated - is based on the consecutive assembly of three middle layers and a top layer where the second and the forth assembled layers are both clockwise or counter clockwise rotated respect to the other layers orientation.

For both scaffold configurations, virtual porosity returns a value of $\approx 57\%$, regardless of the integration with DDSs. Porosity was evaluated comparing the volume of virtual models to the volume of a bulk parallelepiped whose side is

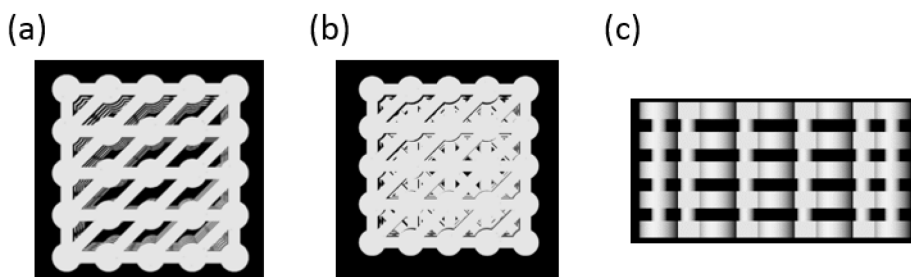


Figure 3.3: top view (Rhinoceros rendering) of scaffolds (a) 0° and (b) 0/90° configurations; (c) frontal view (Rhinoceros rendering) of the assembled scaffolds.

equal to scaffolds one. Calculations were performed using Rhinoceros dedicated function for volume calculation.

Figure 3.3 moreover shows these assembly configurations generate (along the stacking direction) scaffolds with an aligned anisotropic rhomboidal and triangular porosity (0° configuration) or with multiple triangular shaped porosity (0/90° configuration). Similar pore structures were previously fabricated by Di Luca⁸⁴ (0°), Yilgor⁸⁵ and Ahn⁸⁶ (0/90°).

Scaffolds lateral pore shape is, otherwise, equal on all sides of both the presented configurations; the void space between layers continuous zone and pillars is approximately rectangular ($\approx 1 \times 0.3 \text{ mm}^2$) in the central zone, while pores are shaped roughly as squares ($\approx 0.3 \times 0.3 \text{ mm}^2$) on the extrema, as reported in figure 3.3 (c). The integration of a lateral porosity demonstrated advantageous in several TE applications, as discussed in chapter 2; for instance, Ahn et al demonstrated an improved seeding and retention of chondrocytes *in vitro* in poly(propylene fumarate-co- diethyl fumarate) scaffolds⁸⁶; similarly, Holmes and co-workers designed a scaffold whose lateral pore structure demonstrated to enhance blood vessels development in a bone-like scaffold⁸⁷.

Layers were assembled, as briefly introduced in the last chapter, using a solution based process similar to that used by Lima and co-workers to assembly PCL and starch-PCL layers¹²¹, as will be described in a devoted paragraph. This method was implemented to avoid the use of high temperatures^{125,127} which can be detrimental for DDSs stability and due to access restrictions to specialized equipment such as high precision tools^{140,141} or systems based on plasticizing agents like CO_2 ^{136,142}, N_2 ¹³⁷ or solvent vapours¹¹⁹.

3.2.3 Drug delivery systems

The design of modular DDSs was sought as an appropriate solution to implement for the bioactivation of the designed PCL scaffolds to release active drugs both in a spatial and temporal controlled manner. Specifically, we decided to focus on drug loaded μPs to be later packed inside semi-hollow structures

(shells). Figure 3.4 shows a render (generated using Rhinoceros after DDSs 3D CAD using solid-related functions) of one of such shells while table 3.1 summarizes shell features.

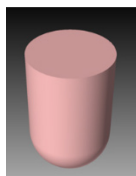


Figure 3.4: isometric view (Rhinoceros rendering) of a DDS shell.

Feature	Dimension (μm)
Shell diameter	540
Shell height	600
Shell thickness	≈ 20

Table 3.1: shells features.

Advancements in micro/nanofabrication technologies have demonstrated of great impact in the design and fabrication of polymeric reservoirs¹⁴³ and microcontainers¹⁴⁴ through, for instance, SL methods. Therefore, multiple polymeric reservoirs can be fabricated in a short time and filled by packing microparticles which could be later sintered - using an appropriate (specific for drug and carrier material) procedure among those extensively described in literature^{73,145} - to create a sintered microparticulate DDS, as presented by the Rhino simplified renderings showed in figure 3.5.

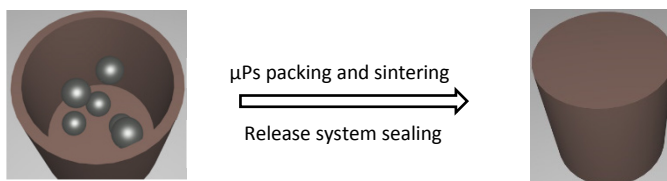


Figure 3.5: Simplified graphical representation (Rhinoceros rendering) for microparticles integration in shells.

As yet described for layers, the requested features for DDSs have necessarily guided materials selection simultaneously with the choice of a suitable fabrication technique. Properties versatility of PLGA such as tunable *in vivo* lifetimes, security for human use and, moreover, the presence of several still developed PLGA formulations for the controlled release of proteins⁵⁴ and other drugs⁵⁶ (also using double emulsions, an established and straightforward μPs fabrication technique^{146,147}) suggested the choice of this polymeric material among the others for μPs preparation.

The material selected for shells fabrication, instead, was gelatin, a denatured protein that is obtained from collagen by acid and alkaline hydrolysis. Gelatin has been used in pharmaceuticals, cosmetics, as well as food products and it is considered as a safe material by the food and drugs administration (FDA). Several DDSs, such as micro/nanoparticles¹⁴⁸ carriers and capsules¹⁴⁹ for the oral drug delivery, were fabricated using this material.

However, gelatin presents a sol-gel transition around 37°C which limits its functionality at higher temperatures. A possible solution is chemical crosslinking. Previous research has documented the preparation of chemical crosslinked gelatin solutions¹⁵⁰ to avoid its fast dissolution in physiological conditions; among these, glyceraldehyde was used as crosslinking agent for its confirmed non-toxicity¹⁵¹⁻¹⁵³.

The overall steps of DDSs fabrication will be described later in this chapter.

3.3 Layers fabrication by magnetic embossing

A magnetic embossing process was developed for manufacturing the structural layers. The selection of a discontinuous method, such as those introduced in chapter 2, has as first stage the fabrication of at least a 2D structured master - in case direct methods - or of several replicas in case of replication methods. A replication method will be described for PDMS masters manufacturing and the resulting molds properties will be presented and discussed. Afterwards, manufacturing processes for the others magnetic embossing components, later assembled with the aim to manufacture the PCL structural layers, will be described. In the last subparagraph, the magnetic embossing fabrication steps will be extensively presented.

3.3.1 Molds fabrication by micromilling and soft lithography

PDMS molds (2 mm thickness) were fabricated through micromachining and SL sequential stages, as shown in Figure 3.6.

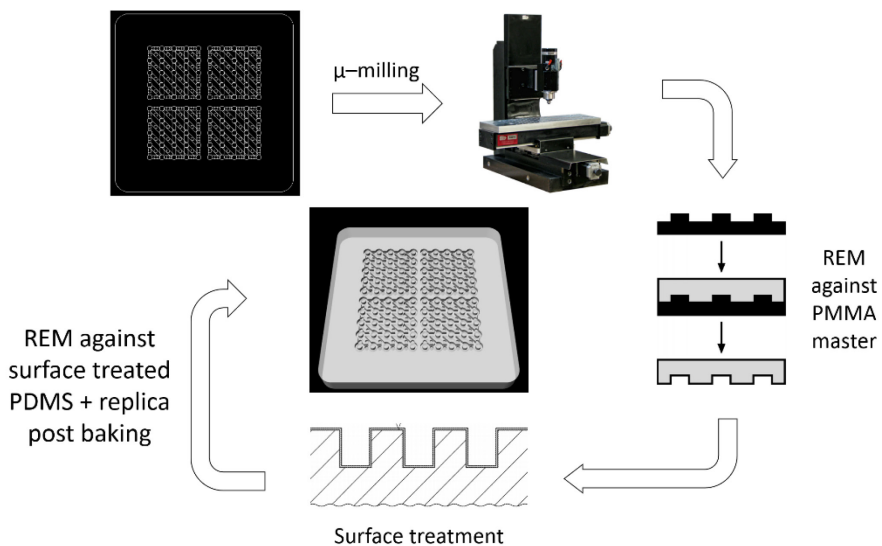


Figure 3.6: PDMS molds fabrication scheme.

The first step was the fabrication of patterned PMMA molds (2 mm thickness, ME303020, Goodfellow Cambridge Limited, England) using a μ -milling machine (Minitech Mini-Mill/GX, Minitech Machinery Corporation, USA). Molds layouts were designed using Draftsight (version 2018 SP1, Dassault Systems, France) and the related machining instructions (.gcode files) were generated using the CAM software Deskam 2000 (version 5.1.5.11, Carken Co. Ltd., USA). Two molds layout were designed: the former for the simultaneous embossing of four middle layers (see Figure 3.6), while the latter for the embossing of two bottom + two top layers.

The following mills (Performance Micro Tools, USA) were used to pattern the PMMA sheet:

- TR-2-0080-S (0.008 inches diameter): cylindrical islands (middle layers mold);
- TR-2-0120-S (0.012 inches diameter): layers channels and holes features (both molds).

For each experiment, machine spindle speed was set to 10000 rpm, feed rate was set to 20 mm/min and water was used as coolant. Among every machining experiment, wipers were used to clean PMMA sheet and coolant replaced. Mills were cleaned dispensing acetone (32201, Sigma-Aldrich, USA) and later ultrapure water (water) (Milli-Q[®], Merck, Germany). A TR-2-0800-S mill (0.08 inches diameter) was finally used for the last part program cutting the predesigned perimeter of the PMMA mold.

Subsequently, PMMA molds patterns are replicated in PDMS using REM processes. Replication procedures were carried out using a method like that developed by Jo and co-workers¹⁵⁴. A specific PMMA enclosure container (which can be used for both PMMA and PDMS molds replication) was previously fabricated using μ -milling; the container is a three-parts system designed with a fixed external shape. The bottom part acts as a base, while the others were designed, respectively, with a central via-hole for molds integration. Each PMMA part (2 mm thickness) was machined using a TR-2-0800-S mill with no coolant; spindle speed and feed rate were 10000 rpm and 20 mm/min, respectively.

To replicate the PMMA molds, a mixture of PDMS 10:1 (precursor:curing agent ratio) (Sylgard 184, Dow Corning, USA) was prepared. The two components were subsequently mixed and degassed for at least 20 minutes into a chamber with reduced pressure to remove trapped air bubbles. Later, a certain volume of this degassed mixture was poured onto the PMMA master in the PMMA replication system (whose pieces were temporally fixed by four 2.5 cm wide binder clips) and trapped air bubbles were removed from master

features with repeated vacuum-degassing cycles into the same chamber. Among cycles, more PDMS mixture was sometimes deposited. Once trapped air was completely extracted, PDMS mixture was added to completely fill the replica system hole. The mixture was subsequently flattened by placing 150 μL PDMS on a previously cut small glass slide (1 mm thickness) (10143562, Thermo Fisher Scientific, USA) which was fixed to the replica system. Finally, the whole system was heated in an oven (VC 20, Salvis Lab, Switzerland) at 80°C for at least 90 minutes to thermally cross-link PDMS^{122,123} and, at the end, the system was disassembled.

PDMS intermediate mould surfaces were then functionalized (silanized) using a patented procedure¹⁵⁵. Briefly, a mixture containing the silanizing agent Fluorolink S10 (Solvay Solexis, Italy) was prepared according to the manufacturer instructions. PDMS intermediate molds were superficially functionalized with a custom O₂ plasma (50 W, 60 s) on both patterned and unpatterned surfaces and then the mold was immediately dipped into 10 mL of mixture for at least 2 minutes. To consolidate the deposited surface film, replicas were left at 100°C for 1h in an oven and later rinsed with 2-propanol (33539, Sigma-Aldrich, USA) to remove the unreacted mixture.

Subsequently, the silanized molds were replicated through a modified REM process. Specifically, a 5:1 PDMS mixture was prepared, mixed, degassed and poured on the treated PDMS molds housed in the PMMA replica system. Vacuum-degassing cycles and PDMS mixture flattening were performed as previously described. PDMS cross-linking was promoted curing the system in an oven at 85°C for 30 minutes¹⁵⁶. The sample was then quickly cooled at -20°C for 15 minutes and the replica carefully peeled from the silanized mold. Finally, the PDMS replica was moved on a polytetrafluoroethylene (PTFE) sheet and thermally aged on a previously heated hot plate (RCT basic, IKA, Germany) at 250°C for 1 h^{156,157}. The PDMS replica was then cooled to room temperature.

A sacrificial layer coating was applied on PDMS molds aimed to simplify the successive PCL layers peeling step. A procedure similar to that of Wu and co-workers¹⁵⁸ was developed for this purpose; Figure 3.7 presents the process workflow.

Preliminary steps were carried out to fabricate PMMA and PTFE components and a polyvinyl alcohol^a (PVA^a) (388406, Sigma-Aldrich, USA) aqueous solution. Specifically:

- a PMMA sheet (4 mm thickness, ME303040, Goodfellow Cambridge Limited, England) was patterned using μ -milling (TR-2-0800-S mill) to generate a 1.8 mm deep zone to accommodate one of the PDMS masters. The same mill was used to pattern a PTFE sheet (3 mm

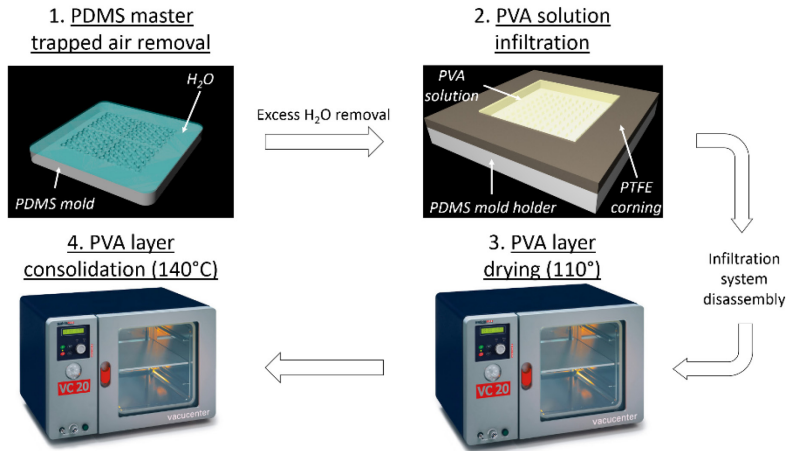


Figure 3.7: PVA sacrificial layer coating fabrication scheme.

thickness, 680-678, RS pro, UK) creating a PTFE frame with a square via hole (18 mm side). Working parameters were 10000/1000 rpm spindle speed (PMMA/PTFE) and 20 mm/min feed rate. No coolant was used.

- A 1% w/V solution of PVA^a in water was prepared: the polymer was dissolved at 80°C under moderate stirring until a clear PVA solution was formed. The solution was cooled to room temperature before use.

To coat molds with a PVA layer, the thermally aged PDMS molds were superficially functionalized with O₂ plasma (50 W, 60 s) on the patterned surfaces and immediately submerged in a room temperature water bath using tweezers. The system was moved in a reduced pressure ambient (oven) to extract trapped air bubbles from PDMS features; then, a sonication cycle in a ultrasonic bath (Labsonic LBS2, Falc Instruments, Italy) at 59 KHz (40% power) for at least 20 seconds was performed to remove the eventually unextracted bubbles. PDMS moulds were then extracted from the water bath and the moulds placed inside the patterned PMMA parts (previously removing the excess water); PTFE frames were immediately fixed with 1 mm wide binder clips and 1 mL of PVA^a solution was poured on each PDMS mold. The system was incubated in a closed petri dish for 10 minutes at room temperature to promote PVA deposition and then afterwards the system was disassembled after the excess solution was removed. Finally, PDMS molds were positioned onto flat PTFE parts and heated inside an oven firstly at 110° for 15 minutes and later at 140°C for 20 minutes to promote PVA layer drying and consolidation, respectively.

Molds were visually inspected using a stereomicroscope (SZX16, Olympus, USA) to assess features quality after each fabrication step. The evaluation of mold features dimensions was carried out using LCMicro, the stereomicroscope dedicated software. Specifically, side-side distance, ridges width, circumferences in bottom/top layers and pillars circumferences in middle layers master after μ -milling, REM and PVA^a coating were evaluated and the related values compared.

Profilometry (Dektak 150, Veeco, USA) measurements were also performed to check variations in features depths during machining and subsequent REM operations of molds with top and bottom layers features. Briefly, molds were fixed by transparent double-sided tape on small glass slides. The same slide was used before measurements for the manual alignment of the profilometer stage to minimize vertical misalignments (values less than 1 μ m). Three linear measurements on two different machined areas were performed on each sample using a 2.5 μ m tip radius. Positions correspondence was guaranteed during measurements on the different samples.

3.3.2 Molds characterization

Visual inspection measurement results of molds are summarized in table 3.2.

Feature	Design (μ m)	PMMA (μ m)	PDMS (μ m)
Side-side distance	6456.40	6294.95 \pm 5.65	6233.75 \pm 8.37
Channels	400.00	388.97 \pm 2.14	386.06 \pm 2.72
Circumferences	956.40	932.17 \pm 3.64	927.83 \pm 1.28
Pillars	550.00	514.92 \pm 2.80	509.60 \pm 2.42

Table 3.2: design values and measurements of mold features analysed using LCMicro. Data are expressed as mean value \pm standard deviation except for design values. The number of replicates (n) is $n=3$ for all molds features except for pillars ($n=4$). The significance level (α) set for the statistical analysis is 0.05.

The results thus obtained demonstrate μ -milling fabrication has determined a reduction in the expected features dimensions (the null hypothesis is indeed always rejected for all the analysed features regardless side – side distances). Specifically, there is a mismatch between features dimensions of about 2.5% while this variation is around 6.5% for pillars. Such higher mismatch value for pillars is anyway in agreement for instance with the results obtained by Carugo and co-workers. The authors machined by μ -milling a PMMA sheet patterning a straight microchannel architecture (design channel width: 254 μ m). Dimensional analyses using SEM demonstrated about 5.5% variation for this feature¹³⁸. Possible suggested explanations for features mismatch could be a

variation of the actual tool size ($\approx 200 \mu\text{m}$) from the nominal value inserted in the CAM program which can have caused pillars overcut¹⁵⁹ or an increased mill flexion¹⁶⁰.

Features dimensions of thermally aged PDMS molds show a shrinkage of about 1%. These results are consistent with other studies which report shrinkages from 1 to 2% for 10:1 and 1:6 PDMS mixtures cured at 80°C for 2 hours^{122,161}. Anyway, statistical analyses do not present significant differences which indicate the REM process do not promote planar features modifications.

Table 3.3 instead summarizes profilometry measurements.

Area	Mold type	Value (μm)
1	PMMA	398.5 \pm 0.6
	PDMS	422.6 \pm 2.3
	PVA coated PDMS	424.9 \pm 1.7
2	PMMA	409.7 \pm 3.1
	PDMS	436.6 \pm 3.4
	PVA coated PDMS	440.5 \pm 3.5

Table 3.3: profilometry measurements on the different moulds using profilometer dedicated software. Data are expressed as mean value \pm standard deviation ($n=3$ for all the measurements). α set for the statistical analysis is 0.05.

The results show a generalized difference between the two areas measured. These results are consistent with the information reported on PMMA material brochure which reports a maximum thickness tolerance of $\pm 20\%$ for all sheets thicknesses, even for the smallest sizes sold ($100 \times 100 \text{ mm}^2$)¹⁶². Therefore, the reported depths variations respect to nominal thickness could explain the statistically significant differences in depth evaluation for the manufactured 20 x 20 mm PMMA mold. Otherwise, the presented data suggest a high machining accuracy for a μ -milling experiment¹⁶⁰; Carugo and co-workers for instance have reported a $\approx 7.4\%$ variation in depth for a machined 100 μm deep channel¹³⁸. These depth differences are inevitably transferred to PDMS molds following REM processes as data summarized in table 3.2 report.

Further variations could be observed following REM steps; specifically, we report height variations of $\approx 6\%$; statistical analysis consider this variation significantly different. However, the results obtained are broadly consistent with the PDMS depth mean value measured by Carugo and co-workers which amounts about 4%. To further improve depth variations during REM, one possible solution to this problem could be the direct implementation of Jo and co-workers' REM system. The authors demonstrated the fabrication of PDMS thin layers of controlled height (less than 100 μm) compressing rigid molds and PDMS mixtures between composite REM systems using C-clamps. However, as

further proved by Moraes and co-workers¹⁶³, this method cannot totally delete height variations in replicas especially if master molds incorporate heights variabilities from previous manufacturing steps, similarly to the data summarized in table 3.2.

Thermally aged PDMS moulds were coated using a PVA adsorption/drying cycle followed by PVA layer thermal immobilization at 140°C. Albeit Wu and co-workers protocol effectively promote PVA deposition, one question still unanswered was whether the deposition and consolidation of one or several layers of PVA alter channels aspect ratios. Trantidou and co-workers developed an experiment to evaluate this aspect¹⁶⁴. Briefly, a PDMS microfluidic systems for droplet generation were fabricated by silicon wafer patterning and SL methods. PDMS microfluidic systems were designed with 400 µm nominal width and 200 µm nominal height. To evaluate channels dimensional variations, profilometry experiments were performed before and after three cycles of PVA flushing (using a protocol similar to Wu and coworkers¹⁵⁸) into the bonded microfluidic system. The results show that PVA deposition does not alter features depth¹⁶⁴. These findings agree with the data shown in Table 3.3 which demonstrate a minimal values fluctuation from thermally aged PDMS measurements and data are not statistically different.

3.3.3 Magnetic embossing

A magnetic embossing procedure was developed to fabricate the structural layers. Several preliminary operations must be implemented before the effective embossing procedure; specifically, the fabrication of the embossing system and the fabrication of PCL films.

A two-component embossing system was fabricated by µ-milling PTFE sheets (3 mm thickness). A TR-2-0400-S mill (0.04 inches diameter, Performance Micro Tools, USA) was used to generate the following features in the first sheet (base):

- 1.5 mm deep area for coverslip integration (22.15 mm side);
- Via holes for magnets integration: (5.15 mm side)

and in the second sheet (counterstamp):

- A 0.3 mm deep area for coverslip integration (22.15 mm side);
- Via holes for magnets integration (5.15 mm side)

In each component, the same mill was used to remove rounded internal corners in each milled edge of the square area and via holes to promote an easier integration of glass coverslips and magnets using the tip suggest by Guckenberger and co-workers¹⁶⁰. Working parameters were 1000 rpm spindle speed, 20 mm/min feed rate and compressed air was used as coolant. Finally, the TR-2-0400-S mill was used to cut the predesigned perimeter of the PTFE

parts. These were then visually inspected by stereomicroscope and the integration with 22 x 22 mm² glass coverslips (# 1.5, Thermo Fisher Scientific, USA) and cubical neodymium magnets (5 x 5 x 5 mm side x side x height) (magnets4you GmbH, Germany) was effectively assessed.

The second preliminary operation was the fabrication of PCL films. PCL (average Mn 45000) (704105, Sigma Aldrich, USA) was sold in form of pellets which consequently must be processed to fabricate the films through a compression moulding technique. Firstly, a PTFE mold was machined by μ -milling to pattern two 13 x 13 x 0.3 mm (side x side x depth) areas using a TR-2-0400-S mill. The same mill was used to cut the predesigned perimeter of the PTFE mold. Effective depths were checked by profilometry analyses. Later, a custom-made two-component compression system were assembled; specifically, components were assembled by using double sided tape to fix a small glass slide onto the centre of a big glass slide. Finally, the as-machined PTFE film mold was fixed using double sided tape on one of the two glass pieces (2947, Corning, USA).

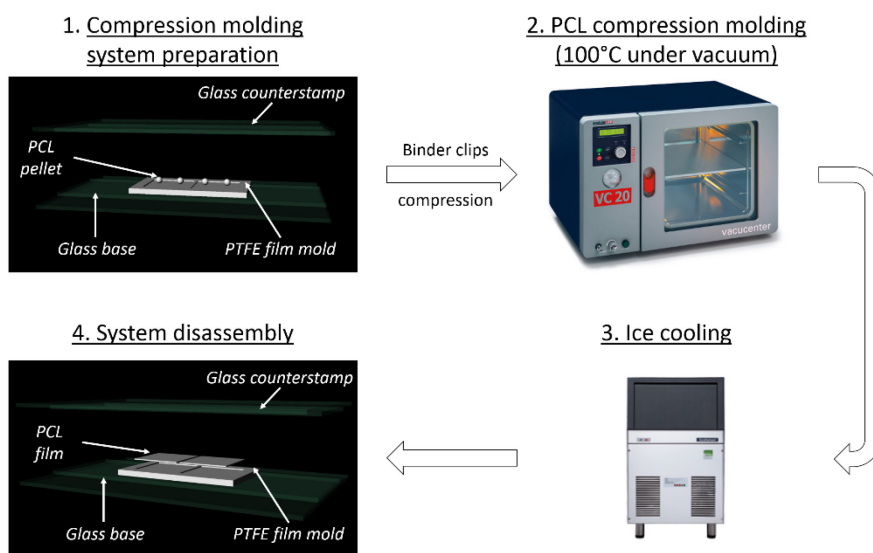


Figure 3.8: PCL films fabrication process scheme.

Figure 3.8 shows the PCL films fabrication process.

Four PCL pellets were accurately positioned onto the PTFE mould. Then, the glass counterstamp was placed above the pellets and the system was temporarily fixed using two 5 cm wide and two 2.5 cm wide binder clips. Pellets were subsequently molten and compressed in a reduced pressure ambient

(oven) at 100°C for 90 minutes. Subsequently, the system was stored in a glass petri dish and cooled inside an ice bath for at least 30 minutes.

Once solidified, films were peeled from the PTFE mold under a stereomicroscope.

Finally, PCL films were characterized by micro-computed tomography (μ -CT) (SkyScan 1172, Bruker, Belgium). μ -CT, like conventional tomography, uses X-rays to obtain projection images (acquisition stage) of a 3D-object. Following a cone beam reconstruction, this data can be later processed to obtain a virtual tomographic model made up of several cross-sectional images of the object under test. The tomographic model can be observed from multiple angulations and moreover can be manipulated to observe samples internal structures, differently from conventional microscopy techniques.

Before magnetic embossing, several PCL films tomographic models were reconstructed and, moreover, analysed in order to quantify molding and embossing quality for PCL films. For this purpose, CT-An (Bruker, Belgium) was used to perform a binarization operation of 2D cross-sections. Binarization is carried out by imposing a threshold on the absorption spectrum of these images to discriminate between air and the absorbing material. The result of this operation is a binary image (0/1 white/black) in which the black and white voxels represent respectively the empty volume and the one occupied by PCL. It is up to the software thus to count white and black voxels obtaining the object-to-void volume ratio and hence porosity.

As the preliminary operations were carried out, it was possible to process PCL film to achieve the structural layers using the magnetic embossing process. This can be split up in three macro steps:

- 1) Embossing system assembly.
- 2) Embossing step.
- 3) System disassembly and layers post – processing operations.

The assembly step allows the sealing of the embossing system whose part are showed in Figure 3.9.

Specifically, PTFE components assembly was achieved as follows:

- double sided tape was applied on the milled side of the PTFE base to cover via holes.
- a glass coverslip was fitted in the patterned zone under the stereomicroscope.
- magnets were finally fixed on the double-sided tape on the other side.

Similar steps were carried out in the case of the counterstamp; however, the double-sided tape was subsequently cut in correspondence of the via holes with the aid of tweezers to allow the easy removal of magnets. Finally, other two

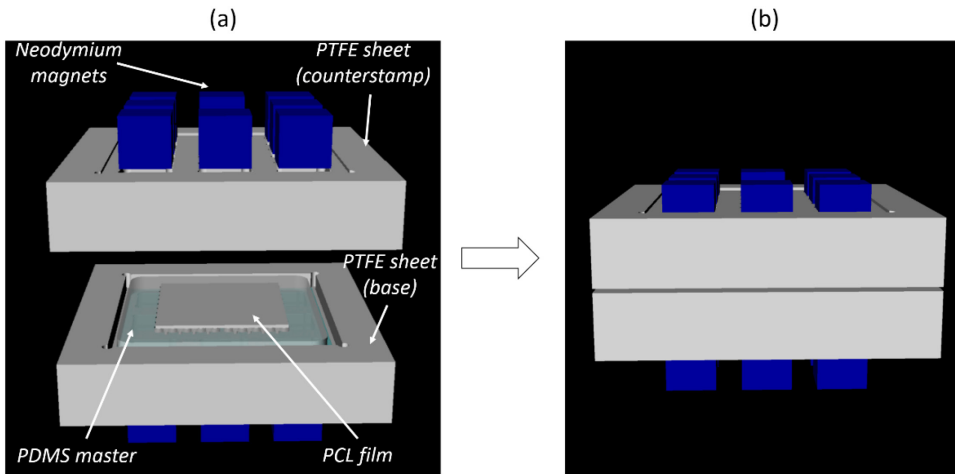


Figure 3.9: magnetic embossing system. (a) exploded-view drawing CAD render. (b) CAD render of the assembled system sealed by magnetic force.

PTFE sheets with via holes were assembled to guarantee magnets stability during the assembly and embossing steps.

To complete system assembly, a PVA coated PDMS mold was positioned onto the PTFE base glass coverslip and a PCL film was aligned to correctly cover PDMS features under the stereomicroscope. Finally, the PTFE base and counterstamp were carefully sealed by the magnetic force.

PCL layers fabrication scheme (representing steps 2 and 3 of the embossing process) is shown in Figure 3.10.

The assembled embossing system was moved in an oven where subsequent steps of chamber depressurization and heating allow the fabrication of PCL

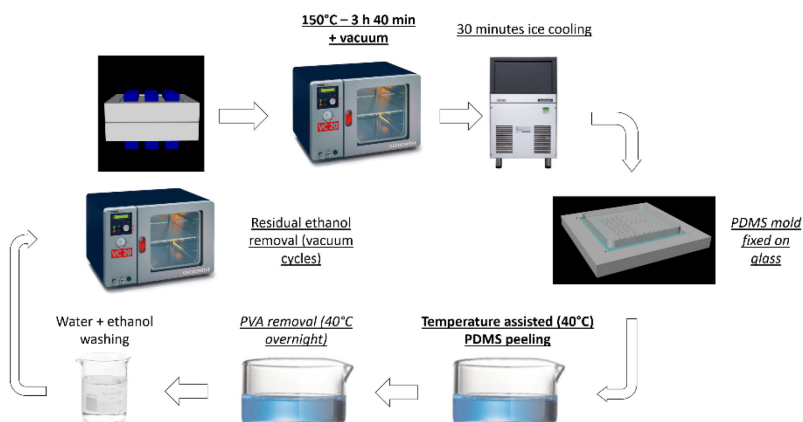


Figure 3.10: PCL layers fabrication through magnetic embossing. Flowchart of the embossing process, embossing system disassembly and layers post-processing operations.

modules; specifically, chamber was depressurized; then, temperature was set to 150°C to promote firstly PCL film melting and later PCL embossing. The transient heat state in the oven chamber lasted around 45 minutes and, once the set temperature was effectively achieved, the embossing system embossed for further 3 hours. At the end, depressurization was slowly removed and the embossing system immediately stored in a glass petri dish to be cooled in an ice bath for 30 minutes.

After the cooling step, the embossing system was disassembled removing magnets from the counterstamp. Layers peeling from PDMS mold was manually performed by cyclic fast dipping steps in a 50°C water bath to soften and remove the residual polymer film around mold perimeter. Finally, the PCL layers, attached to counterstamp's glass coverslips, were left in a 40°C water bath overnight to allow residual PVA dissolution. The next day, PCL layers were washed firstly in a 40°C water bath and subsequently water removed by solvent - ethanol (32221, Sigma-Aldrich, USA) – exchange. Finally, the solvent was removed from samples through several vacuum-degassing cycles at room temperature and the layers stored at room temperature for further characterizations and tests.

3.3.4 Layer characterization methods

Morphology

Layers morphology was assessed by optical microscopy and scanning electron microscopy (SEM) (Ultraplus, Zeiss, Germany).

The stereomicroscope was used to assess qualitatively the embossing quality (presence of residual PCL film and/or evident micromolding defects); moreover, similarly to molds, LCMicro was to evaluate layers features dimension.

SEM was used to confirm data acquired from stereomicroscopy and to better assess layers morphology. This technique can be used to analyse radiodense materials such as PCL and to shoot highly magnified gray-scale images of the studied objects. Aluminium SEM specimen stubs were covered by carbon tape. Layers were conveniently mounted to analyse the features of interest. Then, a (sputter coater) (208HR, Cressington, UK) equipped with a gold target was used to deposit a 30 nm layer of material under an argon atmosphere. Samples were then loaded into the SEM and photographs were acquired at 5 or 10 kV and different magnifications.

Pore structure

Layers tomographic models were reconstructed using μ -CT according to the procedure described in the previous paragraph to ascertain the correspondence among the virtual and effective layers pore structure and to evaluate replica defects (e.g. the percentage of closed pores).

Surface chemistry

Chemical analysis of layers surface was carried out by attenuated total reflection Fourier transform infrared (ATR-FTIR) spectroscopy to evaluate residual PVA onto the samples after the manufacturing process. ATR-FTIR (L1280026, Perkin-Elmer, USA) spectra of the layers in the frequency range of (4,000–700 cm^{-1}) at different washing times were compared to those of neat PCL and PVA films and the main peaks assigned to the specific bonds stretching and bending. The PCL films and PCL layers were manufactured by the already described compression moulding and magnetic embossing methods, while PVA layers were fabricated by solution casting as described elsewhere¹⁶⁵.

Surface topography

Surface topography were analysed through profilometry and Atomic force microscopy (AFM). An AFM (NanoWizard II, JPK Instruments, Germany) was used to acquire images of top layer surface; the dedicated microscope (Axio Observer Z1, Zeiss, Germany) was combined to the AFM to control tips and sample position. Several probes (MLCT, Bruker, USA), with a spring constant of 0.01 N/m, were used in contact mode, in air, at room temperature.

Profilometry measurements were carried out as previously described for molds. Briefly, layers were mounted on small glass slides by double sided transparent tape. After profilometer stage calibration (misalignment < 1 μm) three measurements were carried out on different areas to evaluate surface topography. Linear analyses of 150 μm were performed (using a 2.5 μm tip radius) keeping correspondence as far as possible with AFM areas.

3.4 Layers characterization

A qualitative molding evaluation of PCL films was performed before magnetic embossing experiments. The tomographic models of PCL reconstructed demonstrated minor replica defects (anyway ineradicable albeit compression molding was performed in a vacuum chamber), which however do not compromise subsequent layers fabrication. Consequently, films fabricated at 100°C for 90 minutes were used for the magnetic embossing experiments.

3.4.1 Morphology

Figure 3.11 presents a set of pictures of a bottom layer acquired using stereomicroscopy and SEM.

From this figure it can be seen that the magnetic embossing process allowed the fabrication of layers whose morphological structure strongly resembles the corresponding designed CAD design, showing minor structural defects and/or residual film. Higher magnification pictures – see pictures (b) and (c) - further confirm the previous assertion; indeed, measurements on layers circumferences ($926.10 \pm 3.64 \mu\text{m}$, $n=3$) and layers filaments ($380.98 \pm 2.73 \mu\text{m}$,

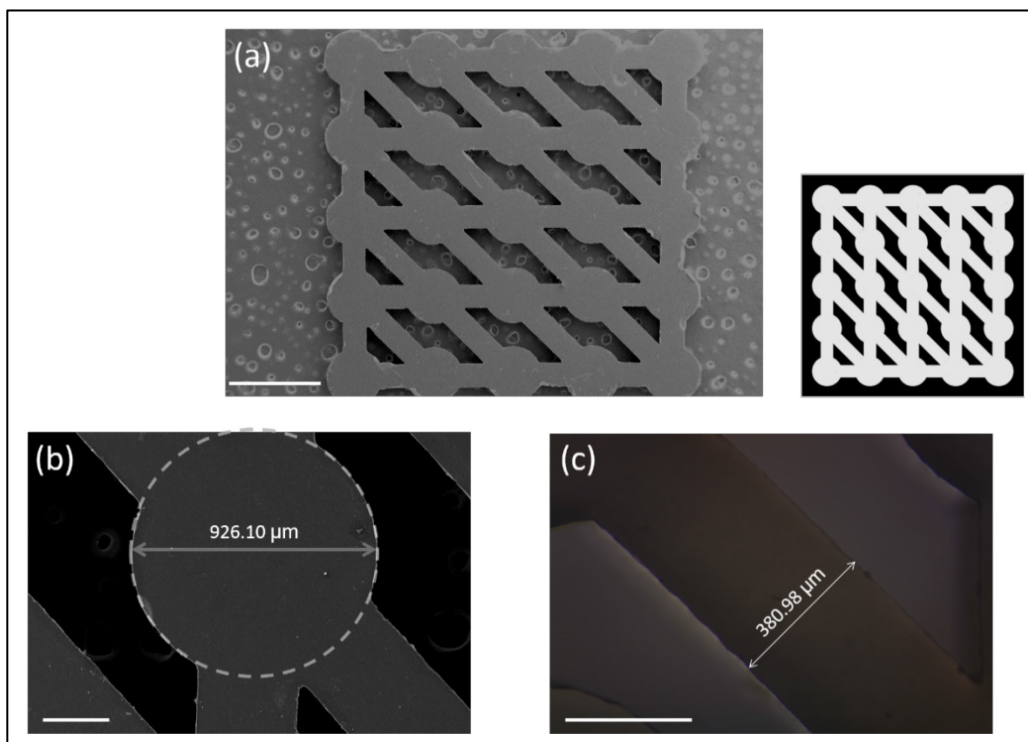


Figure 3.11: typical pictures of a bottom layer. (a) Low magnification SEM photograph of a layer top surface. Scale bar 1.5 mm. (b) SEM photograph of a circular feature with indication of the mean diameter. Scale bar: 250 μm (c) Optical microscopy image of a diagonal filament with indication of mean diameter. Scale: 250 μm .

$n=3$) demonstrate small variations from PDMS thermally aged molds features. This finding represent a significant advance; indeed, previous studies indicated that embossing procedures using PDMS generate samples whose features present significant variations from the original design, as extensively investigate by Lee and Lee¹⁶⁶. Furthermore, as described in chapter 2, Yang and co-workers have demonstrated the fabrication of PLGA/nanoclays composite layers (120 μm wide pores and 60 μm thickness) by PDMS micro-embossing at a temperature far from the polymer glass transition temperature. The main limitation of the experimental results was a high mismatch of features dimension from nominal values¹³⁵. Otherwise, thermally aged PDMS molds fabricated by Kim and co-workers demonstrated an enhanced replication performance. These materials, indeed, proved stiffer ($\approx 45\%$), more stable at high temperature ($\approx 150^\circ\text{C}$) and harder ($\approx 25\%$)¹⁵⁶ compared to traditional 10:1 PDMS molds used to imprint an array of pillars (200 μm thickness and 30 μm diameter) and of a complex channel structure (100 μm width) onto PMMA sheets surfaces. Ren and co-workers, moreover, demonstrated an effective

embossing of PTFE sheets even at 275°C with a resolution up to 100 nm¹⁵⁷. The presented results for the magnetic embossed PCL layers therefore are in good agreement with Kim¹⁵⁶ and Ren¹⁵⁷ studies, as also assessed by SEM and optical microscopy pictures of middle layer top surface and features (see Figure 3.12) which report mean values for pores circumferences and pillars of 509.85 ± 2.15 μm (n = 9) and 317.74 ± 2.15 μm (n=4), respectively.

Albeit PCL structural layers demonstrate generally slight variations respect to design features values, it could be reasonable assert these mismatches could be mainly ascribed to the PMMA molds machining process, which demonstrated the less accurate among the others, and as confirmed by statistical analyses. These indeed demonstrated ($\alpha = 0.05$) PDMS replicas and layers features differences are not statistically different.

In conclusion, magnetic embossing demonstrates as an effective way to fabricate complex microstructures with adequate features accuracy using PCL without the need of expensive platforms or technologies.

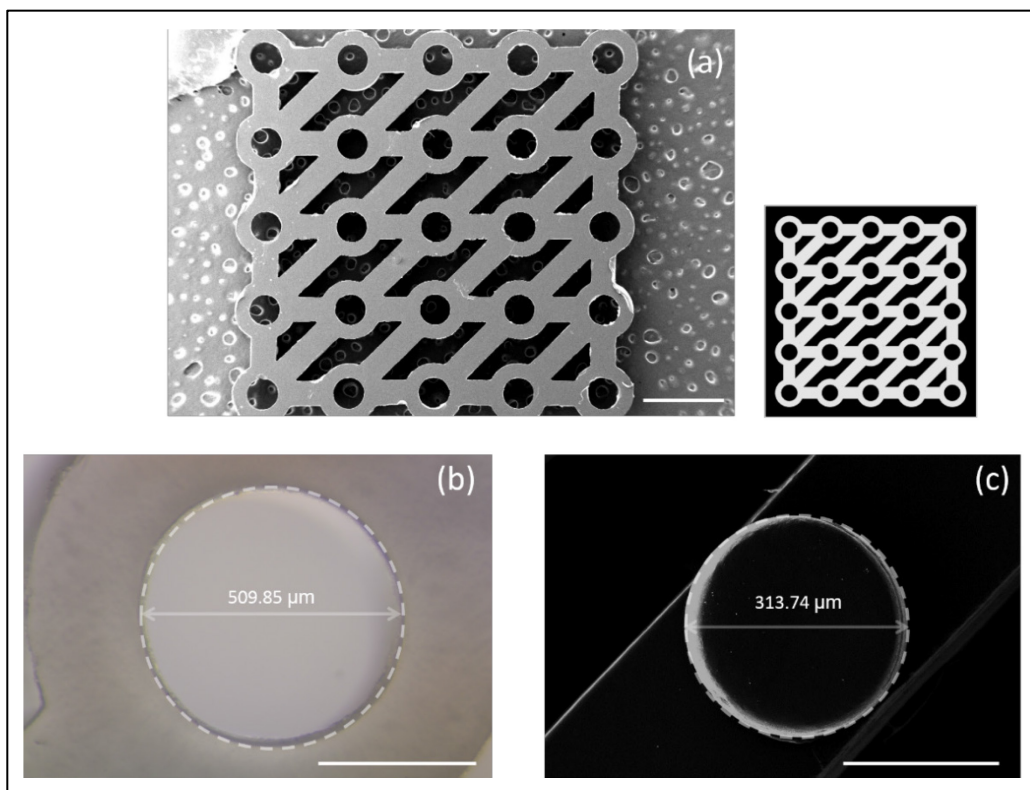


Figure 3.12: typical pictures of a middle layer. (a) Low magnification SEM photograph of a layer top surface. Scale bar 1.25 mm. (b) Optical microscopy image of a circular feature with indication of the mean diameter. Scale bar: 300 μm (c) SEM photograph of a diagonal filament with indication of mean diameter. Scale: 250 μm.

Moreover, it is noteworthy highlight that the presented findings describe for the first time the fabrication of polymeric structures showing via-holes with a thickness of 700 μm or more using PDMS as mold material. To our knowledge, similar thick structures ($\approx 700 \mu\text{m}$ thickness) were fabricated using metal molds^{121,167}. Yang and co-workers indeed, as yet described, showed the fabrication of layers of 60 μm thickness using PDMS as mold¹³⁵, thus approximately an order of magnitude thinner.

3.4.2. Pore structure

Figure 3.13 shows pictures of the tomographic model of a top layer reconstructed using $\mu\text{-CT}$.

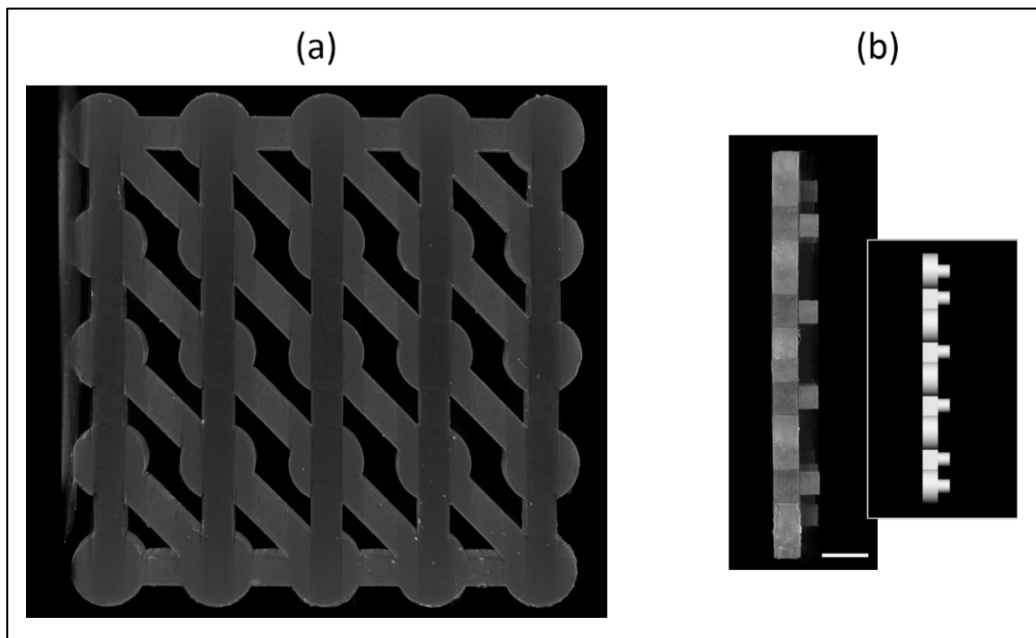


Figure 3.13: $\mu\text{-CT}$ tomographic model of a top layer. (a) Low magnification picture of the top surface. (b) Picture of the lateral view. Scale bar: 700 μm .

As for SEM analyses, despite the lower resolution (down to 1 μm), the 3D volume-rendered model strongly resembles the corresponding designed CAD rendering showing negligible defects. Moreover, figure 3.13 (b) shows a lateral view of the 3D model. The scale bar suggests a good correspondence between the designed and the effective thickness of layers.

Volume-rendered 3D models were also analysed in order to quantify molding and embossing quality for PCL films and layers. For this purpose, CT-An Bruker, Belgium) was used to perform a binarization operation of 2D cross-sections. Binarization is carried out by imposing a threshold on the absorption spectrum of these images to discriminate between air and the absorbing material. The

result of this operation is a binary image (0/1 white/black) in which the black and white voxels represent respectively the empty volume and the one occupied by PCL. It is up to the software thus to count white and black voxels obtaining the object-to-void volume ratio and hence porosity.

Analyses were carried out qualitatively on PCL top layers. These demonstrated a closed porosity of $2.06 \pm 0.80 \%$ ($n=3$). These findings show that compression moulding and magnetic embossing steps adequately process PCL avoiding the generation of a high closed porosity.

3.4.3 Surface chemistry characterization

ATR-FTIR was used to acquire spectra of PCL and PVA (in form of films) and PCL layers. Fig. 3.14 depicts spectra comparison of PCL/PCL and PCL layer (before H₂O treatment).

The IR spectra exhibited characteristic peaks of individual PVA and PCL polymers as extensively described elsewhere¹⁶⁸. For instance, PCL films spectra show characteristic IR bands of $1,721 \text{ cm}^{-1}$ attributed to C=O stretching (str)

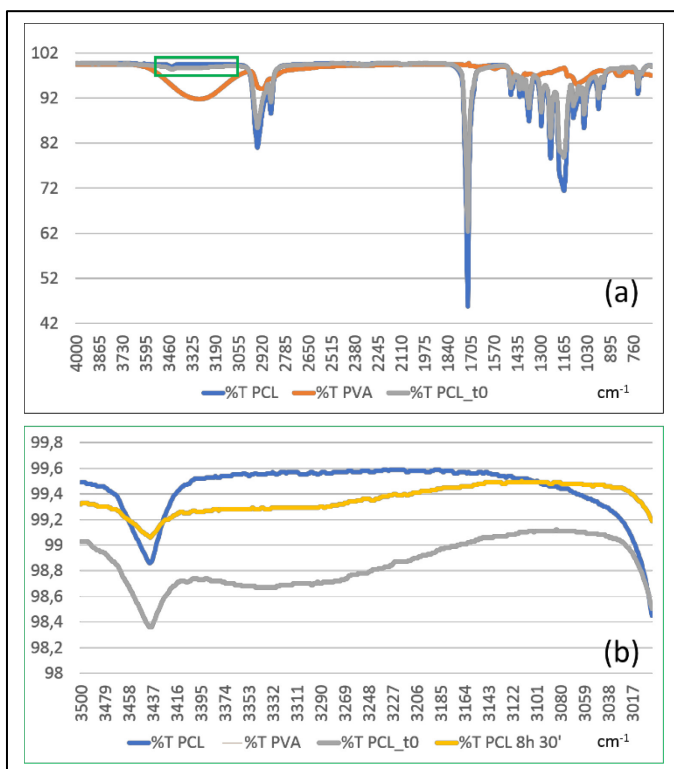


Figure 3.14: ATR spectra. (a) Plot of a typical PCL and PVA film compared with the spectra of an embossed PCL layer before H₂O washing. (b) Magnification of the spectra between 3500 – 3000 cm⁻¹. These are compared with that of a PCL embossed layer after 8 h and 30 minutes washing in a 40°C water bath.

and the $2,941\text{ cm}^{-1}$ attributed to the asymmetric (Asy.str) of CH₂ bands. Simultaneously, the graph shows the characteristic broad peaks for PVA at $3,259\text{ cm}^{-1}$ attributed to OH str and CH₂ vibration (Vib) band at $1,417\text{ cm}^{-1}$.

The analysis indicate a quite similar spectra between PCL film and PCL layers albeit the presence of PVA and pores structure could have generated intensity variations because of the difference in the optical path¹⁶⁹.

Figure 3.14 (b) presents an insight of the ($3500\text{--}3000\text{ cm}^{-1}$) frequency range where – see Figure 3.14 (a) - PVA IR spectra present the characteristic IR band of the OH str. Spectra of pure PCL and PCL layers before and after washing treatment are shown. The graph suggests how an 8 h and 30 minutes washing of PCL layers demonstrates successful to reduce the OH str intensity as compared to the untreated PCL layers. The increase in the intensity spectra can be ascribed to the solubilization of the residual PVA present onto the layers surface. To further assess this hypothesis PCL layers were analysed by SEM as previously described to evaluate their superficial morphology before and after H₂O washes. Figure 3.15 (a) and (b) presents photographs of the bottom surface of top layers in the two different configurations.

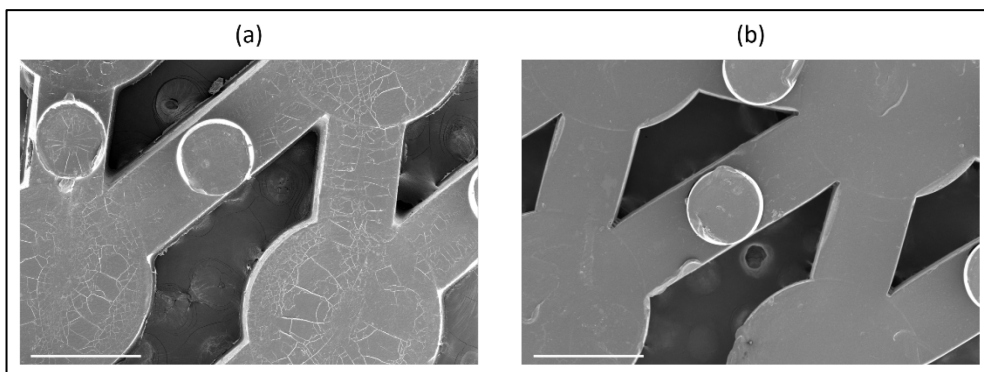


Figure 3.15: SEM photographs of a bottom surface of (a) PCL layer immediately after peeling from PDMS mold (b) after 8 h and 30 minutes treatment in a 40°C H₂O water bath. Scale bars: $500\text{ }\mu\text{m}$.

The visibility of superficial crystal-like structures in figure 3.15 (a) which are otherwise absent in figure 3.15 (b) suggest PCL layers after 8 h and 30 minutes of washing in 40°C water do not present a similar superficial morphology. The most likely explanation of the presented difference could be only PVA solubilization. The presented data concur instead with the work of Aina and co-workers which demonstrate the dissolution of fully hydrolysed PVA (in 250 mL) at 40°C even after approximately 1 hour¹⁷⁰. Considered the high dissolution time, it could be reasonable, as ATR and SEM demonstrate, claim that PVA has almost fully dissolved after 8 h and 30 minutes of treatment in 1.5 L water.

3.4.4. Surface topography

Surface topography were analysed through profilometry and Atomic force microscopy (AFM).

Figure 3.16 (a) presents a typical 3D AFM maps of the PCL samples.

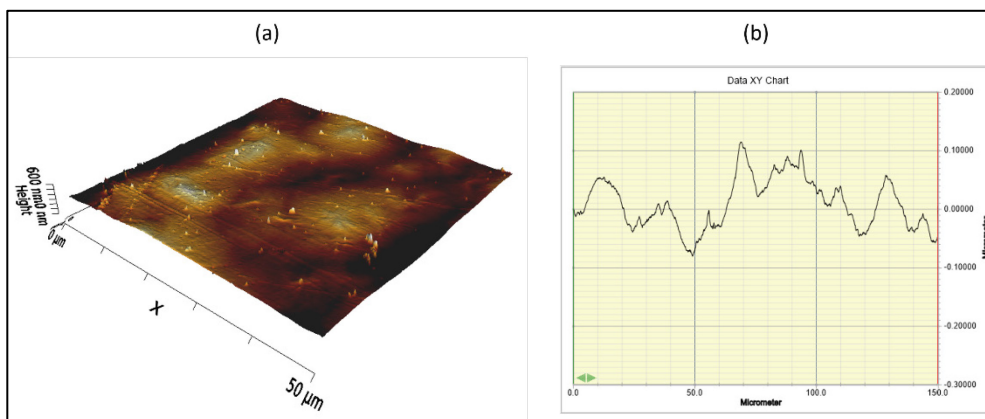


Figure 3.16: surface morphology analyses of a top layer. (a) Typical 3D AFM map ($50 \times 50 \mu\text{m}^2$) of a top layer (b) Typical profilometry curve ($150 \mu\text{m}$) of a similar area presented in (a).

The observations were performed on $50 \times 50 \mu\text{m}^2$ areas evidencing a superficial topography in the submicron-scale as even represented by the z-axis scalebar.

Profilometry measurements were carried out as linear analyses of $150 \mu\text{m}$ (using a $2.5 \mu\text{m}$ tip radius) keeping correspondence as far as possible with AFM areas. A typical profilometry curve for the analysed features is reported in Figure 3.16 (b). Similarly to AFM analyses, maximum variations around 160 nm were measured indicating the data obtained are broadly consistent with AFM analyses, which report a maximum height of $\approx 140 \text{ nm}$.

In-depth assessments were performed to evaluate further surface morphology data. Previous studies indicate that the average surface roughness and surface asymmetry and sharpness indicators, such as skewness and kurtosis, are among the most relevant to evaluate cell-material interaction in TE scaffolds^{171,172}. Table 3.4 presents surface morphology data of interest (average roughness and skewness) of the analysed layers. Kurtosis was evaluated only from AFM analyses.

	Roughness	Skewness	Kurtosis
AFM	39.48 ± 10.34	0.65 ± 0.06	2.51 ± 0.07
Profilometer	30.52 ± 7.59	0.52 ± 0.05	/

Table 3.4: surface morphology parameters (roughness, skewness and kurtosis) evaluated using AFM and profilometry. Data is expressed as mean value of 3 measurements on different areas ($n=3$). α set for the statistical analysis is 0.05.

The overall measurement results support the qualitative evaluations of figure 3.16 and present a mild asymmetry of the surface height distribution respect to the mean plane towards peaks and a slight deviation from sharpness of the surface height distribution towards rectangular-like cross-section.

The presented findings raise questions about comparisons between the two techniques, albeit the two AFM and profilometry could be considered quite similar in the principle and in the analysable data¹⁷³. Wennerberg and co-workers developed an extended comparison of stylus and optical profilometry with AFM for different biomaterials. Specifically, the authors showed that generally stylus profilometry tends to underestimate surface data respect AFM ones.¹⁷⁴ These conclusions are in good agreement with the findings of table 4.3. The statistical data does not highlight significant differences for both roughness and skewness suggesting that for these PCL layers the two techniques present a similar accuracy grade.

It is well known topography can guide cell behaviour. A common classification splits surface roughness in macroroughness (100 μm – millimetres), microroughness (100 nm – 100 μm), and nanoroughness (less than 100 nm). Previous studies indicate that for larger cells, such as osteoblasts and neurons, macroroughness is reasonable, while for smaller cells, such as HUVECs, in contrast, nanoroughness (10–102 nm) could enhance cell adhesion and growth¹⁷⁵. However, only several of the previous studies presents and discuss extended superficial morphology data. For instance, Salerno and co-workers carried out surface roughness and skewness analyses using confocal microscopy on polylactic acid (PLA) and polylactic-co-caprolactone scaffolds fabricated by thermally induced phase separation methods (testing also configurations with or without NaCl porogen). Scaffolds present a superficial rugosity of 50-150 μm and a negative skewness among -1 and 0 which respectively decrease and increase using blend with higher amounts of PLA. The authors demonstrate hBMSCs adheres better on scaffolds manufactured without porogen while cells adequately proliferate on all scaffolds¹⁷⁶. However, a cell-material interaction analysis based merely on superficial morphology was not performed. A more accurate study was presented by Serra and co-workers that manufactured PLA and PLA/PEG scaffolds even reinforced with calcium phosphate particles by AM. Evaluations demonstrated an increase of surface roughness in reinforced scaffolds while a decrease in skewness (from ≈ 1 to -0.5) and kurtosis. Rat MSCs were seeded demonstrating different morphological configurations which however could be ascribed also on a different surface wettability thanks to inorganic particles¹⁷⁷.

To the author's best knowledge, only Takeda and co-workers has studied cells behaviour (rat phenochromocytoma cells) focusing merely on surface

topography. The authors demonstrated that, albeit adhesion was successful at 24h on all the scaffolds configurations, cells were preferentially adhered on scaffolds with decrescent skewness values and similar average roughness. Kurtosis did not seem to affect significantly cells behaviour.

In conclusion, the outcomes presented only suggest that a possible candidate for PCL layers seeding (and reasonably scaffolds) could be HUVECs; however, this conclusion is based only on a comparison of superficial roughness and consequently specific tests will be need to effectively prove this hypothesis.

3.5 Scaffold building by PCL layers assembly

3.5.1 Assembly parts design and fabrication

CAD renders of the of the assembly parts is presented in Figure 3.17.

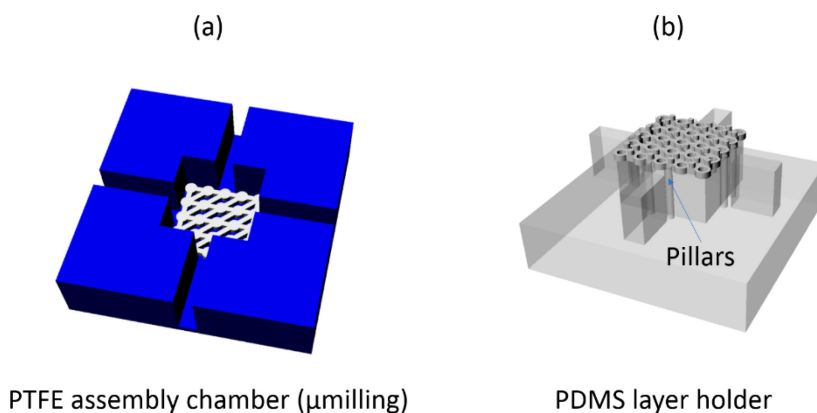


Figure 3.17: CAD renderings of (a) the PTFE assembly chamber and (b) a PDMS layer holder.

As shown in figure 3.17 (a), layers were aligned inside a square cavity (6.4 mm side, 3.8 mm depth) while, as shown in figure 3.17 (b), layers were temporarily bound on PDMS holders by two cylindrical pillars (thicknesses 400 μ m).

The μ -milling machine was used to fabricate the assembly chamber patterning a PTFE sheet (6 mm thickness, 197-0051, RS pro, UK). A TR-2-0600-S mill (0.06 inches diameter) (Performance Micro Tools, USA) was used to mill the assembly cavity while a TR-2-0800-S mill was used to cut the predesigned perimeter of the external piece. A PMMA sheet (6 mm thickness, ME303055, Goodfellow Cambridge Limited, England) was milled to fabricate several different molds to be replicated using PDMS by REM; cavities of different depths (3/2.4/1.7/1 mm) using a TR-2-0400-S were machined considering scaffolds design and the assembly process. Pillars holes (about 1.20 mm diameter) were

patterned using the same mill. A TR-2-0800-S mill was finally used to cut the predesigned perimeters of the external pieces. PDMS layer holders were manufactured using the same REM process previously described (PDMS 10:1, 80°C/90 minutes).

3.5.2. Layers assembly

A 30% w/V solution of PCL in dichloromethane (DCM) (32222, Sigma-Aldrich, USA) and anisole (296295, Sigma-Aldrich, USA) (70/30% V/V) was prepared and the polymer dissolved overnight under moderate stirring at 50°C on a hotplate. Once prepared, a small amount (about 4 - 5 mL) of solution was poured in an 8 mL vial.

To stack PCL layers, a stereomicroscope was used to align a bottom layer inside the assembly chamber, while the other layers (three middle layer and a top layer) were bounded in the specific PDMS holders considering the appropriate orientation to assembly 0° and 0/90° scaffold configuration.

The effective bonding procedure, as summarized in Figure 3.18, was performed under a chemical hood.

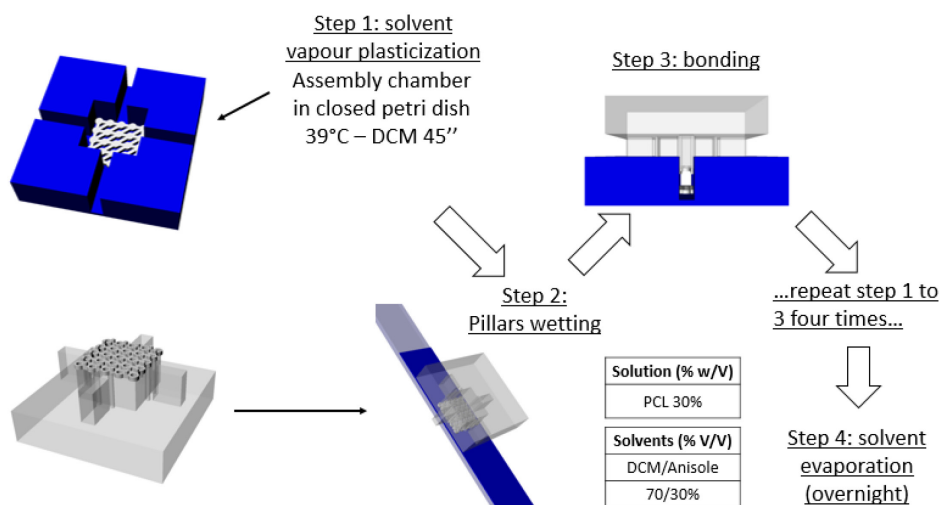


Figure 3.18: layers assembly process flowchart.

Firstly, the assembly chamber was positioned inside a glass petri dish on a hot plate at 39°C for about 10 minutes. Later, a small amount of DCM solution was poured on a small PTFE part positioned in the same glass petri dish. The solvent was used to vaporize and loosen PCL chains of the bottom layer in the sealed petri.

After about 30 seconds, a cut small glass slide (about 8 mm wide) was quickly dipped in the PCL solution in the glass vial. Then, the glass petri dish cap was removed and the PDMS system holder of the first middle layer manipulated to

promote contact among PCL solution on the glass slide and layer pillars. The PCL module was quickly aligned in the PTFE chamber to promote bonding with the bottom layer and the system was left in slight compression using operator hand's fingers for at least 10 minutes.

The process was repeated to stack two more middle layers and a top layer.

Finally, the scaffold was left overnight to promote solvent evaporation and bonding consolidation. Scaffolds were stored at room temperature for further characterizations.

3.5.3 Layer characterization methods

Morphology

PCL scaffolds morphology was assessed by SEM using a protocol similar to that already described for PCL layers. Briefly, scaffolds were conveniently mounted on stubs. A layer of gold (40 nm) was deposited on samples which were then loaded in the SEM. Photographs were shot at 10 kV and different magnifications.

Pore structure

The PCL scaffolds pore structure was analysed by μ -CT using a protocol similar to that already described for PCL films and layers. Briefly, tomographic models of 0° and 0/90° scaffolds configurations were reconstructed and observed from multiple angulations to ascertain the correspondence of scaffolds pore structure with the related CAD models and perform a qualitative evaluation of layers bonding.

Porosity

To quantitatively evaluate scaffolds porosity, gravimetric measurements ($n = 5$) and volumetric analyses of the μ -CT tomographic models ($n = 3$) were carried out. In the former case, a caliper was used to evaluate scaffolds thicknesses and lateral sides distance, while the analytical balance was used to quantify scaffolds mass. These data were analysed to further calculate the effective V_E and theoretical V_T scaffold volumes; the former is evaluated by means of scaffolds mass, while the latter is calculated using the geometrical data measured by the caliper. The equation that describes gravimetric porosity is then as follows:

$$Porosity (\%) = \left(1 - \frac{V_E}{V_T}\right) \cdot 100 \quad (1)$$

Otherwise, to evaluate scaffolds porosity by μ -CT a binarization of the reconstructed images is necessary, as described for PCL films and layers analyses. CT-An counts the white and black voxels, which correspond to polymer and empty volume, respectively. Later, the software counts the white and black voxels and calculates porosity.

Scaffold μ -CT and gravimetric porosity were compared with the theoretical porosity, using a simple geometrical model (yet described in paragraph 3.2.2). Briefly, Rhinoceros was used to evaluate scaffolds cumulative volume - or rather, the sum of volumes of one top layer, three middle layers and a top layers virtually stacked one on the top of the other – in comparison to the volume of a parallelepiped whose side is equal to theoretical side - side distance of layers (\approx 6.45 mm).

Mechanical properties

The mechanical characterization of the assembled scaffolds was evaluated by the commercial MTS installed inside μ -CT, similarly to the procedures described elsewhere^{178,179}. Briefly, 0° and 0/90° PCL scaffolds were loaded in a direction normal to the assembly one onto the lower platen of the μ -CT material testing stage (MTS) and the upper platen was moved closer to the top sample surface. Continuous compression tests on n=3 samples per configuration were performed. During these experiments, MTS lower platen was moved upward up to the maximal compression, corresponding to 222N, without interruption. The loading curve was acquired in real time, so that the relationship between the imposed displacement and stress could be obtained.

Interrupted compression tests were also performed by stopping the compression and scanning the sample to evaluate morphology and pore structure around two predefined areas of the stress–strain diagram. μ -CT analyses were performed as previously described.

Biocompatibility (*in vitro* tests)

In vitro biocompatibility tests were carried out on assembled 0° PCL scaffolds to evaluate cells adhesion, proliferation and migration.

UV radiation was used to sterilize scaffolds for 1 hour. Later, these scaffolds were moved into 48-well plates (392-0061, VWR International, USA) previously coated with 1% gelatin^a (G2500, Sigma-Aldrich, USA). A cell suspension – composed by the cell/tissue culture media Medium 200 (M200) (M200500, Thermo Fisher Scientific, Gibco, USA) additioned with Low Serum Growth Supplement Kit (LSGS) (S003K, Thermo Fisher Scientific, Gibco, USA) - of HUVECs (passage 4) was prepared and 40 μ L (containing \approx 20.000 cells) were seeded on the centre of the external surface of scaffolds top layers (“seeding surface”) in each well. 200 μ L suspension were otherwise deposited in empty wells to be used as control. Cells adhesion was evaluated on scaffolds and control wells by manual counting of cells present on the wells bottom after 6h of static seeding (scaffolds were previously moved in other empty wells where M200 tissue culture media was previously dispensed). PrestoBlue Cell Viability Reagent (PrestoBlue) (A13261, Thermo Fisher Scientific, Invitrogen, USA) was used as

described by the manufacturer with several modifications to carry out an indirect assay aimed to evaluating cells present in wells; later, the assay data were compared to those of the manual counting procedure. Briefly, PrestoBlue was added to microplate wells and incubated at 37°C for 1 hour. Then, a plate reader (EnSpire 2300, Perkin Elmer, USA) was used to evaluate wells fluorescence to plot a curve of relative fluorescence units versus culture time.

Later, static culture on scaffolds was extended up to 72 h and then 7 days to evaluate HUVECs proliferation and migration, which was carried out as already described.

At the different time points, scaffolds were finally fixed using 4% paraformaldehyde and stained with Hoechst (33342, Thermo Fisher Scientific, Invitrogen, USA) and rhodamine phalloidin (R415, Thermo Fisher Scientific, Invitrogen, USA). Confocal microscopy observations (25x magnification) were carried out using a TCS SP5 microscope (Leica, Austria) to qualitatively evaluate adhesion, proliferation and migration on scaffolds.

3.6. 3D PCL scaffolds characterization

3.6.1 Morphology

Figure 3.19 presents a set of SEM pictures of a 0/90° scaffold configuration. From this figure it can be seen that the iterated use of DCM vapours and PCL solution for layers staking have not significantly altered their morphology and pore structures. Indeed, figure 3.19 (a) indicate the top layer morphology and the macroscopic pore structure has not been altered by the assembly process. Moreover, the same figure suggests an adequate alignment between layers as supported by the observation of the external scaffold perimeter. Figures 3.19 (b) and (c) presents higher magnification pictures of the same scaffolds focusing on surface texture and pore structure details, respectively, indicating similarities with the SEM pictures of layers presented in paragraph 3.4.1.

The presented findings are in agreement with the SEM images shown by Lima and co-workers which have previously developed a similar bonding process for PCL modules¹²¹. Albeit the assembly process demonstrated effective for both layers configurations, a closer comparison among the SEM picture showing Lima's scaffold and Figure 3.19 (a) suggest the fabrication of the assembly chamber and layers holders could have effectively reduced dimensional mismatches, which could be more easily observed in the SEM picture of Lima's work.

3.6.2. Pore structure

The PCL scaffolds pore structure was analysed by μ -CT as previously described. Figure 3.20 shows pictures of the tomographic model of scaffolds top surfaces, lateral views and moreover a scaffold virtual section.

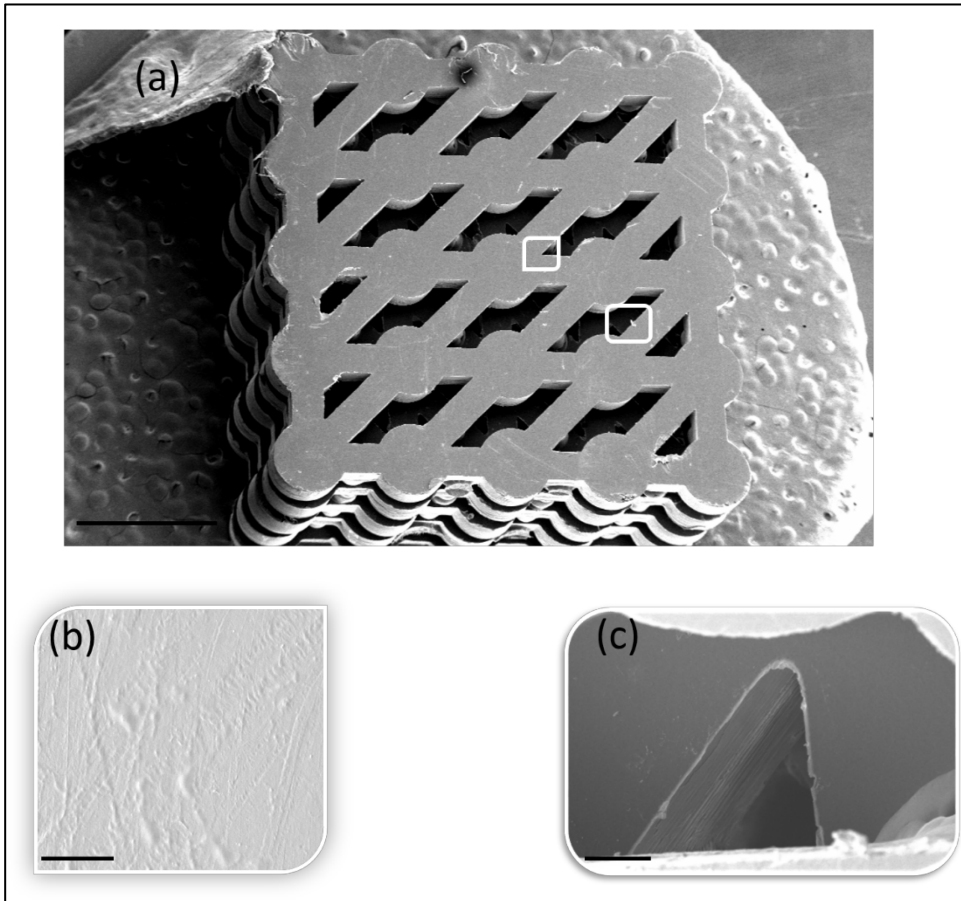


Figure 3.19: SEM photographs of a 0/90° assembled scaffold. (a) Low magnification picture showing the top surface of such a scaffold. Scale bar: 1.8 mm (b) High magnification photograph of the area enclosed by the rectangle with two rounded edges showing a detail of the top layer surface topography. Scale bar: 20 μm (c) High magnification picture of the area enclosed by the rectangle with all rounded edges showing a detail of the scaffold pore structure. Scale bar: 80 μm .

The $\mu\text{-CT}$ model strongly resembles the corresponding designed CAD rendering showing negligible defects. Even the virtual section illustrated in figure 3.20 (d) demonstrate the accuracy of the bonding process. The picture indeed depicts how occluded pores or damaged structures are absent. Finally, figure 3.20 (c) presents a lateral view of a scaffold tomographic model. This picture demonstrates qualitatively how bonding among the continuous area of a layer and pillars of the above module seems effectively achieved. The inset of figure 3.20 (c) further confirms this claim showing a high magnification picture of a restricted area of the tomographic model. Pillars in foreground are effectively bonded to the underlying structural layers filaments and the same results could be observed also for pillars in the background. The results thus obtained are consistent with those of Lima and co-workers, as already discussed

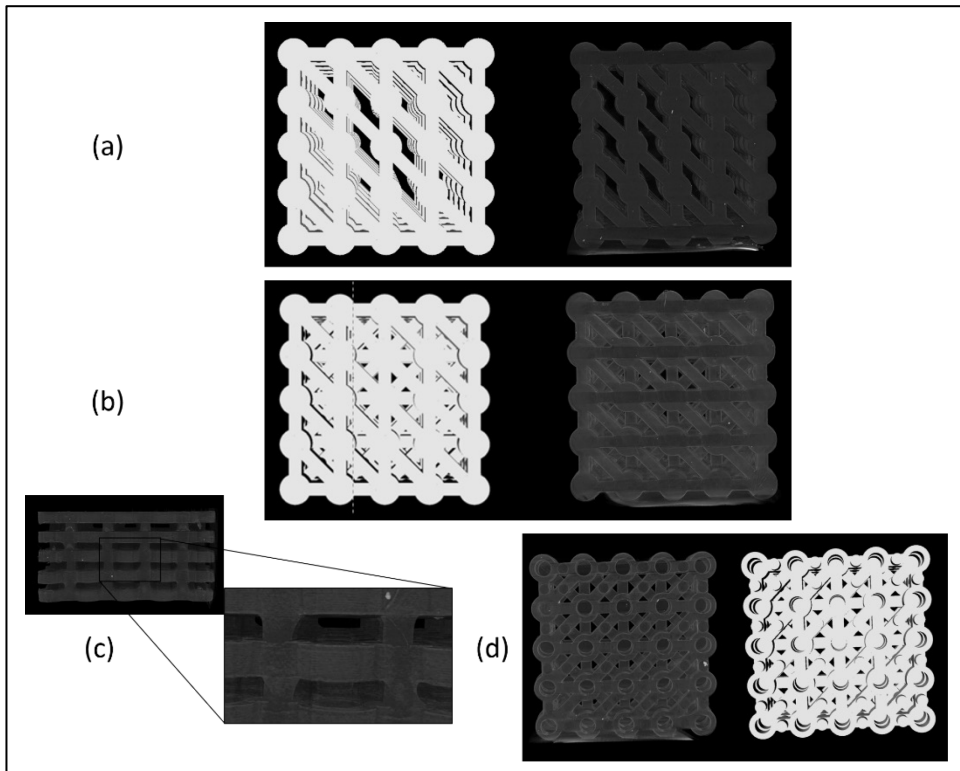


Figure 3.20: tomographic models of assembled scaffolds. (a) 0° configuration. (b) $0/90^\circ$ configuration. (c) Lateral view of an assembled scaffold. Inset: magnification of the boxed area showing bonding between layers. (d) Virtual section of a $0/90^\circ$ scaffold. (a), (b) and (d) show also pictures of the CAD renderings of the analysed structures.

the last paragraph. Even for their scaffolds, the obtained structures were stable and did not present signs of deformation on the pillars as a consequence of the assembly process¹²¹. Anyway, albeit the scaffolds could be effectively straightforwardly assembled, a limitation of the experimental results is that a bonding accuracy of few microns is hardly possible using this type of process. Solutions capable of a higher accuracy were developed by Mata and co-workers which have fabricated modular scaffolds using a mechanical jig (resolution $\pm 30 \mu\text{m}$)¹⁴⁰ for high precision stacking of PDMS microstructured layers and by Kolewe and co-workers which have accurately bonded PGS layers with a resolution better than $0.5 \mu\text{m}$ programming an automated bonder device¹⁴¹.

3.6.3. Porosity

Table 3.5 summarizes the results of porosity evaluation.

<i>In silico</i> (%)	Gravimetric (%)	μ -CT (%)
57.04	56.58 \pm 0.57	57.87 \pm 0.44

Table 3.5: scaffolds porosity values comparison. Measurements are expressed as mean value \pm standard deviation ($n=5$ for gravimetric while $n=3$ for μ -CT analyses). α set for the statistical analysis is 0.05.

Albeit the differences and the limitation of each technique (as reported by Loh and co-workers³⁴), statistical analyses do not support statistically differences among *in silico* porosity values respect to gravimetric and μ -CT values. Otherwise, the same evaluations for gravimetric and μ -CT porosities suggest the null hypothesis should be rejected. The most likely explanation of this result could be an overestimation of μ -CT porosity caused by limitations related to post-processing in the reconstruction phase and/or material and environment thresholding¹⁸⁰, for instance. The nature of the assembly process (use of PCL solution to bond layers) suggests a decrease in porosity, rather than an increase, which supports a slight overestimation of porosity using μ -CT technique.

In conclusion, it is possible to claim the developed two-step discontinuous process for layers fabrication and scaffolds assembly allows to strictly control scaffold morphological (SEM pictures) and pore structure properties.

3.6.4 Mechanical properties

Figure 3.21 presents the typical stress-strain plot for scaffolds and typical pictures of μ -CT tomographic models shot at the end of the elastic behaviour zone and before the densification zone. The stress strain behaviour evaluated by the MTS correspond with the theoretical one, as also confirmed in other works presenting similar scaffolds, such that of Hoque and co-workers. Briefly, stress-strain curves typically followed three distinct regions: (i) a linear elastic region, (ii) a plateau of roughly constant stress, and (iii) a final region of steeply rising stress¹⁸¹ (figure 3.21 inset). μ -CT analyses pictures present, at the end of the linear elastic zone (*), a scaffolds lateral morphology that do not seem dissimilar to the design one. As compression strain increases, the 3D pores of the scaffolds crush and undergo a densification process; the 3D tomographic pictures (#) at the end of the plateau zone show indeed a completely different morphology which substantiate what yet described. Finally, once the rods and struts were crushed, the scaffold become stiffer and the stress level rise quickly until the maximum compression value.

Mechanical tests were performed even to calculate scaffolds Young's modulus. This was evaluated as the slope of initial linear portion of the stress-

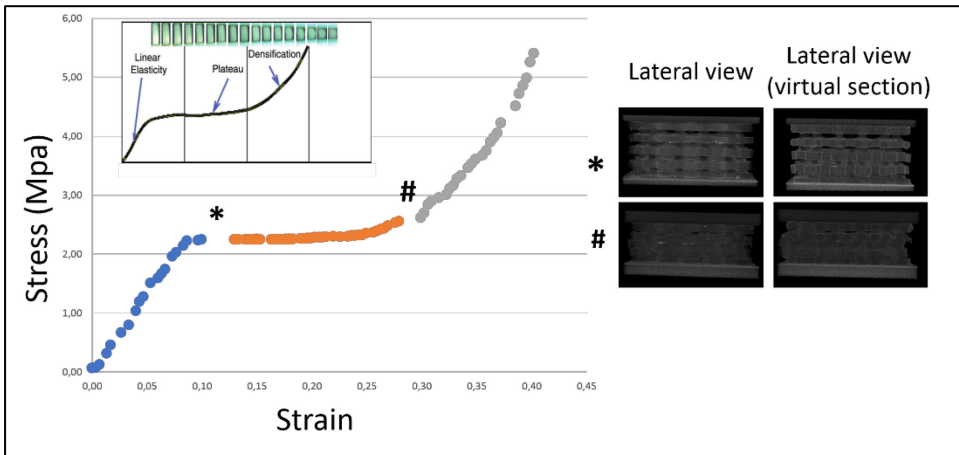


Figure 3.21: typical uniaxial compression stress-strain curve for the assembled PCL scaffolds. Pictures of 3D tomographic models illustrate changes in scaffolds pore structure during compression tests. Images are related to lateral views (external surface and internal surface) of the compressed scaffolds after the linear zone and before the densification zone of the stress-strain curve. Inset: typical uniaxial compression stress-strain curve of a porous structure. Partially reused with permission from Mary Ann Liebert, Inc¹⁸¹.

strain curve neglecting any toe region formed due to the initial settling of the specimen. Table 3.6 summarizes the modulus values of the two different scaffolds configurations.

Albeit the presented data report a variation in the mean Young’s modulus, this represents a minimum mismatch which do not present significant differences and could be ascribed to little differences in the manual layers’ assembly procedure. Indeed, more pronounced differences are visible in scaffolds presenting similar structural properties, such as those fabricated by AM. For example, Holmes and co-workers demonstrate how filaments dimensional variations could generate high Young’s modulus differences (more than 50%) although porosity values are close⁸⁷. Other factors which could affect linear elastic modulus differences in such scaffolds were discussed by Gleadall and co-workers. The presence of staggered structures, repeated layers, multiple lay-down patterns and variations in filament orientation, for instance, regardless of porosity differences or different filaments dimensions (as already described) are all potential factor for Young’s modulus variations⁸².

	Scaffold 0°	Scaffold 0/90°
Young’s modulus (MPa)	29.28 ± 2.23	26.85 ± 3.10

Table 3.6: scaffolds Young’s modulus evaluated after uniaxial compression tests on both scaffold configurations (n=3). Measurements are expressed as mean value ± standard deviation. α set for the statistical analysis is 0.05.

Although the designed 0° and 0°/90° scaffolds show several of these effects, truthfully pillars are bounded during each assembly step always in fixed positions. Therefore, the discussed effects can hardly motivate this restrained variation in Young’s modulus between the two scaffolds configurations.

Uniaxial compression tests were carried out even along directions orthogonal to the stacking one to evaluate scaffolds bonding behaviour. Briefly, the stress strain curve presents an upward trend up to strain values of ≈ 0.1 mm/mm where scaffolds fails due to layers delamination, as expected.

Previous studies have discussed possible applications for such scaffolds considering the presented mechanical behaviour. Eshraghi and Das have for example extensively studied AM PCL scaffolds mechanical properties. The results obtained have indicated as possible applications that of bone TE, specifically such scaffolds have compressive moduli and ultimate compressive strengths values which fall within the lower range of those reported for human trabecular bone ($1 \leq$ elastic modulus ≤ 5000 MPa, $0.1 \leq$ ultimate compressive strengths ≤ 27.3 MPa)¹⁸² and, as demonstrated also by Holmes and co-workers, potentially even for vascular TE purposes⁸⁷.

3.6.5. Biocompatibility (*in vitro* tests)

Table 3.7 summarizes mean values of HUVECs adhesion and proliferation at the different time points. Cell number reported in the “scaffolds” row were evaluated mainly by the manual evaluation procedure and validated by PrestoBlue data.

	6h	72h	7d
Controls	18500 ± 513	76500 ± 436	280000 ± 764
Scaffolds	11700 ± 2200	32433 ± 2926	145000 ± 2207

Table 3.7: biocompatibility *in vitro* quantitative evaluation. Data showed are mediated on n=3 samples per type. α set for the statistical analysis is 0.05.

These findings demonstrate a successful adhesion ($\approx 58\%$ at 6h) which confirms scaffolds biocompatibility. Moreover, the presented results suggest the effective HUVECs proliferation over time on the modular PCL scaffolds (statistical analysis report significative differences).

Confocal microscopy photographs - see Figure 3.22 - support the data previously shown. Cells effectively adheres and proliferate on scaffolds layers. Moreover, the presence of events of cellular mitosis (extensively visible in photographs shot at 7d) qualitatively supports proliferation data. These seems very promising findings for a such long time point. Finally, cellular morphology showed in several areas by figure 3.22 (b-c) indicate how seeded cells adhere and proliferate in all layers not only onto layers filaments but also spreading onto

layers pores. An evidence is illustrated by the cells stretched morphology of figure 3.22 (b) right. The presented cellular behaviour is in good agreement with the finding presented by Xie et al for additive manufactured PCL scaffolds with regular structures. HUVECs adhered on PCL filaments always the same way regardless of designed dimensions; then, adhered HUVECs formed a circle, and ultimately filled the pores once the proliferation reaches a sufficient grade. This cellular behaviour is normal as demonstrated by CD31 and VE-cadherin expressions which suggest promising angiogenesis capabilities¹⁰⁸.

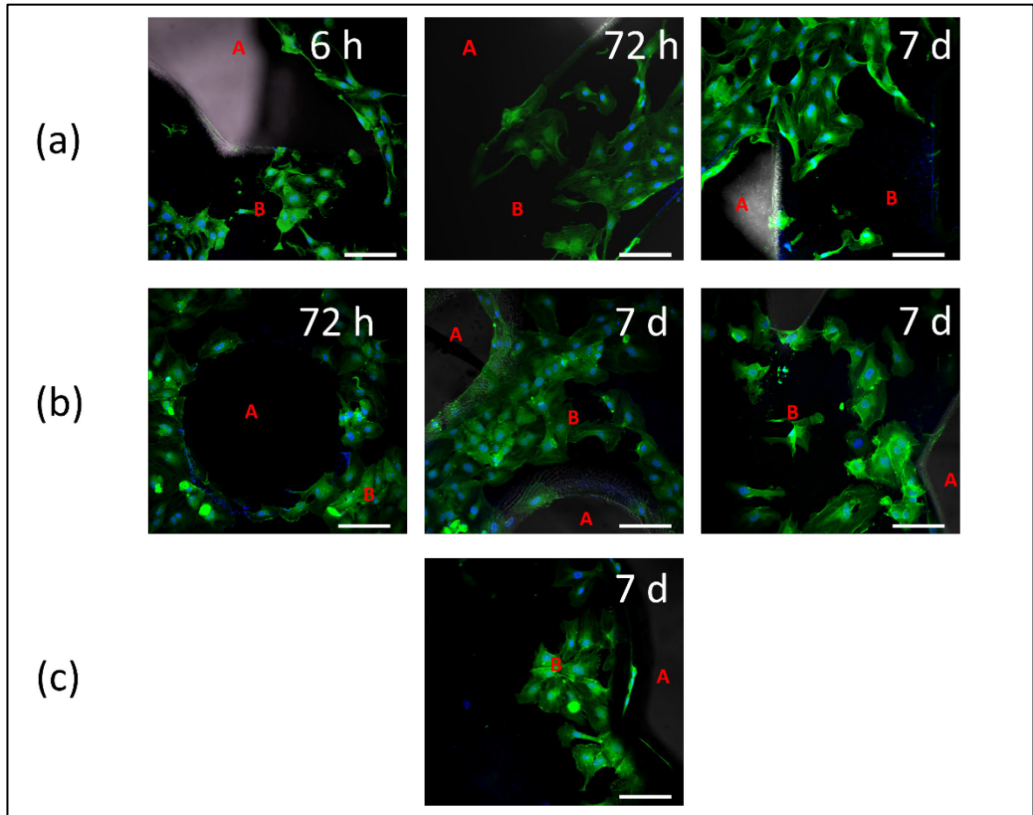


Figure 3.22: confocal microscopy pictures of a 0° scaffold (nuclei staining: Hoechst; cytoskeleton staining: rhodamine phalloidin). (a) 6h - 72 h - 7d pictures of scaffold's seeded surface. (b) 72h - 7d pictures of middle layers surfaces. (c) 7d pictures of the internal surface of a bottom layer. Scale bars: 123.5 μm .

3.7 Drug delivery systems

3.7.1 Vascular endothelial growth factor – loaded poly(lactic-co-glycolic acid) microparticles by double emulsion

VEGF loaded μ Ps preparation is a multistep process whose main stage is represented by the water-in-oil-in-water emulsion procedure. However, several preliminary steps must be performed. Firstly, μ Ps preparation starts with the as bought VEGF (in form of powder) processing and will be completed only once the prepared μ Ps are dimensionally and morphologically characterized.

Freeze-dried VEGF (100-20, PeproTech, UK) was firstly centrifuged at 13'000 rpm for 45 seconds in a microcentrifuge (MicroCL 21R, Thermo Scientific, USA) and then dissolved (reconstituted) in sterile water to achieve a 0.1% w/v (1 mg/mL) solution. For VEGF extended storage, a buffer solution, specifically a 0.2% w/v bovine serum albumin (BSA) (A-7030, Sigma-Aldrich, USA) solution in sterile phosphate buffered saline (PBS) 1x, was prepared and used to dilute the VEGF aqueous solution to 0.05% w/v (500 μ g/mL). Several 20 μ L aliquots (ratio VEGF/BSA 1:2) were then distributed in different 0.5 mL Protein LoBind tubes (0030108094, Eppendorf, Italy) and stored at -20°C for further operations.

To effectively prepare VEGF-loaded μ Ps, a 0.5% w/v PVA^b (Mowiol[®] 40-88, 324590, Sigma-Aldrich, USA) water stock solution was prepared as previously described while the following solutions were freshly prepared shortly before the double emulsion steps:

- 0.97% w/v (9.7 mg/mL) BSA in water;
- 0.1% w/v (1 mg/mL) heparin sodium salt (Hp) (H3149, Sigma-Aldrich, USA) in water;
- 15% w/v (150 mg/mL) PLGA (Resomer[®] RG 504 H, Evonik, Germany); in DCM (1 mL).

Later, a VEGF/BSA aliquot was thawed and sequentially 10 μ L of Hp solution and 70 μ L of BSA solution were dispensed in the VEGF/BSA solution tube to prepare a 100 μ L VEGF/BSA/Hp solution (ratio VEGF/Hp/BSA 1:1:70). Immediately, this solution was aspirated and dispensed into the PLGA/DCM solution and the first emulsion was generated using the high-speed homogenizer (T25 digital Ultra-Turrax[®], IKA, Germany, tool 8G) operating at 15000 rpm for 2 minutes. Immediately, the emulsion was added to 10 ml of the 0.5% w/v PVA^b solution and immediately emulsified at 8000 rpm for 1 min (tool 8G) to produce a multiple emulsion. DCM evaporation and subsequent microsphere hardening were carried out firstly pouring the double emulsion in a low-form 250 mL beaker with 30 mL 0.5% w/v PVA^b solution and further agitating the solution using a overhead stirrer at room temperature for 3h (RZR 2102 control, Heidolph, Germany, impeller BR 10). Later, microspheres were

collected, washed two times with water by centrifugation (4°C, 4500 rpm, 15 min) (SL 16R, Thermo Scientific, USA) and freeze-dried overnight (0,01 mbar, -60 °C) (Alpha 1-4 LSC, Martin Christ, Germany). At the end of the freeze-drying processes, μ Ps were distributed in several Safe-Lock tubes and stored at -20°C for further operations or characterizations.

3.7.2. Microparticles characterization

μ Ps were dimensionally and morphologically characterized.

Methods

The mean diameter and size distribution of μ Ps were determined by laser light scattering (Mastersizer 2000, Malvern Instruments, UK, tool Hydro 2000S) on a dispersion of freeze-dried μ Ps in 0.5% w/v PVA. Measures were performed once achieved a laser obscuration value of about 3% and the considered granulometric distributions and mean diameter values resulted from an average of 3 measures of the same dispersion. The definitive mean value \pm standard deviation was evaluated considering the average measurements generated following the analysis of three different batches (n=3).

SEM observations were performed to evaluate μ Ps superficial and internal morphology.

In the latter case, a PMMA mold (4 mm thickness) was machined by μ -milling to pattern several 30 x 5 x 3 mm (length x width x depth) isolated structures. PDMS 10:1 was prepared as previously discussed and the volume of liquid mixture to approximately cover half of the depth of one structure was poured, degassed and cured at 80°C for at least 30 minutes. Later, a small amount of μ Ps was mixed with PDMS using tweezers onto the spoon of a small spatula and degassed in a reduced pressure chamber. The mixture was finally poured onto the previously cured PDMS and the system flattened as previously described using a large glass slide. Finally, PDMS mixed with μ Ps was cured for at room temperature at least for 48 h. Finally, thin PDMS layers were cut using a razor blade.

Several small amounts of μ Ps and several layers with μ Ps sections were mounted on aluminium stubs coated with carbon tape. These were later sputter coated with a 45 nm gold layer. Samples were then loaded in the SEM and photographs were shot at 10 kV and different magnifications.

Results and discussion

A typical particle size distribution curve is given in Figure 3.23.

The graph suggests, due to the well-known intrinsic nature of double emulsion batch processes, the presence of few smaller particles between 1 and 10 μ m and no bigger particles up to 100 μ m. The graph represented is thus broadly consistent with the mean calculated diameter which correspond to

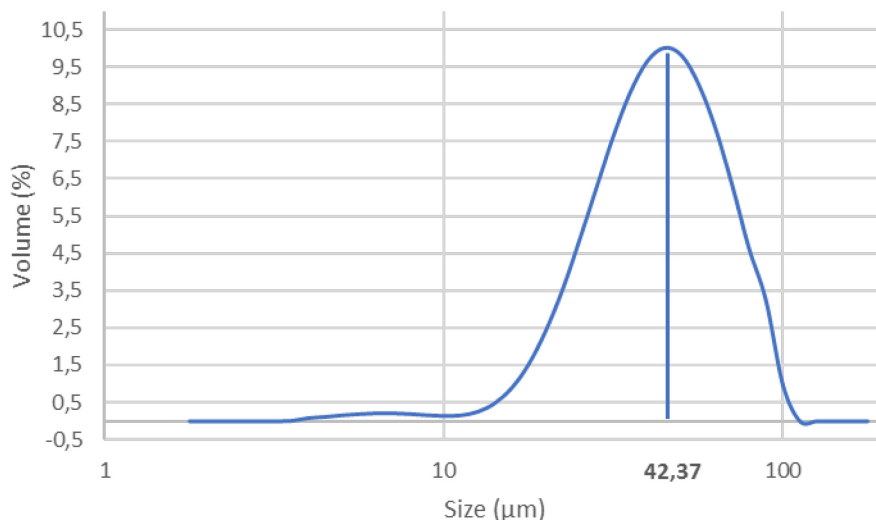


Figure 3.23: typical particle size distribution of the freeze-dried VEGF-loaded μ Ps.

$42.37 \pm 2.15 \mu\text{m}$. The findings are in good agreement with the VEGF loaded PLGA μ Ps prepared by Borselli and co-workers which have used a similar method. Indeed, they report a $21.5 \mu\text{m}$ mean diameter respect to a design value of $20 \mu\text{m}$ ¹⁸³.

Figure 3.24 presents the superficial and internal morphology of μ Ps. Figure 3.24 (a) aims to show the size distribution while figure 3.24 (b) aims to emphasize the superficial morphology of a typical μ P. The two photographs demonstrate PLGA μ Ps are spherical and have a closed superficial porosity. These characteristics suggest the capability to initially limit a burst release of the loaded VEGF respect to μ Ps illustrated by d'Angelo and co-workers. The authors' SEM pictures indeed present an evident surface porosity with a mean pore diameter of $5 \mu\text{m}$ ¹⁸⁴. These differences in μ Ps could be reasonably ascribed in differences in the PLGA amount (100 mg vs. 150 mg) dissolved in DCM albeit manufacturing parameters have been fixed.

Considering the internal morphology, it has been found the presence of a dense pore network, which goes from the inside to the surface of the μ Ps – see figure 3.24 (c) – which suggests the potential controlled release of VEGF according to drug diffusion mechanisms through the innate PLGA micro- and nanopores and the macroporous structure of the μ Ps prepared by the emulsion technique⁵¹.

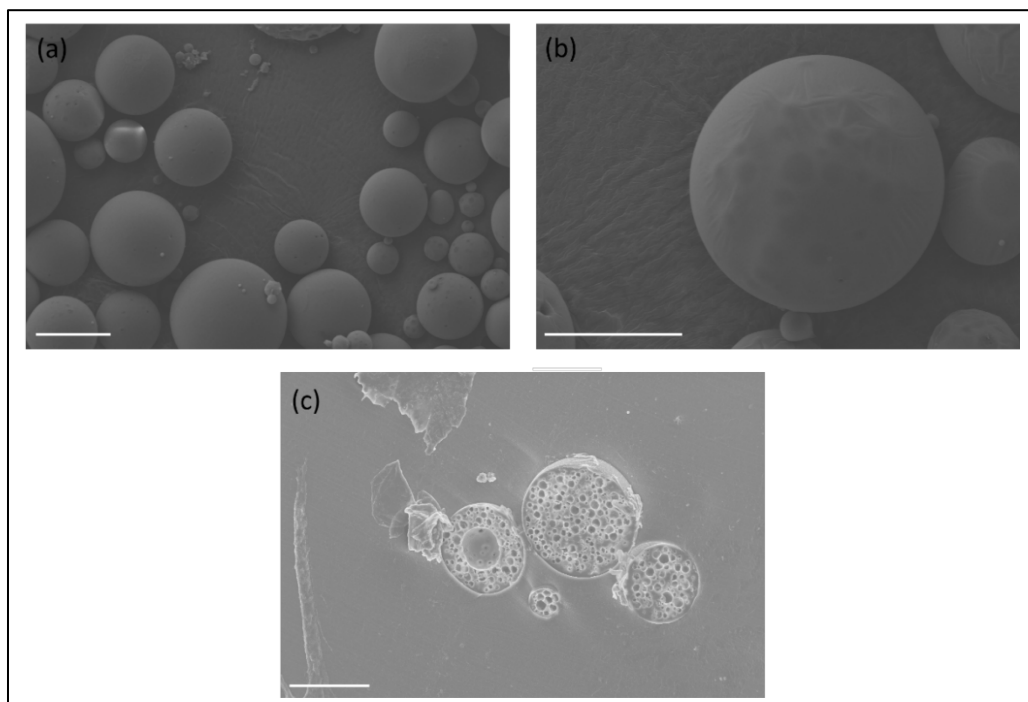


Figure 3.24: SEM photographs of VEGF loaded μ Ps prepared by double emulsion. (a) Magnification of the μ Ps distribution. Scale bar: 40 μ m. (b) Magnification of single μ P. Scale bar: 20 μ m. (c) Magnification of a PDMS layer including section of different μ Ps. Scale bar: 40 μ m.

3.7.3. Drug delivery systems external shells fabrication

The second stage of DDSs fabrication dealt with the external shells fabrication through SL methods.

Micromachining and SL steps were carried out to fabricate the PDMS master for shells fabrication, similarly to the procedure described for structural molds manufacturing. Briefly, the μ -milling machine was used to pattern a set of 540 μ m large and 600 μ m deep holes on a PMMA sheet (4 mm thickness). A TR-2-0200-BN ball-nose mill (0.02 inches diameter, Performance Micro Tools, USA) was used to achieve contoured features. Working parameters were 10000 rpm spindle speed and 20 mm/min feed rate, respectively. To pattern large hemispherical bottoms, a planar step size of 5 μ m was set. A TR-2-0800-S mill was used to cut the predesigned perimeter of the PMMA mold.

Later, an intermediate elastomeric mold was fabricated through REM (PDMS 10:1, 80°C/90 minutes) and subsequently its surface was modified using the previously described silanization process. Finally, a modified REM process was implemented to manufacture a hydrophilic PDMS master¹⁸⁵. Briefly, a 10:1 (precursor:curing agent ratio) PDMS mixture was prepared as previously

described; later, a 2% w/w amount of Silwet L-77 (Momentive, Germany) was poured inside the PDMS mixture which was again mixed. Thus, the mixture was poured as previously described and the hydrophilic PDMS consolidated at 60°C overnight, then disassembled and visually inspected using a stereomicroscope.

Shells were fabricated using a micromolding method, as shown in figure 3.25, similar to that used for PVA coating of the structural layers molds.

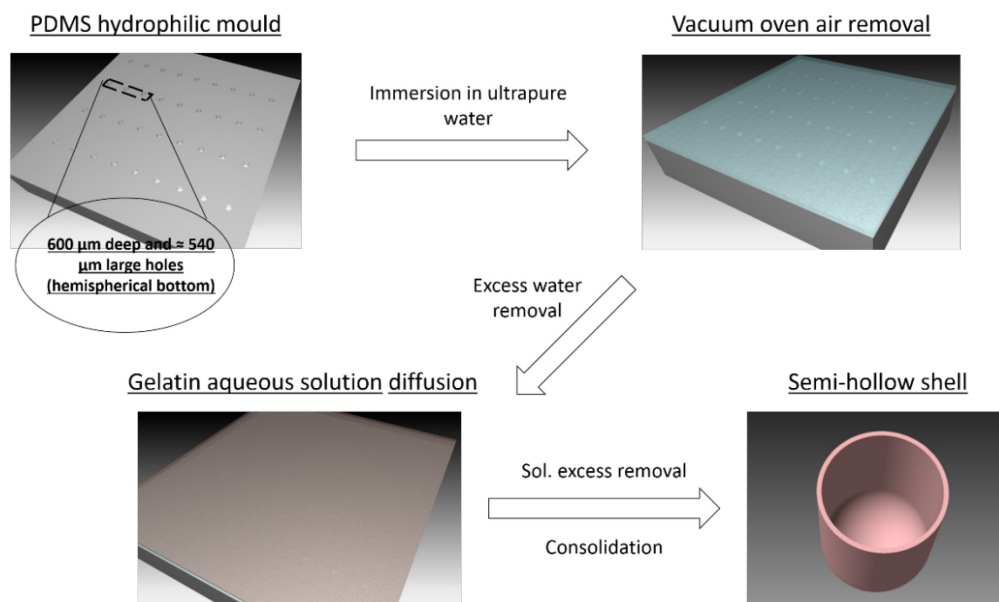


Figure 3.25: shells micromolding process workflow.

Briefly, a 10% w/v gelatin (G9391, Sigma-Aldrich, USA) solution was prepared, heated at 50°C and subsequently stirred at moderate speed to promote solute homogenization. Finally, glyceraldehyde (G5001, Sigma-Aldrich, USA) (5% w/w compared to gelatin initial powder) was added and the solution stirred at 50°C overnight.

The next day, PDMS hydrophilic moulds were submerged in a room temperature water bath; vacuum extraction and sonication were performed to remove trapped air bubbles. Then, excess water was removed and quickly replaced by 600 µL of 10% w/v gelatin solution at 50°C. The mold was then incubated at 50°C for 30 minutes to promote gelatin diffusion. Finally, excess solution was bladed away and the system consolidated at 70°C in an oven for at least 45 minutes. The mold was then visually inspected using the stereomicroscope and stored at room temperature.

3.7.4. External shells characterization

SEM observations were performed as previously described to evaluate shells micromolding quality. Briefly, several shells were carefully removed from PDMS moulds under a stereomicroscope, visually inspected and conveniently mounted on stubs to observe their lateral and bottom surface. A layer of gold (45 nm) was deposited on samples which were then loaded into the SEM. Photographs were shot at 10 kV and different magnifications.

Figure 3.26 shows pictures of the lateral and the bottom surfaces of shells. These strongly resemble the designed structures. Moreover, it can be observed that both the lateral and bottom surfaces do not present major replica defects demonstrating the gelatin solution has effectively diffused during the 50°C incubation step. SEM pictures finally allow to qualitatively ascertain the

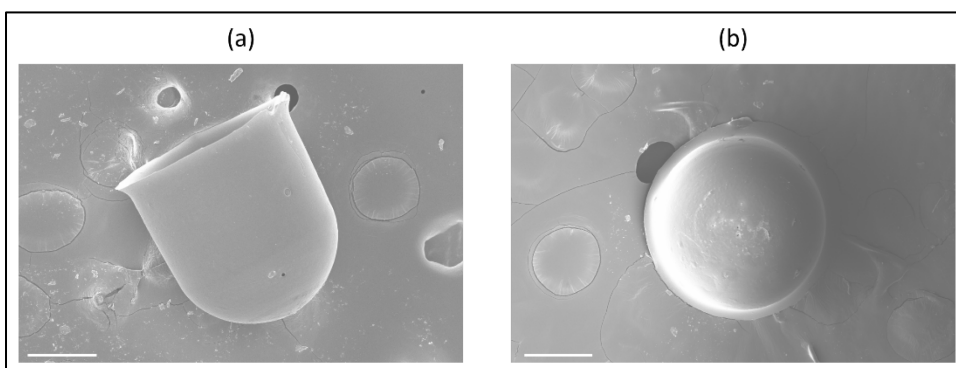


Figure 3.26: gelatin shells SEM photographs emphasising (a) lateral or (b) bottom surface. Scale bars: 200 μm .

designed dimensions have been respected; indeed, the fabricated PDMS molds after REM steps present holes whose diameters have a $538.72 \pm 1.12 \mu\text{m}$ mean value. The microfabricated shells using these moulds have usually demonstrated an adequate integration in middle layers pore as it will be further ascertained.

Tao and co-workers yet presented a procedure to fabricate hollow asymmetric gelatin structures through a combination of photolithographic and SL methods¹⁸⁶. Anyway, the manufactured gelatin structures were smaller in height of an order of magnitude ($\approx 10 \mu\text{m}$) to the truncated round-shaped shells shown in Figure 3.26.

Instead, Kim and co-workers developed an equivalent fabrication procedure to that described in the last paragraph fabricating microcontainers with thicknesses up to 250 μm . Briefly, photolithography and REM methods were used to fabricate PDMS stencils of different shapes. Stencils were subsequently fixed on a glass slide and the whole system was plasma cleaned. Polymeric

solutions of different concentrations were prepared and some droplets dispensed onto PDMS stencils. Finally, the excess solution was bladed and the residual liquid was cured at room temperature. For instance, circular containers of 300 μm diameter were successfully fabricated using synthetic polymer solutions¹⁴⁴. The data obtained show thus the straightforward possibility to fabricate different shells using similar solution-based processes. Synthetic and natural polymers can be equivalently processed conveniently tuning several manufacturing steps.

3.7.5. Drug delivery systems: microparticles packing and sintering

The second step for the effective fabrication of DDSs was μPs packing in empty shells. An aliquot of VEGF loaded μPs was thawed and several μPs were spreaded on the hydrophilic PDMS. The flat part of a small spatula was used to move μPs inside hollow shells to fill these completely. Subsequently, a PDMS counterstamp was used to properly pack μPs previously moved inside shells. PDMS counterstamp was designed with pillars placed in the same positions of PDMS mold holes. Specifically, μ -milling was used to pattern (TR-2-0120-S) flat 300 μm wide and 300 μm deep holes in a PMMA sheet (4 mm thickness). TR-2-0800-S mill was used to cut the predesigned perimeter of the PMMA mold. The PDMS counterstamp was later effectively fabricated by REM (PDMS 10:1, 80°C, 90 minutes).

The described packing procedure was further performed twice again to completely fill gelatin shells. At the third passage, packing by PDMS counterstamp was avoided.

The third step of DDSs preparation was packed μPs sintering, which was performed using solvent vapours or gaseous CO_2 .

The first process was described by De Alteriis and co-workers¹⁸⁷ and adopted with some modifications. Briefly, a custom-made vaporization setup was used to vaporize a dimethyl carbonate (517127, Sigma-Aldrich, USA)/ethanol solution (1:8 ratio V/V). Setup was composed by a jacketed Drechsel bottle connected to a thermostatic bath and to a nitrogen line. The temperature of the thermostatic bath was set to 25 °C while the nitrogen pressure was set to 0.15 bar. The ends of a flexible tube were connected to the gas outlet of the Drechsel bottle and to a 40 mm glass funnel, respectively, so that this could properly enclose the PDMS mold. Once the solvent mixture was dispensed into the Drechsel bottle and the PDMS mold was properly enclosed, nitrogen flux was opened and VEGF loaded μPs were exposed to solvent vapours for 8 minutes. Then, the PDMS mould was placed under an extraction arm for at least 30 minutes to extract the residual solvent vapour.

Gaseous CO₂ μ Ps exposition was performed inside a critical point dryer (EM CPD 300, Leica, Austria). The PDMS mold top surface was covered with filter paper and placed inside the fine mesh specimen holder tool. The upper part of this holder was blocked with a small brass piece to lock the PDMS mold in position during the experiment. The whole system was then loaded inside the machine's chamber and temperature was set to 15°C. Then, gaseous CO₂ was slowly injected inside the chamber and a fast exchange phase was performed setting the pressure around 30 bar (far from CO₂ critical pressure). Then, temperature was raised to approximately 32°C and a 10 minutes plasticization step was performed at \approx 35 bar. Later, CO₂ was slowly ejected and the chamber cooled to 25°C. Finally, PDMS mold was placed under an extraction arm for at least 30 minutes to extract the residual gaseous CO₂.

3.7.6. Microparticles packing and sintering characterization

VEGF sintered μ Ps superficial morphology was analysed by SEM.

Briefly, sintered μ Ps samples were packed inside PDMS moulds without shells and sintered using one of the two described methods. Later, samples were carefully removed from PDMS moulds under a stereomicroscope, visually inspected and conveniently mounted on stubs. A layer of gold (45 nm) was deposited on samples which were then loaded into the SEM. Photographs were shot at 10 and 15 kV and different magnifications.

Figure 3.27 (a) shows low magnification image of sintered μ Ps after CO₂ sintering and figure 3.27 (b) presents a higher magnification image of a smaller area.

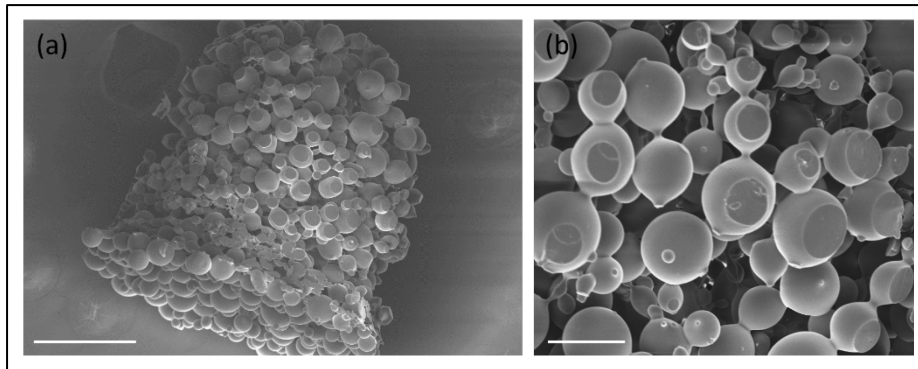


Figure 3.27: SEM photographs of sintered μ Ps. (a) Lateral view of a sintered sample. Scale bar: 200 μ m (b) High magnification picture of a sample aimed to highlight the sintering necks. Scale bar: 60 μ m.

Albeit the difference in μ Ps dimensions, the developed procedure allows an adequate packing of μ Ps, as the overall shape of the systems shows. The multiple sintering necks between particles – see figure 3.27 (b) – indicate the sintering condition promote the effective fabrication of a sintered sample. Similar morphological structures can be observed for sintered μ Ps samples using

dimethyl carbonate /ethanol solvent vapours. De Alteriis and co-workers have indeed previously demonstrated the successful processing in PDMS molds of VEGF loaded PLGA μ Ps using the apparatus. However, these were relatively bigger in dimension (few hundreds of microns) and the apparatus was used for a different aim. Indeed, work purpose was that of tuning the shape of single particles which were respectively loaded in different PDMS molds patterned with holes of different shapes to fabricate non spherical μ Ps. Otherwise, the actual target was the possibility of sinter different smaller spherical μ Ps. Therefore, several experiments were carried out to determine the minimum time to achieve a minimum sintering condition between μ Ps to carry out further operations (DDSs sealing). The minimum adequate sintering time resulted to be 8 minutes.

Figure 3.28 presents sintered μ Ps internal structures after sintering.

These pictures were obtained as described for non-sintered μ Ps, including sintered samples in PDMS. SEM photographs suggests sintering has not altered μ Ps structures, indeed, figure 3.28 (b-c) shows μ Ps internal microstructures similar to that showed in figure 3.24.

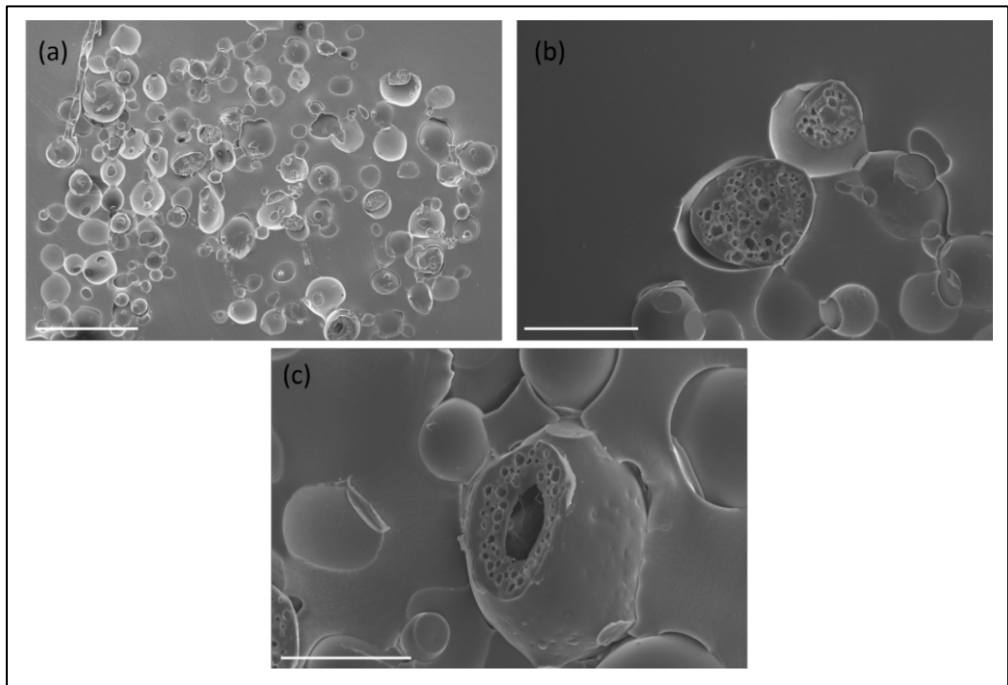


Figure 3.28: SEM photographs of cut sintered μ Ps. (a) Low magnification photograph of a cut sintered sample. Scale bar: 150 μ m (b) High magnification picture aimed to highlight μ Ps internal morphology. Scale bar: 50 μ m; (c) High magnification picture of an included μ Ps with a big central internal macropore. Scale bar: 50 μ m.

It is well-known that extended exposure to solvents can alter the biological activity of encapsulated proteins and bioactive factors⁷³. Among alternative sintering procedures, CO₂ has been one of the most chosen sintering agents. Several experiments have demonstrated the effective sintering of PLGA μ Ps using different CO₂ conditions¹⁸⁸. Moreover, multiple are the applications in TE of such scaffolds: Detamore's group has indeed carried out several studies which have demonstrated successful application of μ Ps for the fabrication of scaffolds for bone and cartilage tissue regeneration purposes^{189,190}. Later, the author's attention focused even also on the fabrication of bioactive sintered scaffolds. For instance, release characteristics of BMP-2 or transforming growth factor - β 3 from PLGA μ Ps subjected to a CO₂ sintering treatment (15 bar, 60 minutes) were investigated demonstrating for both proteins a sustained release from scaffolds up to 3 weeks. Previous studies, such as that of Ennett and co-workers, have even demonstrated the successful sintering of VEGF loaded μ Ps (5 - 50 μ m diameter) to fabricate bioactive scaffolds which have effectively enhanced local angiogenesis after subcutaneous implantation in mice¹⁹¹. The promising findings have provided the inspiration for developing a similar procedure to process and sinter the VEGF loaded μ Ps previously analysed. Similarly to solvent based sintering, several experiments were carried out to determine the minimum sintering conditions. A pressure of 35 bar and a temperature of 32°C for 10 minutes were used for fabricating structures such that showed in Figure 3.27 (a) and (b) which could be sealed inside gelatin shells.

3.7.7. Drug delivery systems: sealing

The yet available 10% w/V gelatin aqueous solution was heated on a hot plate over the sol-gel transition temperature (45°).

DDSs sealing was performed under a stereomicroscope using an adjustable volume pipettes. A small amount of solution was aspirated and a small solution meniscus was quickly created onto the tip adjusting the pipette volume. This small liquid amount was deposited on the top of a DDSs. The operation was repeated to seal all the fabricated DDSs shells replacing tips and liquids when needed. Finally, the PDMS mold was left under an extraction arm overnight to properly dry the deposited gelatin.

3.7.8. Drug delivery systems: characterization

Composite DDSs morphology was evaluated by SEM. Briefly, samples were carefully removed from PDMS moulds under a stereomicroscope, visually inspected and conveniently deposited on stubs' carbon tape. A layer of gold (45 nm) was sputtered on samples which were then loaded into the SEM. Photographs were shot at 7.5 and 10 kV and different magnifications.

Figure 3.29 shows a typical composite DDS.

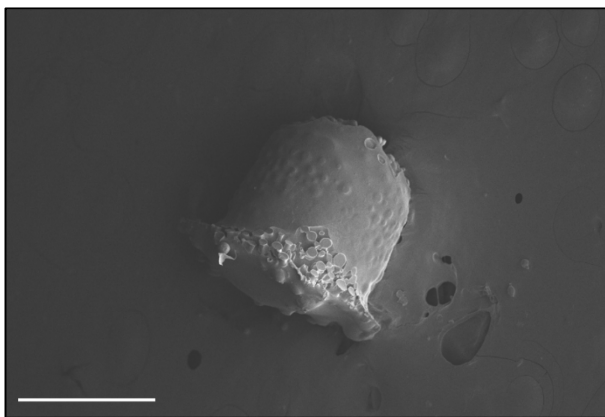


Figure 3.29: SEM photograph of the lateral view of a sealed DDS. Scale bar: 400 μm .

This picture suggests the sealing process has not generally altered the external shape of the premanufactured shells. However, SEM observations show the appearance of little bumps on the external surfaces of DDSs. This effect could be reasonably ascribed to the packing process. Indeed, the consecutive processes of μPs deposition and packing (especially the latter one) could induce a moderate pressure on the rigid external shell layer which could result unavoidably modified once that the μPs structure is sintered.

The same figure 3.29 demonstrate the effectively capping of DDSs. The manual method developed is an effective and straightforward way to seal premanufactured shells or microcontainers. The advantages of this process were demonstrated also by Kim and co-workers for the fabrication of synthetic polymers microcontainers filled by alginate solutions¹⁴⁴. Anyway, an important drawback of such technique is the use of organic solvents such as DCM or chloroform which represent a possible drawback for the manufacturing of composite DDSs.

However, the developed manual method could not always guarantee a strict control of solution deposition. This can generate system sealed with an excess solution volume which can generate large diameter caps. Recently, to overcome this difficulty, studies on microsized DDSs has become very popular and many researchers have proposed various methods for DDSs systems capping using even automated approaches, which can better help to control liquid deposition. Nemeth and co-workers proposed for instance the entire fabrication of DDSs using a dropwise, layer-by-layer process to fabricate Eudragit based DDSs using insulin as a model drug. A sciFLEXARRAYER S3 printer allowed the precise deposition on premanufactured insulin loaded shells of ≈ 300 pL Eudragit solution. SEM images of DDSs after desiccation suggest an effectively accurate capping procedure¹⁹².

3.7.9 Gelatin films swelling experiments

Methods

Gelatin films were prepared and swelling experiments were used to investigate the swelling properties of the materials used for DDSs shells micromolding.

Briefly, a gelatin glycerinaldehyde aqueous solution (10% w/V – 5% w/w) was prepared as previously described. The next day, gelatin films were prepared dispensing 1 mL of hot solution inside PTFE frames (18 mm side) fixed by binder clips (1 cm width) on cut PTFE sheets (\approx 30 mm side). The system was dried in an oven (70°C) for at least 3h.

Later, the systems were disassembled and the films iteratively parted up to fragments each of a few mg weight. Three similar samples were weighed on an analytical balance and then immersed in small petri dishes containing few mL water (preheated at 37°C in an oven). At the different time points, each sample was removed, blotted dry using filter paper, and weighed on the same analytical balance. Swelling data were evaluated as the ratio of the weight of the swollen sample on the initial dry weight. After three days, the prepared gelatin fragments were removed from the petri dishes and dried again at 70°C for at least 1 h. Finally, fragment mass was measured to evaluate samples weight loss.

Results and discussion

Table 3.8 shows a chart which summarizes the swelling experiments results.

	15 minutes	48 h	72 h
Swelling ratio	7.93 ± 0.52	8.51 ± 0.94	9.12 ± 0.83

Table 3.8: swelling ratio evolution over time of gelatin/glycerinaldehyde fragments (n=3). α set for the statistical analysis is 0.05.

The data show fragments mass increase over three days \approx 9 times their dry weight. These data are broadly consistent with those experimentally measured by Kosmala and co-workers for 1% glycerinaldehyde cross-linked gelatin/dextran films. They indeed have demonstrated that these films reach a 6.5 volume swelling ratio in two days and are subsequently stable for 5 weeks before losing integrity¹⁵¹. These last findings support moreover the statistical analysis which reports data of table 3.8 are not significantly different.

Dry mass evaluation after 72h report a \approx 40% mass loss. Thus, these data suggest that, albeit stable in physiological conditions, fluid can effectively erode the cross-linked material. Consequently, it could be reasonable suppose cross-linked gelatin in form of shells allows a fast fluid penetration which can induce loaded drug diffusion from sintered μ Ps. Moreover, shells swelling could ideally

prevent DDSs displacements penalizing possible movements from the predesigned positions.

As experimentally evaluated and broadly demonstrated, gelatin rapidly dissolves in physiological conditions (≈ 10 minutes after immersion in water at 37°C for our experiment) and cannot be used without a previous cross-linking step.

In conclusion, the results obtained suggest the gelatin/glyceraldehyde microfabricated shells are adequately stable in physiological conditions and represent a potential candidate material for future *in vivo* studies of bioactivated composite scaffolds.

3.7.10 Fabrication of composite multifunctional scaffolds

PCL layers and gelatin DDSs were integrated to assemble a 3D composite scaffold. Specifically, sealed DDSs were carefully peeled from PDMS moulds under a stereomicroscope. Later, these were manually integrated in PCL layers using tweezers under a stereomicroscope according to predesigned configurations, as for instance the potential ones illustrated in the renders (generated using Rhinoceros) of Figure 3.30.

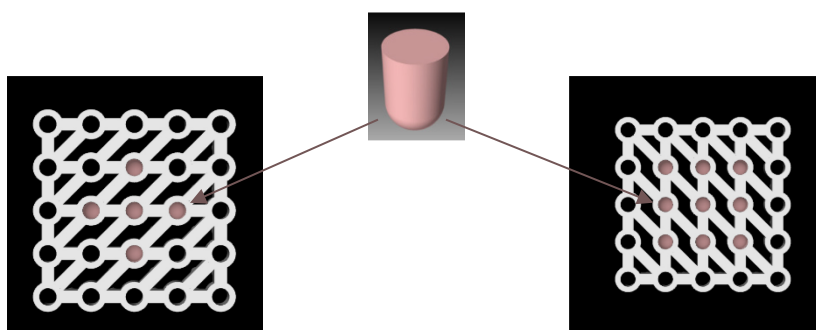


Figure 3.30: Simplified graphical representation for microcontainers integration in PCL layers circular pores.

Later, composite layers were assembled as previously described for the bare PCL layers. Scaffolds integration was finally evaluated using μ -CT as previously described.

3.7.11 Characterization of composite multifunctional scaffolds

Figure 3.31 shows two pictures of the tomographic model of a $0/90^{\circ}$ composite scaffold whose middle layers were integrated according to the configuration shown in the right side of Figure 3.30.

DDSs were loaded in the central pores of each of the three middle layers. Figure 3.31 (a) presents a low magnification picture of a virtual section of such a designed scaffold, specifically showing one of the composite layers.

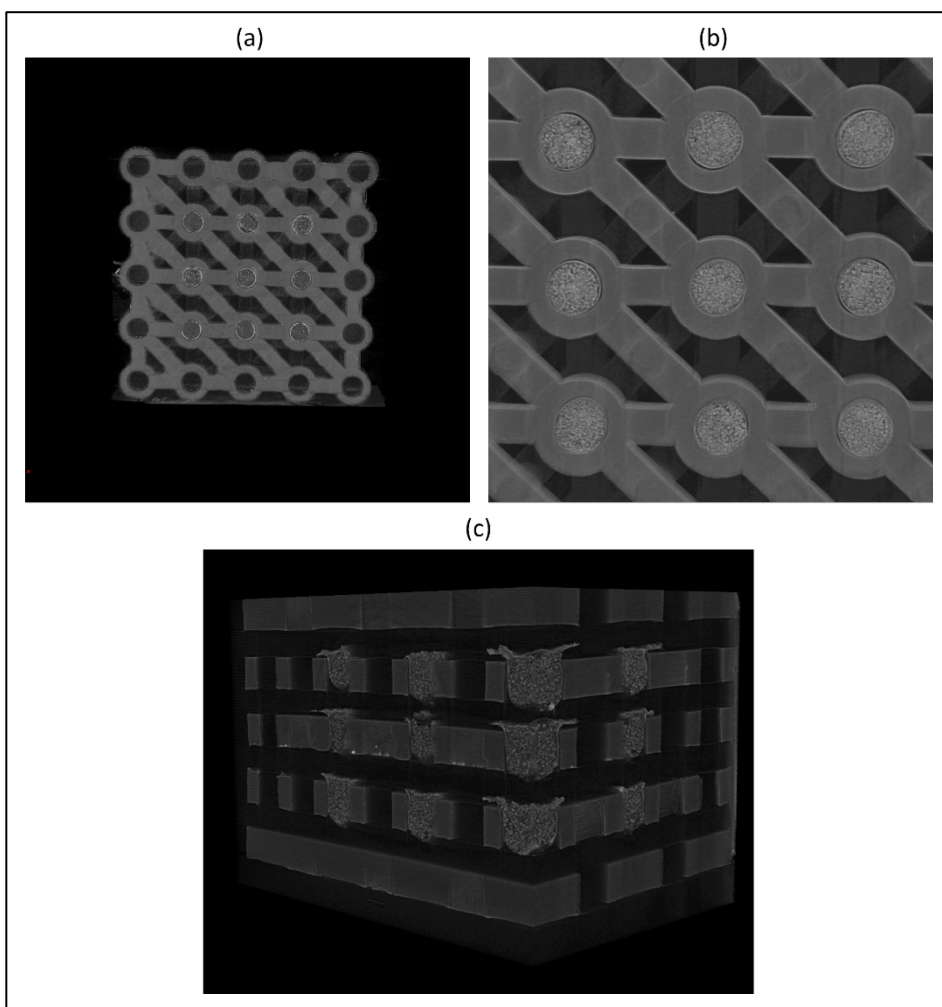


Figure 3.31: μ -CT tomographic model of a composite 0/90° scaffold. (a) Virtual section of a scaffold middle layer. (b) Magnification of the layer centre to highlight DDSs integration. (c) Lateral virtual section of the scaffold centre aimed to show the integration of DDSs in middle layers.

There is a good match between this structure and the 0/90° structures previously developed. This demonstrates the same assembly process could be used and thus the presence of DDSs does not force to make changes to the stacking protocol. Figure 3.31 (b) illustrates the picture of the same layer with a higher magnification. The image proves once again the packing quality of μ Ps inside gelatin shells and allows to observe with greater clarity the integration between the two modules. The results show that major sintering errors are absent and PCL layers pores do not seem deformed after DDSs integration.

Figure 3.31 (c) further supports the presented findings presenting a lateral picture of the 3D tomographic model showing 12 DDSs positioned inside the middle layers.

An important question is related to possible applications for such a configuration. The finding supported by Quade and co-workers suggest the presented scaffolds could have great potential for *in situ* tissue engineering approaches. Fibrillated mineralized collagen was used to produce porous scaffolds into which several ng of VEGF were loaded in scaffold centre to evaluate GF release and study endothelial cells migration. The results show scaffolds modified with a heparin containing VEGF central depots still release biologically active GF after 28 days of cultivation and are capable to recruit endogenous cells developing the steepest VEGF gradient among all the scaffolds types analysed¹⁹³. It could be therefore expected that similar or more promising findings could be shown also by the presented 3D composite scaffolds with controlled structural and morphological properties that have been extensively analysed in this dissertation.

Chapter 4: conclusions and future perspectives

In this study, a bottom-up approach aimed to the fabrication of modular scaffolds for TE applications was introduced.

A preliminary *in silico* study was carried out as first stage to evaluate a potential versatile scaffold design but even possible fabrication technologies to use and eligible materials to process. This study has suggested the fabrication of different PCL layers types to be assembled according to two configurations (0° and $0^\circ/90^\circ$). Scaffolds layers could be eventually integrated with DDSs loaded in predesigned positions to later assembly composite scaffolds.

Based on the results, it can be concluded an innovative (to the author's best knowledge) magnetic embossing process allows to fabricate high thickness PCL layers, whose morphology and pore structure strongly resembles the CAD models. μ -CT tomographic models demonstrate moreover PCL layers presents only minor filling defects. Layers superficial topography presents a sub-micron roughness (30 - 40 nm) and superficial chemistry analyses prove the absence of PVA residues after H₂O treatments (as also supported by SEM images). These findings suggest that magnetic embossing has great potential for manufacturing modules of different thermoplastic polymeric materials; for instance, the PLGA/nanoclays composite layers, fabricated using the "Sacrificial Layer Embossing" process¹³⁵ and used as modules for assembling scaffolds aimed at stem cells differentiation studies¹³⁷, might be potentially fabricated achieving higher thicknesses (hundreds of microns) and promoting a decrease in layers dimensional features mismatches. It is expected finally different microstructures could be fabricated using magnetic embossing opportunely tuning the thickness of the material film to process and the embossing parameters.

The layers assembly technique allows PCL modules bonding; moreover, the process does not induce alterations of modules microstructures as demonstrated by SEM photographs and μ -CT showing structures which strongly resemble the CAD models. The different porosity analyses support the designed porosity value ($\approx 57\%$), while mechanical characterizations demonstrate scaffold compression behaviour strictly resembles that of a porous material (as expected). Mechanical behaviour findings suggest moreover potential applications of such scaffolds - Young's modulus (MPa) presented values are ≈ 27 and 29 MPa - in the bone TE field. *In vitro* tests supported the developed modular approach can be used to fabricate biocompatible scaffolds and demonstrated a successful HUVECs adhesion on different layers and cells proliferation over time.

It has been presented also a multistep technique to produce modular DDSs. Gelatin shells were straightforwardly fabricated using a micromolding procedure as confirmed by SEM photographs. Two techniques were used to successfully sinter μ Ps loaded in shells and the same solution could be used to seal the VEGF loaded DDSs. SEM photographs illustrate the effective μ Ps (42 μ m mean diameter) sintering (high magnification photographs) without the alteration of the original internal morphology. This μ Ps system has been successfully enclosed in cross-linked gelatin shells whose shape was not modified during the different manufacturing steps. The findings suggest that this approach could be applicable to manufacture modular DDSs using different shells material/shapes and which can potentially encapsulate active drugs/molecules after the exposure to solvent vapours/ CO_2 .

DDSs were effectively integrated in predesigned layers position, as demonstrated by μ -CT tomographic models. Both modules features seem not present deformations even after both manual handling and integration. Finally, it is possible to assert the illustrated example of a composite scaffold have great potential for applications such as vascular bone TE, as initially even indicated by the supporting literature.

Anyway, further research is still required. Specifically, more tests will be needed to verify VEGF encapsulation efficiency in μ Ps; simultaneously, further experiments will be required to find out VEGF release profile. These analyses will be needed even to effectively evaluate DDSs biological activity following the sintering procedures.

Moreover, further research on potential systems of automated integration is desirable to prove the possibility to automatically integrate bioactive DDSs inside PCL layers. These analyses appear fully justified to develop an improved bottom-up approach which can potentially enhance integration resolution between modules and increase scaffolds fabrication yield.

In conclusion, more research into possible bioactive scaffold designs is still necessary to validate the discussed modular approach could effectively be used to manufacture scaffolds potentially capable to control the space and time presentation of bioactive cues (e.g. VEGF) and consequently govern and guide morphogenic and tissueogenic processes.

References

- 1 Watson, C. J. E. & Dark, J. H. Organ transplantation: historical perspective and current practice. *Br. J. Anaesth.* **108**, 129-142, doi:10.1093/bja/aer384 (2012).
- 2 Tevis, S. E. & Kennedy, G. D. Postoperative complications and implications on patient-centered outcomes. *J. Surg. Res.* **181**, 106-113, doi:10.1016/j.jss.2013.01.032 (2013).
- 3 Dzobo, K. *et al.* Advances in Regenerative Medicine and Tissue Engineering: Innovation and Transformation of Medicine. *Stem Cells Int.*, **24**, doi:10.1155/2018/2495848 (2018).
- 4 Heath, D. *30 years of tissue engineering, what has been achieved?*, <<https://www.weforum.org/agenda/2019/06/30-years-since-the-mouse-with-a-human-ear-what-has-been-achieved/>> (2019).
- 5 Langer, R. & Vacanti, J. P. Tissue Engineering. *Science* **260**, 920-926, doi:10.1126/science.8493529 (1993).
- 6 Ikada, Y. Challenges in tissue engineering. *J. R. Soc. Interface* **3**, 589-601, doi:10.1098/rsif.2006.0124 (2006).
- 7 Korias, P. Delivery of Growth Factors for Tissue Regeneration and Wound Healing. *Biodrugs* **26**, 163-175, doi:10.2165/11631850-000000000-00000 (2012).
- 8 Sultana, N. in *Biodegradable Polymer-Based Scaffolds for Bone Tissue Engineering* 1-17 (Springer Berlin Heidelberg, 2013).
- 9 Li, S., Sengupta, D. & Chien, S. Vascular tissue engineering: from in vitro to in situ. *Wiley Interdiscip. Rev.-Syst. Biol* **6**, 61-76, doi:10.1002/wsbm.1246 (2014).
- 10 Rhiyahinezhad, H., Sabbatier, G. & McKiel L. *In vitro, in vivo, and in situ tissue engineering: pros and cons*, <<https://biomaterialskingston.wordpress.com/2017/04/26/sc7-in-vitro-in-vivo-and-in-situ-tissue-engineering-pros-and-cons/>> (2017).
- 11 Lee, S. J., Yoo, J. J. & Atala, A. in *In Situ Tissue Regeneration* (eds Sang Jin Lee, James J. Yoo, & Anthony Atala) 3-17 (Academic Press, 2016).
- 12 Chan, B. P. & Leong, K. W. Scaffolding in tissue engineering: general approaches and tissue-specific considerations. *Eur. Spine J.* **17**, S467-S479, doi:10.1007/s00586-008-0745-3 (2008).
- 13 Rana, D., Arulkumar, S., Vishwakarma, A. & Ramalingam, M. in *Stem Cell Biology and Tissue Engineering in Dental Sciences* (eds Ajaykumar Vishwakarma, Paul Sharpe, Songtao Shi, & Murugan Ramalingam) 133-148 (Academic Press, 2015).
- 14 Guarino, V., Causa, F. & Ambrosio, L. Bioactive scaffolds for bone and ligament tissue. *Expert Rev. Med. Devices* **4**, 405-418, doi:10.1586/17434440.4.3.405 (2007).
- 15 Babaie, E. & Bhaduri, S. B. Fabrication Aspects of Porous Biomaterials in Orthopedic Applications: A Review. *ACS Biomater. Sci. Eng.* **4**, 1-39, doi:10.1021/acsbomaterials.7b00615 (2018).

- 16 Ratner, B. D. The Biocompatibility Manifesto: Biocompatibility for the Twenty-first Century. *J. Cardiovasc. Transl. Res.* **4**, 523-527, doi:10.1007/s12265-011-9287-x (2011).
- 17 Rodriguez, B. L. & Larkin, L. M. in *Functional 3D Tissue Engineering Scaffolds* (eds Ying Deng & Jordan Kuiper) 279-304 (Woodhead Publishing, 2018).
- 18 Zhu, M. F. *et al.* In vivo engineered extracellular matrix scaffolds with instructive niches for oriented tissue regeneration. *Nat. Commun.* **10**, 14, doi:10.1038/s41467-019-12545-3 (2019).
- 19 Ghouse, S. *et al.* The design and in vivo testing of a locally stiffness-matched porous scaffold. *Appl. Mater. Today* **15**, 377-388, doi:10.1016/j.apmt.2019.02.017 (2019).
- 20 Cortese, B. & Elwany, M. Occurrence and management of bioresorbable vascular scaffold failure in real-life studies. *J. Thorac. Dis.* **9**, S935-S939, doi:10.21037/jtd.2017.06.82 (2017).
- 21 Tan, H. C. & Ananthakrishna, R. A review of bioresorbable scaffolds: hype or hope? *Singap. Med. J.* **58**, 512-515, doi:10.11622/smedj.2016178 (2017).
- 22 Zhang, H. B., Zhou, L. & Zhang, W. J. Control of Scaffold Degradation in Tissue Engineering: A Review. *Tissue Eng. Part B-Rev.* **20**, 492-502, doi:10.1089/ten.teb.2013.0452 (2014).
- 23 Gomes, M. E., Malafaya, P. B. & Reis, R. L. in *Biodegradable Systems in Tissue Engineering and Regenerative Medicine* (eds R.L. Reis & Julio San Román) Ch. 5, (CRC Press, 2004).
- 24 Prabakaran, M. in *Characterisation and Design of Tissue Scaffolds* (ed Paul Tomlins) 149-168 (Woodhead Publishing, 2016).
- 25 Salerno, A. & Netti, P. A. in *Biomedical Foams for Tissue Engineering Applications* (ed Paolo A. Netti) 71-100 (Woodhead Publishing, 2014).
- 26 Sgarminato, V., Tonda-Turo, C. & Ciardelli, G. Reviewing recently developed technologies to direct cell activity through the control of pore size: From the macro- to the nanoscale. *J. Biomed. Mater. Res. Part B*, **10**, doi:10.1002/jbm.b.34467 (2019).
- 27 Greiner, J. F. W. *et al.* Natural and synthetic nanopores directing osteogenic differentiation of human stem cells. *Nanomed.-Nanotechnol. Biol. Med.* **17**, 319-328, doi:10.1016/j.nano.2019.01.018 (2019).
- 28 Brennan, C. M., Eichholz, K. F. & Hoey, D. A. The effect of pore size within fibrous scaffolds fabricated using melt electrowriting on human bone marrow stem cell osteogenesis. *Biomed. Mater.* **14**, 12, doi:10.1088/1748-605X/ab49f2 (2019).
- 29 Wang, H. *et al.* The effect of 3D-printed Ti6Al4V scaffolds with various macropore structures on osteointegration and osteogenesis: A biomechanical evaluation. *J. Mech. Behav. Biomed. Mater.* **88**, 488-496, doi:10.1016/j.jmbbm.2018.08.049 (2018).
- 30 Mei, C. *et al.* Three-dimensional spherical gelatin bubble-based scaffold improves the myotube formation of H9c2 myoblasts. *Biotechnol. Bioeng.* **116**, 1190-1200, doi:10.1002/bit.26917 (2019).

- 31 Wang, W. S. *et al.* Implantable and Biodegradable Macroporous Iron Oxide Frameworks for Efficient Regeneration and Repair of Infracted Heart. *Theranostics* **7**, 1966-1975, doi:10.7150/thno.16866 (2017).
- 32 Chitrangi, S., Nair, P. & Khanna, A. Three-dimensional polymer scaffolds for enhanced differentiation of human mesenchymal stem cells to hepatocyte-like cells: a comparative study. *J. Tissue Eng. Regen. Med.* **11**, 2359-2372, doi:10.1002/term.2136 (2017).
- 33 Li, J. *et al.* 3D PLGA Scaffolds Improve Differentiation and Function of Bone Marrow Mesenchymal Stem Cell-Derived Hepatocytes. *Stem Cells Dev.* **19**, 1427-1436, doi:10.1089/scd.2009.0415 (2010).
- 34 Loh, Q. L. & Choong, C. Three-Dimensional Scaffolds for Tissue Engineering Applications: Role of Porosity and Pore Size. *Tissue Eng. Part B-Rev.* **19**, 485-502, doi:10.1089/ten.teb.2012.0437 (2013).
- 35 Yeong, W. Y. *et al.* Porous polycaprolactone scaffold for cardiac tissue engineering fabricated by selective laser sintering. *Acta Biomater.* **6**, 2028-2034, doi:10.1016/j.actbio.2009.12.033 (2010).
- 36 Dattola, E. *et al.* Development of 3D PVA scaffolds for cardiac tissue engineering and cell screening applications. *RSC Adv.* **9**, 4246-4257, doi:10.1039/c8ra08187e (2019).
- 37 Prasopthum, A., Cooper, M., Shakesheff, K. M. & Yang, J. Three-Dimensional Printed Scaffolds with Controlled Micro-/Nanoporous Surface Topography Direct Chondrogenic and Osteogenic Differentiation of Mesenchymal Stem Cells. *ACS Appl. Mater. Interfaces* **11**, 18896-18906, doi:10.1021/acsami.9b01472 (2019).
- 38 Choi, S. W., Zhang, Y., MacEwan, M. R. & Xia, Y. N. Neovascularization in Biodegradable Inverse Opal Scaffolds with Uniform and Precisely Controlled Pore Sizes. *Adv. Healthc. Mater.* **2**, 145-154, doi:10.1002/adhm.201200106 (2013).
- 39 Bai, F. *et al.* The Correlation Between the Internal Structure and Vascularization of Controllable Porous Bioceramic Materials In Vivo: A Quantitative Study. *Tissue Eng. Part A* **16**, 3791-3803, doi:10.1089/ten.tea.2010.0148 (2010).
- 40 Somo, S. I. *et al.* Pore Interconnectivity Influences Growth Factor-Mediated Vascularization in Sphere-Templated Hydrogels. *Tissue Eng. Part C-Methods* **21**, 773-785, doi:10.1089/ten.tec.2014.0454 (2015).
- 41 Liao, E., Yaszemski, M., Krebsbach, P. & Hollister, S. Tissue-engineered cartilage constructs using composite hyaluronic acid/collagen I hydrogels and designed poly(propylene fumarate) scaffolds. *Tissue Eng.* **13**, 537-550, doi:10.1089/ten.2006.0117 (2007).
- 42 Kempainen, J. M. & Hollister, S. J. Differential effects of designed scaffold permeability on chondrogenesis by chondrocytes and bone marrow stromal cells. *Biomaterials* **31**, 279-287, doi:10.1016/j.biomaterials.2009.09.041 (2010).
- 43 Jeong, C. G. & Hollister, S. J. Mechanical and Biochemical Assessments of Three-Dimensional Poly(1,8-Octanediol-co-Citrate) Scaffold Pore Shape and

- Permeability Effects on In Vitro Chondrogenesis Using Primary Chondrocytes. *Tissue Eng. Part A* **16**, 3759-3768, doi:10.1089/ten.tea.2010.0103 (2010).
- 44 Almeida, H. A. & Bártolo, P. J. in *Computer-Aided Tissue Engineering* (ed Michael A. K. Liebschner) 209-236 (Humana Press, 2012).
- 45 Kang, H., Lin, C. Y. & Hollister, S. J. Topology optimization of three dimensional tissue engineering scaffold architectures for prescribed bulk modulus and diffusivity. *Struct. Multidiscip. Optim.* **42**, 633-644, doi:10.1007/s00158-010-0508-8 (2010).
- 46 Wang, Y., Luo, Z., Zhang, N. & Qin, Q. H. Topological shape optimization of multifunctional tissue engineering scaffolds with level set method. *Struct. Multidiscip. Optim.* **54**, 333-347, doi:10.1007/s00158-016-1409-2 (2016).
- 47 Netti, P. A. in *Regenerative Medicine Applications in Organ Transplantation* (eds Giuseppe Orlando, Jan Lerut, Shay Soker, & Robert J. Stratta) 137-150 (Academic Press, 2014).
- 48 U, M. T. in *Bioactive Materials in Medicine* (eds X. Zhao, J. M. Courtney, & H. Qian) 70-93 (Woodhead Publishing, 2011).
- 49 Elkasabgy, N. A. & Mahmoud, A. A. Fabrication Strategies of Scaffolds for Delivering Active Ingredients for Tissue Engineering. *AAPS PharmSciTech* **20**, 18, doi:10.1208/s12249-019-1470-4 (2019).
- 50 Laurencin, C. T., Ashe, K. M., Henry, N., Kan, H. M. & Lo, K. W. H. Delivery of small molecules for bone regenerative engineering: preclinical studies and potential clinical applications. *Drug Discov. Today* **19**, 794-800, doi:10.1016/j.drudis.2014.01.012 (2014).
- 51 Ungaro, F. *et al.* in *Topics in Tissue Engineering* Vol. 2 (ed N. Ashammakhi & R.L. Reis) Ch. 5, 1-39 (2005).
- 52 Biondi, M., Ungaro, F., Quaglia, F. & Netti, P. A. Controlled drug delivery in tissue engineering. *Adv. Drug Deliv. Rev.* **60**, 229-242, doi:10.1016/j.addr.2007.08.038 (2008).
- 53 Tabata, Y. Significance of release technology in tissue engineering. *Drug Discov. Today* **10**, 1639-1646, doi:10.1016/s1359-6446(05)03639-1 (2005).
- 54 Quaglia, F. Bioinspired tissue engineering: The great promise of protein delivery technologies. *Int. J. Pharm.* **364**, 281-297, doi:10.1016/j.ijpharm.2008.04.030 (2008).
- 55 Wang, Z. M. *et al.* Novel biomaterial strategies for controlled growth factor delivery for biomedical applications. *NPG Asia Mater.* **9**, 17, doi:10.1038/am.2017.171 (2017).
- 56 Garg, T., Singh, O., Arora, S. & Murthy, R. S. R. Scaffold: A Novel Carrier for Cell and Drug Delivery. *Crit. Rev. Ther. Drug Carr. Syst.* **29**, 1-63 (2012).
- 57 Richardson, T. P., Peters, M. C., Ennett, A. B. & Mooney, D. J. Polymeric system for dual growth factor delivery. *Nat. Biotechnol.* **19**, 1029-1034, doi:10.1038/nbt1101-1029 (2001).
- 58 Akar, B. *et al.* Biomaterials with persistent growth factor gradients in vivo accelerate vascularized tissue formation. *Biomaterials* **72**, 61-73, doi:10.1016/j.biomaterials.2015.08.049 (2015).

- 59 Hutmacher, D. W. Scaffolds in tissue engineering bone and cartilage. *Biomaterials* **21**, 2529-2543, doi:10.1016/s0142-9612(00)00121-6 (2000).
- 60 Mikos, A. G., Sarakinos, G., Leite, S. M., Vacant, J. P. & Langer, R. Laminated three-dimensional biodegradable foams for use in tissue engineering. *Biomaterials* **14**, 323-330, doi:[https://doi.org/10.1016/0142-9612\(93\)90049-8](https://doi.org/10.1016/0142-9612(93)90049-8) (1993).
- 61 Kim, J., Yaszemski, M. J. & Lu, L. C. Three-Dimensional Porous Biodegradable Polymeric Scaffolds Fabricated with Biodegradable Hydrogel Porogens. *Tissue Eng. Part C-Methods* **15**, 583-594, doi:10.1089/ten.tec.2008.0642 (2009).
- 62 Washburn, N. R. *et al.* Co-extrusion of biocompatible polymers for scaffolds with co-continuous morphology. *J. Biomed. Mater. Res.* **60**, 20-29, doi:10.1002/jbm.10049 (2002).
- 63 Guarino, V., Guaccio, A. & Ambrosio, L. Manipulating co-continuous polymer blends to create PCL scaffolds with fully interconnected and anisotropic pore architecture. *J. Appl. Biomater. Biomech.* **9**, 34-39, doi:10.5301/jabb.2011.6473 (2011).
- 64 Flynn, L., Dalton, P. D. & Shoichet, M. S. Fiber templating of poly(2-hydroxyethyl methacrylate) for neural tissue engineering. *Biomaterials* **24**, 4265-4272, doi:[https://doi.org/10.1016/S0142-9612\(03\)00334-X](https://doi.org/10.1016/S0142-9612(03)00334-X) (2003).
- 65 Stokols, S. *et al.* Templated agarose scaffolds support linear axonal regeneration. *Tissue Eng.* **12**, 2777-2787, doi:10.1089/ten.2006.12.2777 (2006).
- 66 Yang, S. F., Leong, K. F., Du, Z. H. & Chua, C. K. The design of scaffolds for use in tissue engineering. Part 1. Traditional factors. *Tissue Eng.* **7**, 679-689, doi:10.1089/107632701753337645 (2001).
- 67 Mathieu, L. M. *et al.* Architecture and properties of anisotropic polymer composite scaffolds for bone tissue engineering. *Biomaterials* **27**, 905-916, doi:<https://doi.org/10.1016/j.biomaterials.2005.07.015> (2006).
- 68 Eltom, A., Zhong, G. Y. & Muhammad, A. Scaffold Techniques and Designs in Tissue Engineering Functions and Purposes: A Review. *Adv. Mater. Sci. Eng.*, **13**, doi:10.1155/2019/3429527 (2019).
- 69 Nemati, S., Kim, S. J., Shin, Y. M. & Shin, H. Current progress in application of polymeric nanofibers to tissue engineering. *Nano Converg.* **6**, 16, doi:10.1186/s40580-019-0209-y (2019).
- 70 Elbert, D. L. Bottom-up tissue engineering. *Curr. Opin. Biotechnol.* **22**, 674-680, doi:10.1016/j.copbio.2011.04.001 (2011).
- 71 Mikos, A. G. *et al.* PREPARATION OF POLY(GLYCOLIC ACID) BONDED FIBER STRUCTURES FOR CELL ATTACHMENT AND TRANSPLANTATION. *J. Biomed. Mater. Res.* **27**, 183-189, doi:10.1002/jbm.820270207 (1993).
- 72 Laurencin, C. T., Ko, F. K., Attawia, M. A. & Borden, M. D. Studies on the development of a tissue engineered matrix for bone regeneration. *Cells and Materials* **8**, 175-181 (1998).

- 73 Gupta, V., Khan, Y., Berkland, C. J., Laurencin, C. T. & Detamore, M. S. in *Annual Review of Biomedical Engineering, Vol 19* Vol. 19 *Annual Review of Biomedical Engineering* (ed M. L. Yarmush) 135-161 (Annual Reviews, 2017).
- 74 Kesireddy, V. & Kasper, F. K. Approaches for building bioactive elements into synthetic scaffolds for bone tissue engineering. *J. Mat. Chem. B* **4**, 6773-6786, doi:10.1039/c6tb00783j (2016).
- 75 Wang, H. A., Leeuwenburgh, S. C. G., Li, Y. B. & Jansen, J. A. The Use of Micro- and Nanospheres as Functional Components for Bone Tissue Regeneration. *Tissue Eng. Part B-Rev.* **18**, 24-39, doi:10.1089/ten.teb.2011.0184 (2012).
- 76 Boudriot, U., Dersch, R., Greiner, A. & Wendorff, J. H. Electrospinning approaches toward scaffold engineering - A brief overview. *Artif. Organs* **30**, 785-792, doi:10.1111/j.1525-1594.2006.00301.x (2006).
- 77 Braghirolli, D. I., Steffens, D. & Pranke, P. Electrospinning for regenerative medicine: a review of the main topics. *Drug Discov. Today* **19**, 743-753, doi:10.1016/j.drudis.2014.03.024 (2014).
- 78 Haider, A., Haider, S. & Kang, I. K. A comprehensive review summarizing the effect of electrospinning parameters and potential applications of nanofibers in biomedical and biotechnology. *Arab. J. Chem.* **11**, 1165-1188, doi:10.1016/j.arabjc.2015.11.015 (2018).
- 79 Thavorniyutikarn, B., Chantarapanich, N., Sitthiseripratip, K., Thouas, G. A. & Chen, Q. Bone tissue engineering scaffolding: computer-aided scaffolding techniques. *Progress in Biomaterials* **3**, 61-102, doi:10.1007/s40204-014-0026-7 (2014).
- 80 Nichol, J. W. & Khademhosseini, A. Modular tissue engineering: engineering biological tissues from the bottom up. *Soft Matter* **5**, 1312-1319, doi:10.1039/b814285h (2009).
- 81 Boys, A. J. *et al.* Top-Down Fabrication of Spatially Controlled Mineral-Gradient Scaffolds for Interfacial Tissue Engineering. *ACS Biomater. Sci. Eng.* **5**, 2988-2997, doi:10.1021/acsbiomaterials.9b00176 (2019).
- 82 Gleadall, A., Visscher, D., Yang, J., Thomas, D. & Segal, J. Review of additive manufactured tissue engineering scaffolds: relationship between geometry and performance. *Burns Trauma* **6**, 16, doi:10.1186/s41038-018-0121-4 (2018).
- 83 Van Bael, S. *et al.* The effect of pore geometry on the in vitro biological behavior of human periosteum-derived cells seeded on selective laser-melted Ti6Al4V bone scaffolds. *Acta Biomater.* **8**, 2824-2834, doi:10.1016/j.actbio.2012.04.001 (2012).
- 84 Di Luca, A. *et al.* Tuning Cell Differentiation into a 3D Scaffold Presenting a Pore Shape Gradient for Osteochondral Regeneration. *Adv. Healthc. Mater.* **5**, 1753-1763, doi:10.1002/adhm.201600083 (2016).
- 85 Yilgor, P., Sousa, R. A., Reis, R. L., Hasirci, N. & Hasirci, V. 3D plotted PCL scaffolds for stem cell based bone tissue engineering. *Macromol. Symp.* **269**, 92-99, doi:10.1002/masy.200850911 (2008).
- 86 Ahn, C. B., Kim, Y., Park, S. J., Hwang, Y. & Lee, J. W. Development of arginine-glycine-aspartate-immobilized 3D printed poly(propylene fumarate) scaffolds

- for cartilage tissue engineering. *J. Biomater. Sci.-Polym. Ed.* **29**, 917-931, doi:10.1080/09205063.2017.1383020 (2018).
- 87 Holmes, B., Bulusu, K., Plesniak, M. & Zhang, L. G. A synergistic approach to the design, fabrication and evaluation of 3D printed micro and nano featured scaffolds for vascularized bone tissue repair. *Nanotechnology* **27**, 15, doi:10.1088/0957-4484/27/6/064001 (2016).
- 88 Shick, T. M., Kadir, A. Z. A., Ngadiman, N. H. A. & Ma'aram, A. A review of biomaterials scaffold fabrication in additive manufacturing for tissue engineering. *J. Bioact. Compat. Polym.* **34**, 415-435, doi:10.1177/0883911519877426 (2019).
- 89 Gloria, A., De Santis, R. & Ambrosio, L. Polymer-based composite scaffolds for tissue engineering. *J. Appl. Biomater. Biomech.* **8**, 57-67 (2010).
- 90 Moura, C. S., Ferreira, F. C. & Bartolo, P. J. in *Second Cirp Conference on Biomanufacturing* Vol. 49 *Procedia CIRP* (ed P. Bartolo) 209-212 (Elsevier Science Bv, 2016).
- 91 Fucile, P. *et al.* *Reverse Engineering and Additive Manufacturing towards the design of 3D advanced scaffolds for hard tissue regeneration.* (Ieee, 2019).
- 92 Magaldi, B. V., Pinto, M. O. C. M., Thiré, R. & Araujo, A. C. in *24th ABCM International Congress of Mechanical Engineering* (2017).
- 93 Kang, H. W. *et al.* A 3D bioprinting system to produce human-scale tissue constructs with structural integrity. *Nat. Biotechnol.* **34**, 312-+, doi:10.1038/nbt.3413 (2016).
- 94 Mekhileri, N. V. *et al.* Automated 3D bioassembly of micro-tissues for biofabrication of hybrid tissue engineered constructs. *Biofabrication* **10**, 21, doi:10.1088/1758-5090/aa9ef1 (2018).
- 95 Yang, Y. *et al.* Elastic 3D-Printed Hybrid Polymeric Scaffold Improves Cardiac Remodeling after Myocardial Infarction. *Adv. Healthc. Mater.* **8**, 15, doi:10.1002/adhm.201900065 (2019).
- 96 Koffler, J. *et al.* Biomimetic 3D-printed scaffolds for spinal cord injury repair. *Nat. Med.* **25**, 263-+, doi:10.1038/s41591-018-0296-z (2019).
- 97 Bettinger, C. J., Borenstein, J. T. & Langer, R. in *Principles of Tissue Engineering (Third Edition)* (eds Robert Lanza, Robert Langer, & Joseph Vacanti) 341-358 (Academic Press, 2007).
- 98 Melchels, F. P. W. *et al.* Additive manufacturing of tissues and organs. *Prog. Polym. Sci.* **37**, 1079-1104, doi:10.1016/j.progpolymsci.2011.11.007 (2012).
- 99 Mota, C., Puppi, D., Chiellini, F. & Chiellini, E. Additive manufacturing techniques for the production of tissue engineering constructs. *J. Tissue Eng. Regen. Med.* **9**, 174-190, doi:10.1002/term.1635 (2015).
- 100 Salerno, A., Cesarelli, G., Pedram, P. & Netti, P. A. Modular Strategies to Build Cell-Free and Cell-Laden Scaffolds towards Bioengineered Tissues and Organs. *Journal of Clinical Medicine* **8**, doi:<http://dx.doi.org/10.3390/jcm8111816> (2019).

- 101 Hochleitner, G. *et al.* Additive manufacturing of scaffolds with sub-micron filaments via melt electrospinning writing. *Biofabrication* **7**, 10, doi:10.1088/1758-5090/7/3/035002 (2015).
- 102 Farrugia, B. L. *et al.* Dermal fibroblast infiltration of poly(epsilon-caprolactone) scaffolds fabricated by melt electrospinning in a direct writing mode. *Biofabrication* **5**, 11, doi:10.1088/1758-5082/5/2/025001 (2013).
- 103 Brown, T. D., Daltona, P. D. & Hutmacher, D. W. Melt electrospinning today: An opportune time for an emerging polymer process. *Prog. Polym. Sci.* **56**, 116-166, doi:10.1016/j.progpolymsci.2016.01.001 (2016).
- 104 Park, S. H., Kim, T. G., Kim, H. C., Yang, D. Y. & Park, T. G. Development of dual scale scaffolds via direct polymer melt deposition and electrospinning for applications in tissue regeneration. *Acta Biomater.* **4**, 1198-1207, doi:10.1016/j.actbio.2008.03.019 (2008).
- 105 Vaquette, C. *et al.* A biphasic scaffold design combined with cell sheet technology for simultaneous regeneration of alveolar bone/periodontal ligament complex. *Biomaterials* **33**, 5560-5573, doi:10.1016/j.biomaterials.2012.04.038 (2012).
- 106 Dalton, P. D. *et al.* Electrospinning and additive manufacturing: converging technologies. *Biomater. Sci.* **1**, 171-185, doi:10.1039/c2bm00039c (2013).
- 107 Blum, C. *et al.* Extracellular Matrix-Modified Fiber Scaffolds as a Proadipogenic Mesenchymal Stromal Cell Delivery Platform. *ACS Biomater. Sci. Eng.* **5**, 6655-6666, doi:10.1021/acsbiomaterials.9b00894 (2019).
- 108 Xie, C. Q. *et al.* Structure-induced cell growth by 3D printing of heterogeneous scaffolds with ultrafine fibers. *Mater. Des.* **181**, 11, doi:10.1016/j.matdes.2019.108092 (2019).
- 109 Cha, C., Piraino, F. & Khademhosseini, A. in *Tissue Engineering (Second Edition)* (eds Clemens A. Van Blitterswijk & Jan De Boer) 283-310 (Academic Press, 2014).
- 110 Lima, M. J., Correlo, V. M. & Reis, R. L. Micro/nano replication and 3D assembling techniques for scaffold fabrication. *Mater. Sci. Eng. C-Mater. Biol. Appl.* **42**, 615-621, doi:10.1016/j.msec.2014.05.064 (2014).
- 111 Charest, J. L. & King, W. P. in *BioNanoFluidic MEMS* (ed Peter J. Hesketh) 251-277 (Springer US, 2008).
- 112 Papenburg, B. J. *et al.* One-step fabrication of porous micropatterned scaffolds to control cell behavior. *Biomaterials* **28**, 1998-2009, doi:10.1016/j.biomaterials.2006.12.023 (2007).
- 113 Papenburg, B. J. *et al.* Development and analysis of multi-layer scaffolds for tissue engineering. *Biomaterials* **30**, 6228-6239, doi:10.1016/j.biomaterials.2009.07.057 (2009).
- 114 Liu, Z. Y. *et al.* In vitro mimicking the morphology of hepatic lobule tissue based on Ca-alginate cell sheets. *Biomed. Mater.* **13**, 12, doi:10.1088/1748-605X/aaa4c4 (2018).
- 115 Ye, X. F. *et al.* Scalable Units for Building Cardiac Tissue. *Adv. Mater.* **26**, 7202-7208, doi:10.1002/adma.201403074 (2014).

- 116 Fischer, K. M. *et al.* Poly(Limonene Thioether) Scaffold for Tissue Engineering. *Adv. Healthc. Mater.* **5**, 813-821, doi:10.1002/adhm.201500892 (2016).
- 117 Guarino, V., D'Albore, M., Altobelli, R. & Ambrosio, L. Polymer Bioprocessing to Fabricate 3D Scaffolds for Tissue Engineering. *Int. Polym. Process.* **31**, 587-597, doi:10.3139/217.3239 (2016).
- 118 Ryu, W., Fasching, R. J., Vyakarnam, M., Greco, R. S. & Prinz, F. B. Microfabrication technology of biodegradable polymers for interconnecting microstructures. *J. Microelectromech. Syst.* **15**, 1457-1465, doi:10.1109/jmems.2006.883566 (2006).
- 119 Ryu, W. *et al.* The construction of three-dimensional micro-fluidic scaffolds of biodegradable polymers by solvent vapor based bonding of micro-molded layers. *Biomaterials* **28**, 1174-1184, doi:10.1016/j.biomaterials.2006.11.002 (2007).
- 120 Ryu, W. *et al.* Three-dimensional biodegradable microscaffolding: Scaffold characterization and cell population at single cell resolution. *Acta Biomater.* **7**, 3325-3335, doi:10.1016/j.actbio.2011.05.011 (2011).
- 121 Lima, M. J. *et al.* Bottom-up approach to construct microfabricated multi-layer scaffolds for bone tissue engineering. *Biomed. Microdevices* **16**, 69-78, doi:10.1007/s10544-013-9806-4 (2014).
- 122 Xia, Y. N. & Whitesides, G. M. Soft lithography. *Annu. Rev. Mater. Sci.* **28**, 153-184, doi:10.1146/annurev.matsci.28.1.153 (1998).
- 123 Xia, Y. N. & Whitesides, G. M. Soft lithography. *Angew. Chem.-Int. Edit.* **37**, 550-575, doi:10.1002/(sici)1521-3773(19980316)37:5<550::Aid-anie550>3.3.Co;2-7 (1998).
- 124 Xia, Y. N. *et al.* Replica molding using polymeric materials: A practical step toward nanomanufacturing. *Adv. Mater.* **9**, 147-149, doi:10.1002/adma.19970090211 (1997).
- 125 Gallego, D., Ferrell, N., Sun, Y. & Hansford, D. J. Multilayer micromolding of degradable polymer tissue engineering scaffolds. *Mater. Sci. Eng. C-Biomimetic Supramol. Syst.* **28**, 353-358, doi:10.1016/j.msec.2007.04.021 (2008).
- 126 Sodha, S. *et al.* Microfabrication of a Three-Dimensional Polycaprolactone Thin-Film Scaffold for Retinal Progenitor Cell Encapsulation. *J. Biomater. Sci.-Polym. Ed.* **22**, 443-456, doi:10.1163/092050610x487738 (2011).
- 127 Rosellini, E., Vozzi, G., Barbani, N., Giusti, P. & Cristallini, C. Three-dimensional microfabricated scaffolds with cardiac extracellular matrix-like architecture. *Int. J. Artif. Organs* **33**, 885-894 (2010).
- 128 He, J. K. *et al.* Bottom-up generation of 3D silk fibroin-gelatin microfluidic scaffolds with improved structural and biological properties. *Mater. Lett.* **78**, 102-105, doi:10.1016/j.matlet.2012.03.051 (2012).
- 129 Wang, L. *et al.* A BOTTOM-UP METHOD TO BUILD 3D SCAFFOLDS WITH PREDEFINED VASCULAR NETWORK. *J. Mech. Med. Biol.* **13**, 11, doi:10.1142/s0219519413400083 (2013).

- 130 He, J. K., Zhu, L., Liu, Y. X., Li, D. C. & Jin, Z. M. Sequential assembly of 3D perfusable microfluidic hydrogels. *J. Mater. Sci.-Mater. Med.* **25**, 2491-2500, doi:10.1007/s10856-014-5270-9 (2014).
- 131 Son, J., Bae, C. Y. & Park, J. K. Freestanding stacked mesh-like hydrogel sheets enable the creation of complex macroscale cellular scaffolds. *Biotechnol. J.* **11**, 8, doi:10.1002/biot.201500384 (2016).
- 132 Son, J., Bang, M. S. & Park, J. K. Hand-Maneuverable Collagen Sheet with Micropatterns for 3D Modular Tissue Engineering. *ACS Biomater. Sci. Eng.* **5**, 339-345, doi:10.1021/acsbomaterials.8b01066 (2019).
- 133 Zhang, B. Y. *et al.* Microfabrication of AngioChip, a biodegradable polymer scaffold with microfluidic vasculature. *Nat. Protoc.* **13**, 1793-1813, doi:10.1038/s41596-018-0015-8 (2018).
- 134 Lee, J. N., Park, C. & Whitesides, G. M. Solvent compatibility of poly(dimethylsiloxane)-based microfluidic devices. *Anal. Chem.* **75**, 6544-6554, doi:10.1021/ac0346712 (2003).
- 135 Yang, Y., Basu, S., Tomasko, D. L., Lee, L. J. & Yang, S. T. Fabrication of well-defined PLGA scaffolds using novel microembossing and carbon dioxide bonding. *Biomaterials* **26**, 2585-2594, doi:10.1016/j.biomaterials.2004.07.046 (2005).
- 136 Yang, Y., Xie, Y. B., Kang, X. H., Lee, L. J. & Kniss, D. A. Assembly of three-dimensional polymeric constructs containing cells/biomolecules using carbon dioxide. *J. Am. Chem. Soc.* **128**, 14040-14041, doi:10.1021/ja066157u (2006).
- 137 Xie, Y. B. *et al.* Bioassembly of Three-Dimensional Embryonic Stem Cell-Scaffold Complexes Using Compressed Gases. *Biotechnol. Prog.* **25**, 535-542, doi:10.1002/btpr.151 (2009).
- 138 Carugo, D. *et al.* Facile and cost-effective production of microscale PDMS architectures using a combined micromilling-replica moulding (mu Mi-REM) technique. *Biomed. Microdevices* **18**, 10, doi:10.1007/s10544-015-0027-x (2016).
- 139 Woodruff, M. A. & Hutmacher, D. W. The return of a forgotten polymer-Polycaprolactone in the 21st century. *Prog. Polym. Sci.* **35**, 1217-1256, doi:10.1016/j.progpolymsci.2010.04.002 (2010).
- 140 Mata, A., Fleischman, A. J. & Roy, S. in *Nanoscale Materials Science in Biology and Medicine* Vol. 845 *Materials Research Society Symposium Proceedings* (eds C. T. Laurencin & E. A. Botchwey) 97-103 (Materials Research Society, 2005).
- 141 Kolewe, M. E. *et al.* 3D Structural Patterns in Scalable, Elastomeric Scaffolds Guide Engineered Tissue Architecture. *Adv. Mater.* **25**, 4459-4465, doi:10.1002/adma.201301016 (2013).
- 142 Yang, Y., Zeng, C. C. & Lee, L. J. Three-dimensional assembly of polymer microstructures at low temperatures. *Adv. Mater.* **16**, 560+, doi:10.1002/adma.200306159 (2004).
- 143 Guan, J. J., He, H. Y., Lee, L. J. & Hansford, D. J. Fabrication of particulate reservoir-containing, capsulelike, and self-folding polymer microstructures for drug delivery. *Small* **3**, 412-418, doi:10.1002/smll.200600240 (2007).

- 144 Kim, C. M., Lee, H. B., Kim, J. U. & Kim, G. M. Fabrication of poly (lactic-co-glycolic acid) microcontainers using solvent evaporation with polydimethylsiloxane stencil. *J. Micromech. Microeng.* **27**, 9, doi:10.1088/1361-6439/aa9591 (2017).
- 145 Shi, X. T., Su, K., Varshney, R. R., Wang, Y. J. & Wang, D. A. Sintered Microsphere Scaffolds for Controlled Release and Tissue Engineering. *Pharm. Res.* **28**, 1224-1228, doi:10.1007/s11095-010-0359-4 (2011).
- 146 Ding, D. W. & Zhu, Q. D. Recent advances of PLGA micro/nanoparticles for the delivery of biomacromolecular therapeutics. *Mater. Sci. Eng. C-Mater. Biol. Appl.* **92**, 1041-1060, doi:10.1016/j.msec.2017.12.036 (2018).
- 147 Hajavi, J., Ebrahimian, M., Sankian, M., Khakzad, M. R. & Hashemi, M. Optimization of PLGA formulation containing protein or peptide-based antigen: Recent advances. *J. Biomed. Mater. Res. Part A* **106**, 2540-2551, doi:10.1002/jbm.a.36423 (2018).
- 148 Elzoghby, A. O., Samy, W. M. & Elgindy, N. A. Protein-based nanocarriers as promising drug and gene delivery systems. *J. Control. Release* **161**, 38-49, doi:10.1016/j.jconrel.2012.04.036 (2012).
- 149 Abid, Z. *et al.* Biodegradable microcontainers - towards real life applications of microfabricated systems for oral drug delivery. *Lab Chip* **19**, 2905-2914, doi:10.1039/c9lc00527g (2019).
- 150 Campiglio, C. E., Contessi Negrini, N., Fare, S. & Draghi, L. Cross-Linking Strategies for Electrospun Gelatin Scaffolds. *Materials* **12**, 23, doi:10.3390/ma12152476 (2019).
- 151 Kosmala, J. D., Henthorn, D. B. & Brannon-Peppas, L. Preparation of interpenetrating networks of gelatin and dextran as degradable biomaterials. *Biomaterials* **21**, 2019-2023, doi:10.1016/s0142-9612(00)00057-0 (2000).
- 152 Danilov, N. A. *et al.* Stabilization of scleral collagen by glycerol aldehyde cross-linking. *Biochim. Biophys. Acta-Gen. Subj.* **1780**, 764-772, doi:10.1016/j.bbagen.2008.01.014 (2008).
- 153 Imparato, G., Urciuolo, F., Casale, C. & Netti, P. A. The role of micro scaffold properties in controlling the collagen assembly in 3D dermis equivalent using modular tissue engineering. *Biomaterials* **34**, 7851-7861, doi:10.1016/j.biomaterials.2013.06.062 (2013).
- 154 Jo, B. H., Van Lerberghe, L. M., Motsegood, K. M. & Beebe, D. J. Three-dimensional micro-channel fabrication in polydimethylsiloxane (PDMS) elastomer. *J. Microelectromech. Syst.* **9**, 76-81, doi:10.1109/84.825780 (2000).
- 155 Porro, F. *et al.* Methods and a mold assembly for fabricating polymer structures by imprint techniques. (2014).
- 156 Kim, M., Moon, B. U. & Hidrovo, C. H. Enhancement of the thermo-mechanical properties of PDMS molds for the hot embossing of PMMA microfluidic devices. *J. Micromech. Microeng.* **23**, 10, doi:10.1088/0960-1317/23/9/095024 (2013).

- 157 Ren, K. N., Dai, W., Zhou, J. H., Su, J. & Wu, H. K. Whole-Teflon microfluidic chips. *Proc. Natl. Acad. Sci. U. S. A.* **108**, 8162-8166, doi:10.1073/pnas.1100356108 (2011).
- 158 Wu, D. P., Luo, Y., Zhou, X. M., Dai, Z. P. & Lin, B. C. Multilayer poly(vinyl alcohol)-adsorbed coating on poly(dimethylsiloxane) microfluidic chips for biopolymer separation. *Electrophoresis* **26**, 211-218, doi:10.1002/elps.200406157 (2005).
- 159 Yen, D. P., Ando, Y. & Shen, K. A cost-effective micromilling platform for rapid prototyping of microdevices. *Technology* **4**, 234-239, doi:10.1142/s2339547816200041 (2016).
- 160 Guckenberger, D. J., de Groot, T. E., Wan, A. M. D., Beebe, D. J. & Young, E. W. K. Micromilling: a method for ultra-rapid prototyping of plastic microfluidic devices. *Lab Chip* **15**, 2364-2378, doi:10.1039/c5lc00234f (2015).
- 161 Madsen, M. H., Feidenhans'l, N. A., Hansen, P. E., Garnaes, J. & Dirscherl, K. Accounting for PDMS shrinkage when replicating structures. *J. Micromech. Microeng.* **24**, 6, doi:10.1088/0960-1317/24/12/127002 (2014).
(ed Goodfellow Cambridge Ltd) (2020).
- 163 Moraes, C., Sun, Y. & Simmons, C. A. Solving the shrinkage-induced PDMS alignment registration issue in multilayer soft lithography. *J. Micromech. Microeng.* **19**, 6, doi:10.1088/0960-1317/19/6/065015 (2009).
- 164 Trantidou, T., Elani, Y., Parsons, E. & Ces, O. Hydrophilic surface modification of PDMS for droplet microfluidics using a simple, quick, and robust method via PVA deposition. *Microsyst. Nanoeng.* **3**, 9, doi:10.1038/micronano.2016.91 (2017).
- 165 Suo, B. T. *et al.* Poly (vinyl alcohol) thin film filled with CdSe-ZnS quantum dots: Fabrication, characterization and optical properties. *Mater. Chem. Phys.* **119**, 237-242, doi:10.1016/j.matchemphys.2009.08.054 (2010).
- 166 Lee, B. K. & Lee, B. Y. Investigation of thermoplastic hot embossing process using soft polydimethylsiloxane (PDMS) micromold. *J. Mech. Sci. Technol.* **29**, 5063-5067, doi:10.1007/s12206-015-1102-1 (2015).
- 167 Zhu, X. L. & Cui, T. H. Fabrication of polymer via holes by a combination of hot embossing and indentation processes. *J. Micromech. Microeng.* **21**, 8, doi:10.1088/0960-1317/21/4/045032 (2011).
- 168 Prabha, R. D. *et al.* Bioactive nano-fibrous scaffold for vascularized craniofacial bone regeneration. *J. Tissue Eng. Regen. Med.* **12**, E1537-E1548, doi:10.1002/term.2579 (2018).
- 169 Ogata, Y. H. in *Handbook of Porous Silicon* (ed Leigh Canham) 705-712 (Springer International Publishing, 2018).
- 170 Aina, A. *et al.* Dissolution behavior of poly vinyl alcohol in water and its effect on the physical morphologies of PLGA scaffolds. *UK Journal of Pharmaceutical and Biosciences* **2**, 1-6 (2014).
- 171 Semnani, D. A novel model of optimum nanofibre distribution in nanofibre scaffold structure by genetic algorithm method. *J. Exp. Nanosci.* **9**, 966-981, doi:10.1080/17458080.2012.752583 (2014).

- 172 Takeda, I., Serizawa, S. & Kaneko, A. Fabrication of micro-structured scaffold using self-assembled particles and effects of surface geometries on cell adhesion. *Mech. Eng. J.* **3**, 8, doi:10.1299/mej.15-00521 (2016).
- 173 Silva-Bermudez, P., Ramirez, G. & Rodil, S. E. in *Bio-Tribocorrosion in Biomaterials and Medical Implants* (ed Yu Yan) 250-308 (Woodhead Publishing, 2013).
- 174 Wennerberg, A., Ohlsson, R., Rosen, B. G. & Andersson, B. Characterizing three-dimensional topography of engineering and biomaterial surfaces by confocal laser scanning and stylus techniques. *Med. Eng. Phys.* **18**, 548-556, doi:10.1016/1350-4533(95)00005-4 (1996).
- 175 Chang, H.-I. & Wang, Y. in *Regenerative medicine and tissue engineering-cells and biomaterials* (InTechOpen, 2011).
- 176 Salerno, A., Guarino, V., Oliviero, O., Ambrosio, L. & Domingo, C. Bio-safe processing of polylactic-co-caprolactone and polylactic acid blends to fabricate fibrous porous scaffolds for in vitro mesenchymal stem cells adhesion and proliferation. *Mater. Sci. Eng. C-Mater. Biol. Appl.* **63**, 512-521, doi:10.1016/j.msec.2016.03.018 (2016).
- 177 Serra, T., Planell, J. A. & Navarro, M. High-resolution PLA-based composite scaffolds via 3-D printing technology. *Acta Biomater.* **9**, 5521-5530, doi:10.1016/j.actbio.2012.10.041 (2013).
- 178 Wang, X. & Baker, I. Observation of the microstructural evolution of snow under uniaxial compression using X-ray computed microtomography. *J. Geophys. Res.-Atmos.* **118**, 12371-12382, doi:10.1002/2013jd020352 (2013).
- 179 Parrilli, A. *et al.* Compression test on porous polymeric scaffolds. *n.d.*, 69-72 (2009).
- 180 Bertoldi, S., Fare, S. & Tanzi, M. C. Assessment of scaffold porosity: the new route of micro-CT. *J. Appl. Biomater. Biomech.* **9**, 165-175, doi:10.5301/jabb.2011.8863 (2011).
- 181 Hoque, M. E. *et al.* Processing of Polycaprolactone and Polycaprolactone-Based Copolymers into 3D Scaffolds, and Their Cellular Responses. *Tissue Eng. Part A* **15**, 3013-3024, doi:10.1089/ten.tea.2008.0355 (2009).
- 182 Eshraghi, S. & Das, S. Mechanical and microstructural properties of polycaprolactone scaffolds with one-dimensional, two-dimensional, and three-dimensional orthogonally oriented porous architectures produced by selective laser sintering. *Acta Biomater.* **6**, 2467-2476, doi:10.1016/j.actbio.2010.02.002 (2010).
- 183 Borselli, C. *et al.* Bioactivation of collagen matrices through sustained VEGF release from PLGA microspheres. *J. Biomed. Mater. Res. Part A* **92A**, 94-102, doi:10.1002/jbm.a.32332 (2010).
- 184 d'Angelo, I., Oliviero, O., Ungaro, F., Quaglia, F. & Netti, P. A. Engineering strategies to control vascular endothelial growth factor stability and levels in a collagen matrix for angiogenesis: The role of heparin sodium salt and the PLGA-based microsphere approach. *Acta Biomater.* **9**, 7389-7398, doi:10.1016/j.actbio.2013.03.013 (2013).

- 185 Kim, H. T., Kim, J. K. & Jeong, O. C. Hydrophilicity of Surfactant-Added Poly(dimethylsiloxane) and Its Applications. *Jpn. J. Appl. Phys.* **50**, 4, doi:10.1143/jjap.50.06gl04 (2011).
- 186 Tao, S. L. & Desai, T. A. Microfabrication of multilayer, asymmetric, polymeric devices for drug delivery. *Adv. Mater.* **17**, 1625+, doi:10.1002/adma.200500017 (2005).
- 187 de Alteriis, R. *et al.* A method to tune the shape of protein-encapsulated polymeric microspheres. *Sci Rep* **5**, 9, doi:10.1038/srep12634 (2015).
- 188 Jeon, J. H. *et al.* Tailoring of processing parameters for sintering microsphere-based scaffolds with dense-phase carbon dioxide. *J. Biomed. Mater. Res. Part B* **101B**, 330-337, doi:10.1002/jbm.b.32843 (2013).
- 189 Singh, M., Sandhu, B., Scurto, A., Berkland, C. & Detamore, M. S. Microsphere-based scaffolds for cartilage tissue engineering: Using subcritical CO₂ as a sintering agent. *Acta Biomater.* **6**, 137-143, doi:10.1016/j.actbio.2009.07.042 (2010).
- 190 Bhamidipati, M., Sridharan, B., Scurto, A. M. & Detamore, M. S. Subcritical CO₂ sintering of microspheres of different polymeric materials to fabricate scaffolds for tissue engineering. *Mater. Sci. Eng. C-Mater. Biol. Appl.* **33**, 4892-4899, doi:10.1016/j.msec.2013.08.010 (2013).
- 191 Ennett, A. B., Kaigler, D. & Mooney, D. J. Temporally regulated delivery of VEGF in vitro and in vivo. *J. Biomed. Mater. Res. Part A* **79A**, 176-184, doi:10.1002/jbm.a.30771 (2006).
- 192 Nemeth, C. L., Lykins, W. R., Tran, H., ElSayed, M. E. H. & Desai, T. A. Bottom-Up Fabrication of Multilayer Enteric Devices for the Oral Delivery of Peptides. *Pharm. Res.* **36**, 12, doi:10.1007/s11095-019-2618-3 (2019).
- 193 Quade, M. *et al.* Central Growth Factor Loaded Depots in Bone Tissue Engineering Scaffolds for Enhanced Cell Attraction. *Tissue Eng. Part A* **23**, 762-772, doi:10.1089/ten.tea.2016.0483 (2017).